INFRARED LASER FUSION AND BISECTION OF BLOOD VESSELS WITH REAL-TIME OPTICAL DIAGNOSTIC FEEDBACK

by

Nicholas Constantine Giglio

A dissertation submitted to the faculty of
The University of North Carolina at Charlotte
in partial fulfillment of the requirements
for the degree of Doctor of Philosophy in
Optical Science and Engineering

Charlotte

2022

Approved by:

____
Dr. Nathaniel Fried

____
Dr. Tino Hofmann

____
Dr. Yasin Raja

____
Dr. Harish Cherukuri

ABSTRACT

NICHOLAS CONSTANTINE GIGLIO. Thermal Fusion and Bisection of Blood Vessels Using Infrared Lasers with Real -Time Optical Diagnostic Feedback. (Under the direction of DR. NATHANIEL M. FRIED)

The conventional method of suture ligation of vascular tissues during surgery is time consuming, skill intensive, and leaves foreign objects in the body. Energy-based radiofrequency(RF) and ultrasonic (US) devices have recently replaced the use of sutures and mechanical clips, providing rapid hemostasis during surgery. These devices expedite numerous labor-intensive surgical procedures, including lobectomy, nephrectomy, gastric bypass, splenectomy, thyroidectomy, hysterectomy, cystectomy, and colectomy. Though these newer methods provide rapid and efficient blood vessel ligation, both US and RF devices have limitations including the potential for unacceptably large collateral thermal damage zones, with thermal spread averaging greater than 1 mm. This lack of precision prevents the use of these devices for delicate surgical procedures performed in confined spaces (such as prostatectomy). These devices may also cause thermal damage to healthy tissue through unintended heat conduction in contact with the device jaws. The active jaw of US devices can reach temperatures in excess of 200 ^{o}C during a single application and can take greater than 20 s to cool to usable temperatures before proceeding with further applications. The maximum temperatures on the active jaw of RF devices are lower (< 100 ^{o}C), however, larger thermal spread is observed. This study explores the development of a novel alternative method using near-infrared (IR) lasers for vessel ligation, bisection, and real-time feedback during procedures. This dissertation focuses on the sealing (the act of permanently fusing the lumen of the vessel) and cutting (the act of bisecting a vessel) of the arteries (1-6 mm in diameter), which are the most common vessels sealed with an energy-based device during laparoscopic surgery. There are several potential advantages of laser-based sealing and cutting of vascular tissues compared to conventional US and RF energy-based devices. These include: (1) More rapid sealing and cutting of vascular tissues with seal and cut times as short as 1 s each; (2) More directed deposition of energy into tissue with collateral thermal spread of less than 1 mm; (3) Stronger vessel seals with higher burst pressures (up to 1500 mmHg); (4) An integrated device capable of both optical sealing and cutting of vascular tissues without the need for a separate deployable mechanical blade to bisect tissue seals; (5) Safer thermal profile with lower jaw peak temperatures (< 60 °C) compared to ultrasound (~ 200 °C) and radiofrequency (~ 100 °C) devices; (6) Sealing of large blood vessels greater than 5 mm; and (7) An entirely optical based system with real-time quantitative feedback indicating the success of the thermal seal and/or bisection of the blood vessel. This dissertation will explore these advantages for laser-based technology along with an optical method for real – time optical feedback all with the capability of laparoscopic device integration.

DEDICATION

I dedicate this dissertation to:

Denise Giglio
Who devoted time and energy to cultivate and harmonize my skill set, positioning me on a road towards success. Who always has and always will believe in my potential.

Thomas Giglio
Who captained my ship through calm and rough waters, always arriving at a destination, where I could flourish and accomplish my goals. Whose advice never falters and guidance points my compass true.

Noël Denice
Who has always paved the way regardless of which path I pursued. Who constantly goes above and beyond the call of duty to support me in achieving my goals.

Kelly Harrington
Whose continued encouragement and support champions my success. Who always helps bail out the ship, when I take on too much water.

William Giglio, Sr.
Who was the finest engineer that initially stimulated my interest in the field of Physics and Engineering. Whose inspirational work ethic will live on in my future endeavors.

Thank you

ACKNOWLEDGMENTS

I would like to thank Dr. Nathaniel Fried, my advisor, for his continued support and guidance throughout my research and academic studies. I would also like to thank all of my fellow Biomedical Optics Laboratory members and members of other laboratories who have provided insight and assistance throughout my graduate career, including Dr. Thomas Hutchens and Dr. Luke Hardy. I also appreciate the assistance of my committee members, Dr. Yasin Raja, Dr. Tino Hofmann, and Dr. Harish Cherukuri in critiquing and supporting my research. I also appreciate the Graduate Assistant Support Plan (GASP) provided by the graduate school at UNC Charlotte. This work was supported by the National Institute of Biomedical Imaging and Bioengineering of the National Institutes of Health, under Grant R15EB028576. Support for this work was also given by the Lucille P. and Edward C. Giles Dissertation - Year Graduate Fellowship at UNC Charlotte.

TABLE OF CONTENTS

LIST OF TABLES

LIST OF FIGURES

LIST OF ABBREVIATIONS

~	Approximately
BSZ	Bifurcated seal zone
BP	Burst Pressure
°C	Degrees Celsius
Δ	Change
CAD	Computer aided design
CW	Continuous wave
DOE	Design of experiment
DALSCI	Detection aided laser sealing and cutting instrument
ED	Effective diameter
FDA	Food and Drug Administration
FWHM	Full width-half maximum
HTE	Heat transfer equation
InGaAs	Indium gallium arsenide
IR	Infrared
KTP	Potassium Titanyl Phosphate
mm	Millimeter
mmHg	Millimeter of mercury
MC	Monte Carlo
MM	Multimode
nm	Nanometer
ND	Neutral density

N	Newton
NA	Numerical aperture
OD	Outer diameter
OCT	Optical coherence tomography
OH	Hydroxyl
OPD	Optical penetration depth
PSI	Pounds per square inch
RF	Radiofrequency
s	Seconds
SD	Standard deviation
TS	Thermal spread
TIR	Total internal reflection
UK	Unknown
US	Ultrasonic
UV	Ultraviolet
W	Watt
YAG	yttrium aluminum garnet

CHAPTER 1: INTRODUCTION

Suture ligation of blood vessels is a medical practice which dates back as early as the first century AD. One of the first medical documentations of blood vessel ligation, as a clinical treatment, is credited to Archigenes of Apamea, a Greco-Syrian physician, who stated that vessel ligation is a necessary first step in removing cancerous tumors [1]. In modern medicine, the primitive suture and clip method of blood vessel ligations is still performed during surgery. This method leaves foreign objects in the body and can be time consuming and skill intensive. Energy-based electrosurgical and ultrasonic devices have recently replaced the use of sutures and mechanical clips, providing rapid hemostasis during surgery. Energy-based devices are used in about 80% of the approximately ~ 15 million laparoscopic procedures performed globally each year [2]. These energy-based instruments compress the blood vessel, which collapse the vessel`s internal lumen, and thermally denatures proteins in the blood vessel’s wall to permanently seal the lumen (without leaving foreign objects in the body). The sealed blood vessel can withstand hypertensive blood pressures to restrict blood flow. Finally, the devices then bisect the blood vessel or vascular bundle, thus allowing both hemostatic seals, while also creating a path forward during laparoscopic surgery for the surgeon to reach the diseased tissue to be removed.

Currently, the two most common energy-based technologies used in operating rooms to seal and cut blood vessels are ultrasonic (US) and radiofrequency (RF) devices. Ultrasonic technology uses vibration to coagulate and cut blood vessels. The US technology utilizes friction energy which is generated through a linear piezoelectric crystal driven at a high vibration frequency (up to 55 kHz). These high frequency US waves get absorbed by the vascular tissue which seals (~20 kHz) and cuts (~ 55 kHz) in the specified areas [3]. The mechanical energy is converted into heat, which is the mechanism that denatures the proteins in the blood vessel, causing a seal at low frequencies or vaporization of tissue at higher frequencies [3]. As seen in Figure 1.1, the ultrasonic scalpel has two jaws: an upper jaw which linearly oscillates and a lower jaw which is stationary and used solely to provide pressure to clamp the vessel in place.

Radiofrequency technology (e.g. Ligature device), achieves hemostasis through the use of bipolar radiofrequency (RF) energy at a frequency of 473 kHz [4]. These devices generate an electrical current which is passed though both sides of the blood vessel, and which generates heat, resulting in thermal coagulation of the vessels. The RF device has two jaws; the vessel is clamped between these two jaws and the electrical current is passed through the blood vessel (Figure 1.1). After the blood vessel has transformed sufficient electrical current to heat through Ohmic heating, a separate mechanical blade is deployed to bisect the seal [4]. The LigaSure device is considered the current leader in the RF technology space due to its semi-automated process which operates using real time feedback. The real time feedback system, which is integrated into the LigaSure device, is called TissueFect™ sensing technology. TissueFect™ is designed to monitor the change in electrical impedance of the tissue during procedures [5].

Both US and RF devices are used to expedite numerous surgical procedures including lobectomy [6-7], nephrectomy [8], gastric bypass [9-11], splenectomy [12, 13], thyroidectomy [14-19], hysterectomy [20], and colectomy [21-24]. However, clinical RF and US devices have several limitations which are summarized in Table 1.1. Limitations include tissue charring and significant thermal spread beyond the seal zone, averaging > 1 mm [25-28]. Potential thermal damage to critical tissue structures in confined spaces also prevents use of these devices in sensitive procedures (e.g. nerve-sparing radical prostatectomy) [29,30]. The active jaw of US devices can reach > 200 ^{o}C and can take > 20 s to cool between applications. Maximum active jaw temperatures for RF devices are lower (< 100 ^{o}C), but a larger thermal spread is observed [31-34].

Lasers are being explored as an alternative energy-based device for laparoscopic medical instrumentation for sealing and cutting of blood vessels. Our laboratory is currently pioneering the path for the use of infrared (IR) laser sealing and cutting of blood vessels. Several advantages of laser-based devices include (1) rapid sealing and cutting of vascular tissues with times of ~ 1 s each, (2) directed deposition of energy into tissue with less thermal spread (< 1 mm), (3) stronger vessel seals with much higher burst pressures (BP) than hypertensive (180 mmHg) blood pressure, (4) an integrated device capable of optical sealing and cutting without a separate, deployable, mechanical blade to bisect tissue seals, and (5) lower jaw temperatures (< 60 ^{o}C) compared to US and RF devices. Use of near-infrared lasers may potentially solve these current limitations and provide a more efficient tool for laparoscopic surgery. This dissertation describes the design, construction, and testing of a fully optical-based system for precise sealing and cutting with real-time feedback for a wide range of blood vessel sizes.

Figure 1.1: (Left) Ultrasonic Harmonic Focus Shears technology (Right) LigaSure^{TM}, radiofrequency bipolar electrosurgical device

Table 1.1: Comparison of commercial and experimental vessel sealing and cutting techniques [25-40].

Device	**Vessel Ligation (clips)**	**US Energy**	**RF Energy**	**IR Laser**
Time to seal vessel (s)	~ 50	~ 5	~ 7	~ 1
Cut without external blade	✗	✓	✗	✓
Thermal damage zone (mm)	NA	2.7 ± 0.7	2.0 ± 0.4	1.0 ± 0.4
Real-time feedback	✗	✓	✓	✓
Need for safety glasses	✗	✗	✗	✓
External jaw temperature (°C)	NA	> 200	> 100	< 60
Mean burst pressure (mmHg)	~ 720	~ 200	~ 740	~ 1300

CHAPTER 2: METHODS

2.1: Anatomy of a Vascular System and Blood Vessels

The human body's vascular highway is considered a closed system. The closed system ensures that blood flows from the heart through arteries to specific organs and then travels back to the heart through the veins, completing the system. Vessels are tubular in shape and contain an internal lumen for blood flow. Blood vessels have five main classifications, based on size and function: the aorta, arteries, arterioles, capillaries, and veins. This dissertation focuses on the sealing (the act of permanently fusing the lumen of the vessel) and cutting (the act of bisecting a vessel) of the arteries (1-6 mm in diameter), which are the most common vessels sealed with an energy-based device during laparoscopic surgery. The Food and Drug Administration (FDA) has approved energy-based devices for sealing vessels less than 7 mm in diameter (arteries) [32]. Sealing or fusing is the act of permanently closing the lumen of the vessel to restrict blood flow. The act of cutting or vaporization occurs after a vessel has been sealed. The cut is created along the center of the seal bisecting the vessel, creating two halves, as shown in Figure 2.1.

Figure 2.1: (A) A harvested porcine blood vessel. (B) Concept art of a laparoscopic laser-based device to seal and cut a blood vessel with real time feedback. (C) A successfully sealed and cut vessel (not drawn to scale).

Arteries are considered soft tissue composed of several different cellular layers (Figure 2.2). There are three main layers in an arteriole. The inner most layer located next to the lumen, called the tunica intima, consists of endothelial cells and has a thickness on the order of 10 µm, making up approximately 11% of the vessel wall [35]. The middle layer, which is known as the tunica media, mostly consists of smooth muscle cells and elastin fibers with an average cell thickness of 20 µm. This is generally the thickest layer in the vessel and makes up approximately 56% of the vessel wall [35]. The outer most layer, known as the tunica externa, primarily consists of collagen fibers with a thickness of around 10 µm, making up approximately 33% of the vessel wall [35]. Since the first step of sealing a lumen is to compress the blood vessel, one homogeneous media is considered when analyzing optical tissue properties. The understanding of the structural makeup and collagen / elastin ratios of the vessel is important for future analysis. Knowledge of the structural makeup of the blood vessels enables a comparison between like blood vessels and the use of similar coefficients that match a similar structural makeup, such as human aorta or porcine vessels.

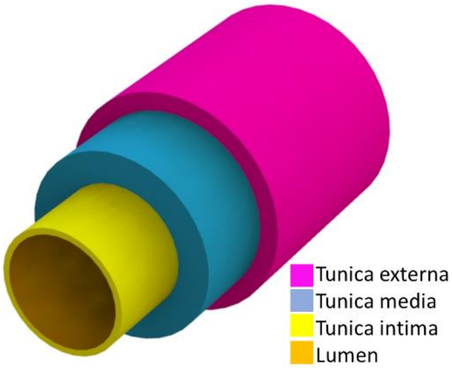

Figure 2.2: The structure of an arteriole vessel (not drawn to scale).

2.2: Tissue Dissection

For testing IR laser technology, a porcine model was chosen which closely matches human blood vessel physiology [43,44]. The porcine renal blood vessels were used for all laboratory studies. Fresh porcine kidney pairs were obtained (Spear Products, Inc, Coopersburg, Pennsylvania), and renal blood vessels were then dissected. To successfully extract a blood vessel tree from the porcine kidney, the kidney must first be removed from the renal capsule. Then, the upper layer of the renal cortex is carefully removed to expose the vessel tree (Figure 2.3A). Once the vessel tree is surgically exposed, the entire vascular tree is surgically removed from the kidney. The vessel tree consists of numerous bifurcations with a wide range of diameters for testing (Figure 2.3B). During studies, blood vessels were categorized as small (< 2 mm), medium (2-4 mm), or large (> 4 mm) samples. Prior to use, all blood vessels were cleaned of fat, stored in physiological saline, and refrigerated at 4 °C, for no longer than 48 hrs. Samples were brought to room temperature (20 °C) before each experiment was performed.

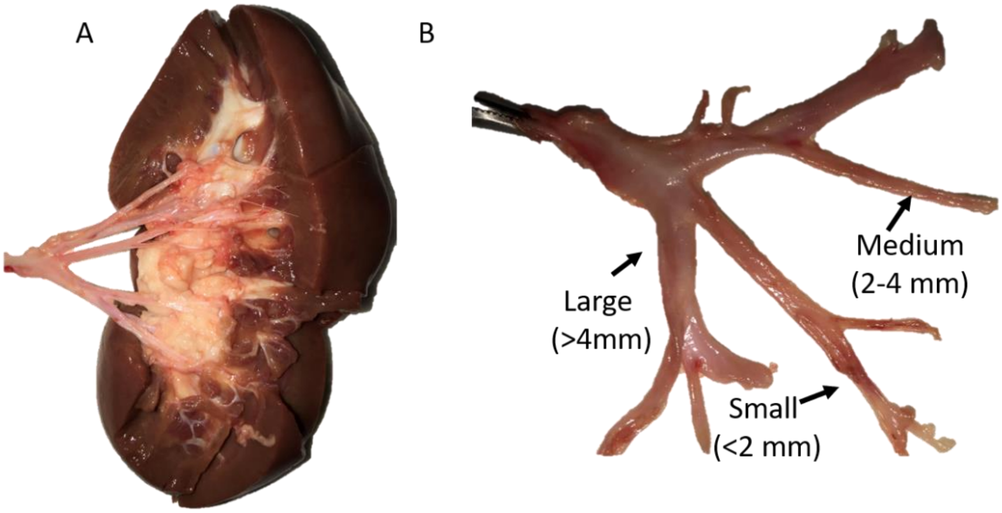

Figure 2.3: (A) Porcine kidney and (B) Branch of dissected vessels of various sizes.

2.3: Blood Vessel Compression

When laparoscopic energy-based devices are used to seal blood vessels, the jaws of the device clamp onto the blood vessel to collapse the lumen. The force applied to clamp down on the blood vessel ranges from 275 to 1758 kPa, depending on the device used [49,50]. When using an optical energy-based device, the thickness of the compressed blood vessel is an important factor to consider. The blood vessel thickness needs to be constant for laser ligation because the optical penetration depth is calculated to reach the entire depth of the tissue. When compressing blood vessels (1-6 mm), the optimal compressibility to collapse the lumen, based on preliminary experiments, is approximately 400 micrometers. However, when the blood vessel is compressed, its width changes, depending on the lumen to wall ratio of each independent blood vessel.

A study was performed to show the percent change in uncompressed to compressed widths of blood vessels. A total of 31 vessels ranging in size from 1 to 5 mm were compressed to 400 micrometers. These vessel diameters were measured with calipers before and during compression. The percent change was recorded, and an average of almost 50 percent increase of vessel diameters was observed during compression (Figure 2.4). This will have a significant impact on the linear laser beam profile length when designing an instrument that will seal blood vessels of 1 – 6 mm in diameter before compression.

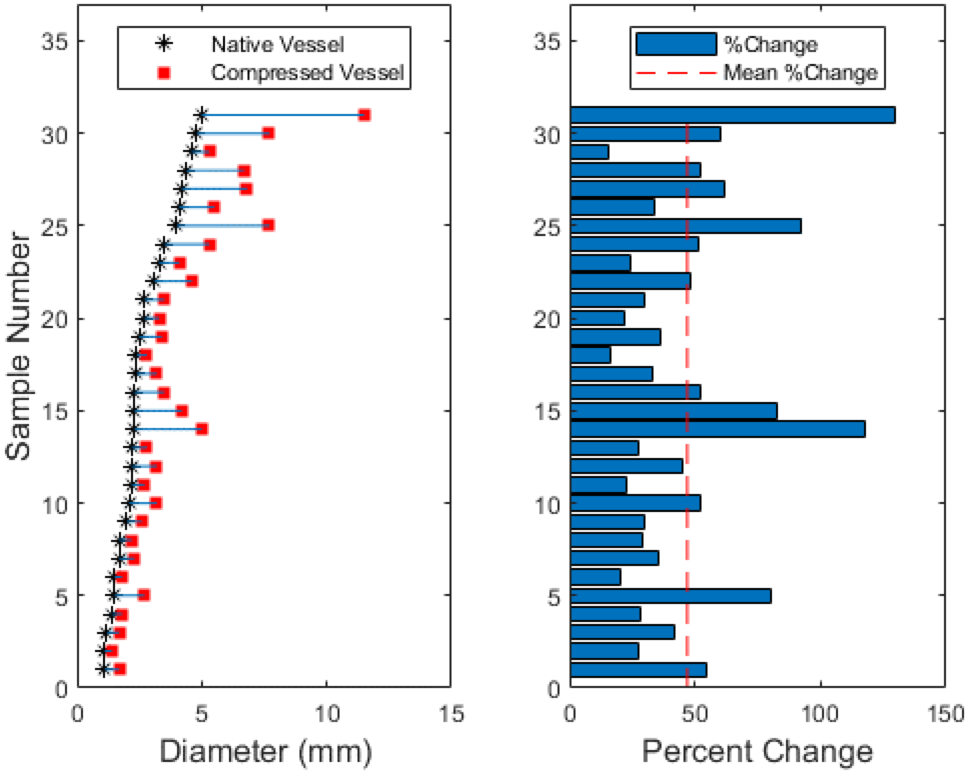

Figure 2.4: Graph on left shows native vessel diameters and compressed to 400 micrometer vessel diameters. Graph on right shows percent change with the mean increase measuring about 50 %.

2.4: Burst Pressure Measurements

Vessel burst pressure measurements were used as the primary indicator of success. The burst pressure setup consisted of a pressure meter (Model 717 100 G, Fluke, Everett, WA), infusion pump (Cole Parmer, Vernon Hills, IL), and an iris clamp as a standard method for measuring vessel seal burst strength [32,46] (Figure 2.5). The process for the vessel burst pressure measurement was completed using the following steps. The lumen of the vessel was placed over a cannula attached to the infusion pump. An iris was then closed to seal the vessel onto the cannula. Next, de-ionized water was infused at a rate of 28 mm^3/s and the pressure was measured with a pressure meter. The infusion rate was chosen based on the average velocity (3 mm/s) [47-48] and vessel diameter (3.5 mm) of arteries, where flow rate is equal to the area times velocity. Finally, the maximum pressure (mmHg) achieved when the vessel seal burst was recorded.

Blood pressure through a vessel varies with the size of the vessel. The vessel diameter sizes targeted for these experiments are in the range of the arteries and categorized as small (< 2 mm), medium (2-4 mm), and large (> 4 mm). The pressure of the arteries ranges from 80 mmHg to 120 mmHg (Figure 2.6). To quantify a successful seal, an industry standard threshold was used that quantifies systolic blood pressure slightly higher than average. A seal is considered successful if the seal can withstand a pressure of three times systolic blood pressure (120 mmHg), equating to 360 mmHg. This over estimation for seal strength accounts for any anomaly of high blood pressure that may occur during surgery.

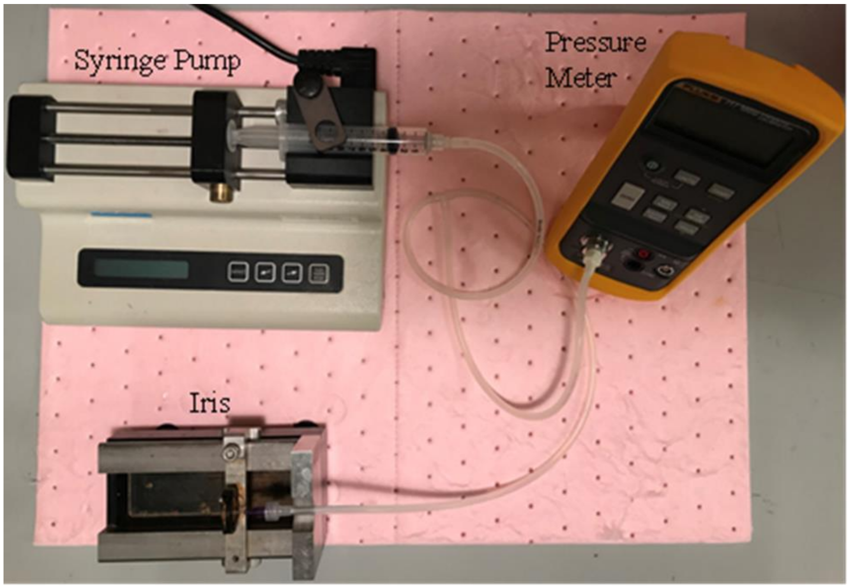

Figure 2.5: Vessel burst pressure measurements used as an indicator of vessel seal strength.

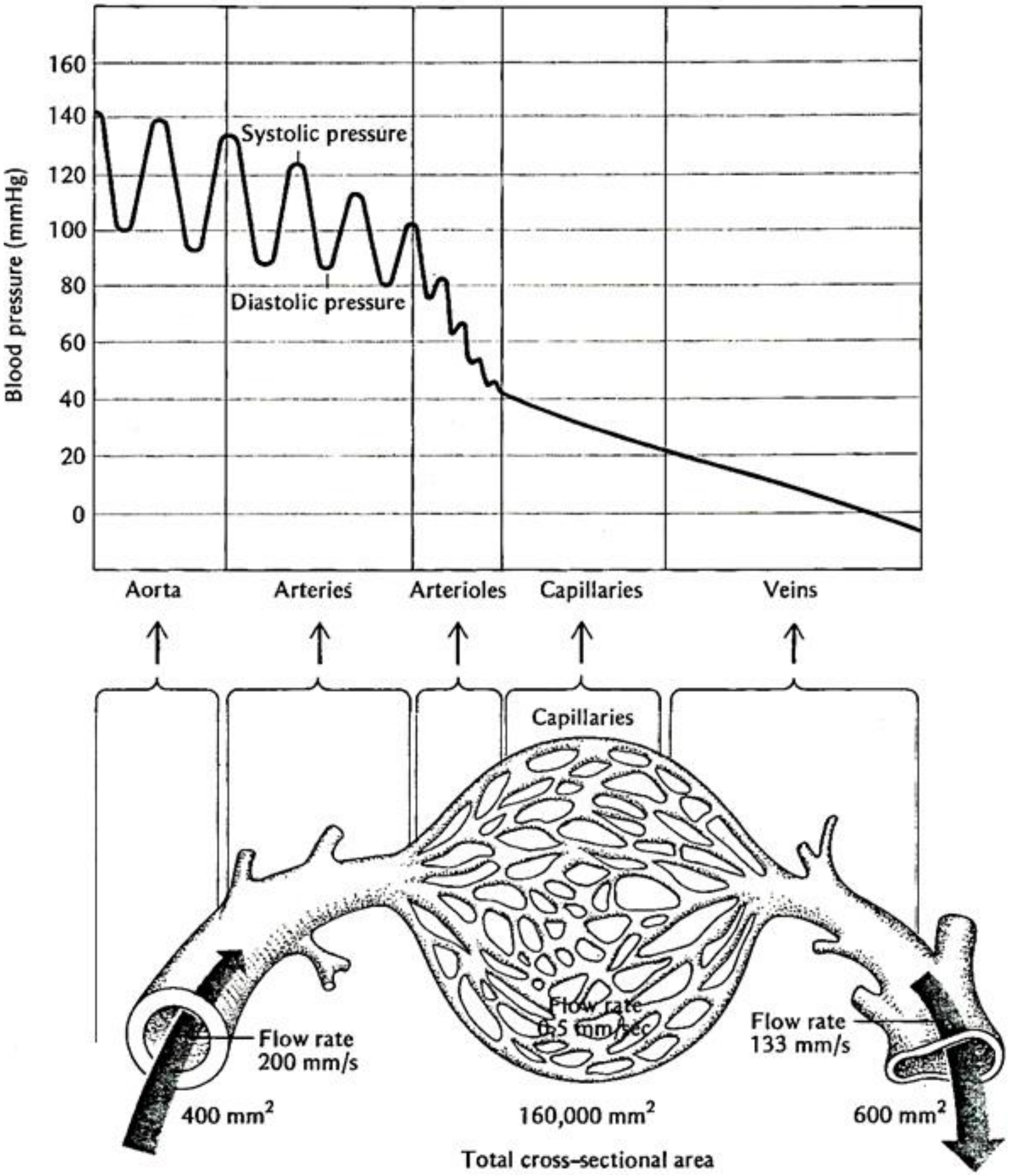

Figure 2.6: Blood pressure as a function of vessel sizes. [55]

CHAPTER 3: THEORY

3.1: Optical Properties of Soft Tissues

To understand the underlying science of a laser-based blood vessel sealing device, it is useful to describe how light interacts with soft tissues. Light interacts with biological tissues in four major processes: reflection, refraction, absorption, and scattering. However, when discussing laser tissue interactions, refraction is only important when the tissue sample is transparent (such as the cornea or during optical clearing of tissues). Since this is not the case for compressed blood vessels, refraction will not be considered moving forward. The extent of the three remaining interactions varies depending on the composition of the tissue.

Reflection of light can be classified into two categories: specular and diffuse reflection. Specular reflection occurs when light interacts with a “glossy” or an optically smooth surface. The surface can be considered optically smooth if the surface roughness of the interface is on the order of less than the wavelength of light with which it is interacting. These specular reflections can be quantified using Fresnel equations, which depend on the index of refraction (n). Diffuse reflection occurs when light interacts with a surface which has a surface roughness greater than that of the wavelength of light with which it is interacting.

Absorption is the complete transfer of energy from an incident photon to the material. When the photon is absorbed by a material, the molecules in the material vibrate and generally transform the energy into heat. There are very specific wavelengths which can be absorbed by a material. In soft tissues, the absorption spectrum is determined by the type of cells that the soft tissue is comprised of as well as the concentration of water in the soft tissue. The probability of the event that a photon is absorbed in the layer (per unit path length) of soft tissue is defined as the absorption coefficient (μ_a), which varies by wavelength (Figure 3.1). When attempting to couple light into soft tissue and convert the optical energy into heat, a wavelength should be chosen with a high absorption coefficient. When absorption is the main interaction between the light and the material, and the absorption coefficient is much greater than the scattering coefficient ($\mu_a >> \mu_s$), then the propagation of the light through the tissue can be accurately modeled using Beer's law of attenuation. Beer's law states that the rate of decrease in direct irradiance of collimated light, if incident on a homogenous medium of thickness (x), is proportional to the irradiance of the incident light.

$$-\frac{dI}{dx} \propto I \qquad 3.1$$

In order to make these two quantities equal, the absorption coefficient must be used as a proportionality constant. Therefore, it can be stated as:

$$-\frac{dx}{dI} = \frac{1}{\mu_a I} \qquad 3.2$$

Integrating the above equation results in:

$$-\int_0^x dx = \int_{I_o}^{I_t} \frac{1}{\mu_a I} dI \qquad 3.3$$

$$-x\mu_a = \ln\frac{I_t}{I_o} \qquad 3.4$$

$$I_t = I_o e^{-\mu_a x} \qquad 3.5$$

where I_o is the initial irradiance of the incoming light and I_t is the irradiance of light transmitted at a tissue depth or thickness of x.

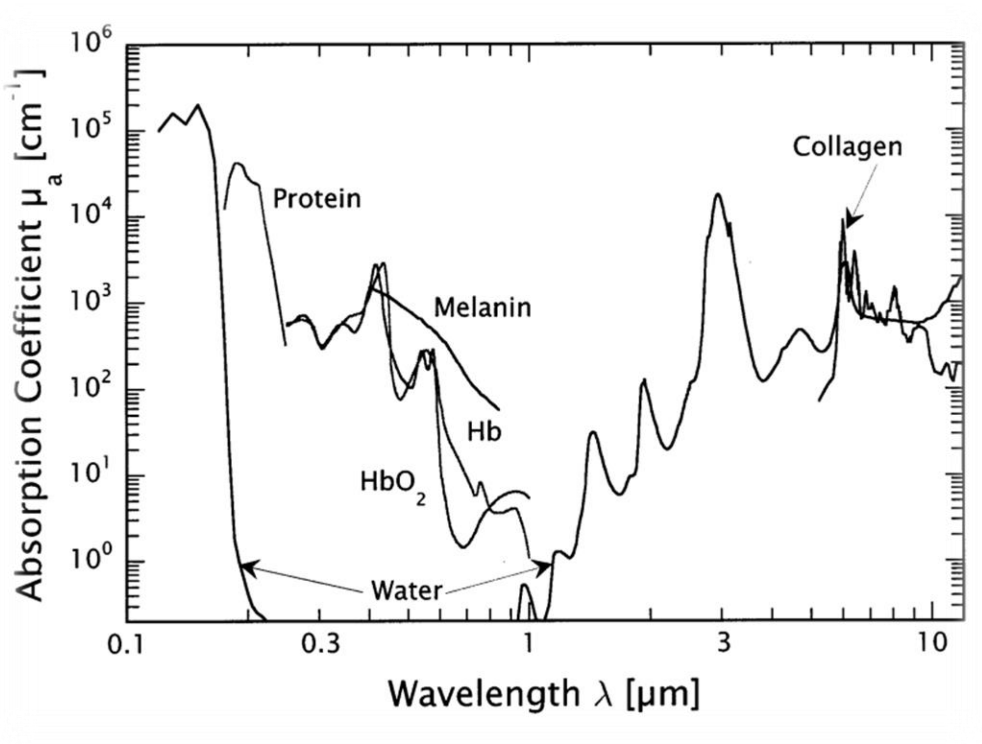

Figure 3.1: Optical absorption coefficients of soft tissue components: 0.1-10 μm spectrum [40].

When light is incident on a biological material, and the light is absorbed and then re-radiated at angles, it is referred to as scattered light. The total amount of scattering which occurs in the material is predicted by the probability of a scattering event happening, which is referred to as a scattering coefficient, μ_s. The scattering coefficient is defined as:

$$\mu_s = \sigma_s N \qquad 3.6$$

where σ_s is the effective scattering cross section and N is the number of scatterers per unit volume. The summation of the scattering μ_s and the absorption μ_a is known as the total attenuation coefficient, μ_t. The mean free path between interaction events is given by the reciprocal of the total attenuation coefficient, $\frac{1}{\mu_t}$. When absorption does not dominate over scattering, Beer's law can be written as:

$$I_t = I_o e^{-\mu_t x} \tag{3.7}$$

The spatial distribution of the irradiance of the scattered light is generated as a function of the size and shape of the inhomogeneities in the medium. The angular dependence of the scattered light can be determined by the Henyey-Greenstein phase function, which is a photon transport equation, and is used to describe a material where $\mu_s >> \mu_a$ hence;

$$p(\cos\theta) = \frac{1 - g^2}{2(1 + g^2 - 2g\cos\theta)^{3/2}} \tag{3.8}$$

where p is the probability of light scattering in a certain direction and g is the anisotropy factor. The anisotropy factor is the average cosine of the scattering angle. If the anisotropy factor is 1 or -1 then the light is observed as ballistic, and is fully forward scattering or fully backward scattering, respectively. If the anisotropy factor is zero, then the scattering is isotropic. Most soft tissues have an anisotropy factor varying between 0.7 to 0.98 leading to a scattering angle of 8° to 45° [32]. Establishing the large preference of photons to scatter forward and the large dependence on wavelength creates a deviation from the traditional Rayleigh and Mie scattering, but finds better agreement with the Henyey-Greenstein function to define the scattering of the photons.

Another parameter measured is the attenuation of scattered light with depth in tissue, which is approximated as the effective attenuation coefficient.

$$\mu_{eff} = \sqrt{3\mu_a(\mu_a + \mu_s')} \tag{3.9}$$

where μ_s' is the reduced scattering coefficient and considers the direction of the scatterers via the anisotropy factor.

$$\mu_s' = \mu_s(1 - g) \tag{3.10}$$

The optical penetration depth (OPD) is a measure of how far light will propagate through the tissue before the irradiance of the laser beam is reduced to 1/e (37%) of its initial value. It is simply calculated as the inverse of the effective attenuation coefficient, and OPD is given by δ. This is a simple method for estimating the OPD which uses the diffusion approximation to incorporate both scattering and absorption to obtain the OPD. A more robust and reliable method for analyzing photon propagation through tissue will be discussed in later chapters.

$$\delta = \frac{1}{\mu_{eff}} \tag{3.11}$$

When absorption and scattering is present in a biological sample it is referred to as turbid media. Blood vessels can be considered turbid media; we will define the optical albedo σ in equation 3.12. If the optical albedo equals zero then the photon is entirely absorbed. If the optical albedo equals one then then photon is entirely scattered with no absorption event occurring.

$$\sigma = \frac{\mu_s}{\mu_a + \mu_s} \tag{3.12}$$

The optical albedo term now needs to be added as a coefficient to equation 3.8 to allow it to approach zero for low scattering coefficients. The optical albedo is an important term when considering rapid dynamic tissue changes, for example optical coagulation which will be addressed in later chapters.

$$p(\cos\theta) = \sigma \frac{1 - g^2}{2(1 + g^2 - 2g\cos\theta)^{3/2}} \tag{3.13}$$

Absorption and scattering coefficients of biological samples can be approximated theoretically from the known sample composition and are also found experimentally with available reference tables. These values refer to the laser tissue interaction as a static process. However, dynamic changes in these values can occur under certain conditions (e.g. thermal coagulation or carbonization).

3.2: Dynamic Optical Properties of Soft Tissues

3.2.1: The Effects of Spot Size Variation on Optical Penetration Depth

Light, which is incident on soft tissue, penetrates the tissue as determined by its optical properties described in Section 3.1. However, for highly scattering materials, the size of the collimated beam can change the optical penetration depth, OPD. A smaller beam width can be associated with an increase in scattering, thus creating a shallower OPD. As the collimated beam width is increased, the scattering propagation of each photon has a greater possibility to propagate in the forward direction, which in turn creates a larger OPD, as observed in Figure 3.2 [33]. There is a greater probability of scattering effects overlapping in a forward propagation formation with a larger beam than that of a smaller beam. However, there is an upper limit to the relationship between beam width and OPD. The upper limit is generally defined when the beam gets so large that the scattering in the medium is saturated and the OPD will no longer grow with the beam expansion. This value is achieved with a 5-12 mm beam width [33]. Simulations have been performed using the Monte Carlo algorithm to show the statistical probability of photon propagation and the relationship between photon distribution and beam shape which will be explored more in future chapters.

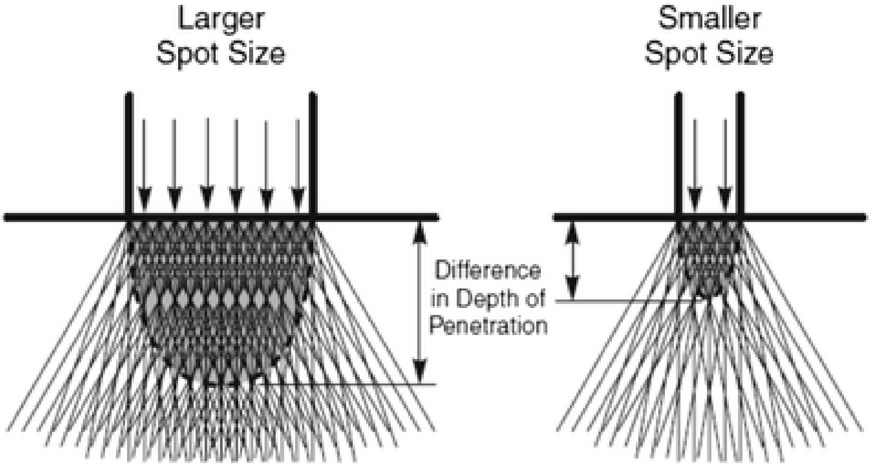

Figure 3.2: The overlapping scattering effects and the forward propagation of a larger beam spot leading to a deeper OPD [41].

3.2.2: Dynamic Tissue Responses to Heat

Biological tissue samples can also have a dynamic response to light. When the incident flux of light on the tissue alters the cellular makeup of the tissue, Beer's law no longer holds. There are three main classifications of dynamic light-tissue interactions: photochemical (absorption of photons by existing or added molecules in tissue which causes a biological cascade event), photomechanical (pulses of light which cause thermal expansion, or plasma, creating acoustic waves to break up biologic material), and photothermal (prolonged laser energy exposure which increases temperature in tissue). This dissertation will focus primarily on photothermal effects of light-tissue interactions, where light is converted into heat inside soft tissues. An example of a photothermal interaction is a high-power laser beam interacting with a biological sample over a period of time. The high-power laser will, over time, fundamentally irreversibly alter the protein structure in the tissue at a high fluence rate [42]. The protein structure undergoes thermal denaturation (coagulation) which directly effects the optical proprieties of the tissue. The predominant change is seen in the scattering coefficient. When creating a very large fluence rate relative to the tissue sample, the process of vaporization starts at the point when the water in the soft tissue starts to form gas bubbles. These bubbles and the rapid change in the tissue volume cause thermal decomposition. Carbonization of soft tissue might also occur under specific conditions. This happens when carbon atoms are released and charring occurs on the tissue surface. Properties of laser-tissue interactions, specifically coagulation, carbonization, and vaporization of porcine blood vessel will be discussed in detail in later chapters.

CHAPTER 4: BACKGROUND AND OVERVIEW

4.1: Wavelength Comparison for Laser Fusion of Blood Vessels

4.1.1: Infrared Laser Systems

As seen in Chapter 3 the selection of a wavelength for sealing and cutting vascular tissue is complex and multifaceted. In this section, the contributing factors impacting the wavelength selection process will be reviewed. The wavelength must be chosen to optimize the absorption into the specific makeup of a blood vessel. Ultraviolet (UV) radiation is strongly absorbed by proteins and water, both present in high concentrations in blood vessels, however UV radiation also has the ability to damage DNA, which eliminated these wavelengths from consideration. The visible spectral region has high hemoglobin absorption. Prior to laser irradiation of the blood vessel, the vessel region will be compressed between the jaws of the laparoscopic device, thus displacing any fluid (including blood) inside. Therefore, hemoglobin does not contribute as an absorber during vessel fusion. It is also noted that if some blood did remain in the treatment area, visible light at high power might cause the blood to clot creating internal blood clots for the patient. For these reasons, the visible spectrum was ruled out for testing. The IR spectrum does contain water and collagen absorption peaks. Both of these components are found in high quantities in a blood vessel (~ 70% water content) making the near-IR spectrum an ideal window for choosing a therapeutic wavelength for vessel ligation [56]. The optical penetration depth (OPD) in water as a function of laser wavelength is shown in Table 4.1 for the laser wavelengths used in this study [41].

During preliminary studies, seven different continuous-wave lasers spanning the entire near-IR spectrum were tested. These lasers included: an 808 nm, 30 Watt diode laser (Apollo

Instruments, Irvine, CA); a 980 nm, 50 Watt diode laser (Edwards Life Sciences, Irvine, CA); a 1075 nm, 50 Watt Ytterbium fiber laser (IPG Photonics, Oxford, MA); a 1470 nm, 40 Watt diode laser (QPC lasers, Sylmar, CA); a 1550 nm, 30 Watt Erbium fiber laser (IPG Photonics); an 1850-1880 nm, 5.5 Watt tunable wavelength Thulium fiber laser (IPG Photonics); and a 1908 nm, 100 Watt Thulium fiber laser (IPG Photonics).

4.1.2: Experimental Setup

A bulk optics setup was necessary for optimizing vessel sealing parameters. The benchtop experimental setup (Figure 4.1) mimicked the tissue contact aspects of a surgical instrument, while providing control over the experimental variables that might impact results (e.g. applied force, compression thickness, beam profile, etc.). This bulk optics setup delivered the infrared laser radiation through a 400-μm-core silica optical fiber, which could easily be integrated into a smaller handheld medical device. The bulk optics setup used two one-inch optics to first collimate and then focus the light. The second lens was a cylindrical lens which converted the collimated circular spatial beam profile to a focused linear beam profile. Collimating and beam shaping optical components were incorporated into the benchtop experimental setup to convert the Gaussian circular beam profile to a quasi-flat-top, linear beam profile, measuring 1 mm width by 12 mm length. This beam provided uniform distribution of laser power in a tight linear beam aligned perpendicular to the vessel direction for narrow, full-width thermal coagulation and sealing. The bulk setup also consisted of a compression stage mimicking the existing compression jaw designs used in surgical settings. On this compression stage, the blood vessel sample was sandwiched between a front glass slide and a back-metal faceplate with a glass slide insert. A compression gap stop of 0.4 mm was used to ensure uniform compression and consistency between different samples. The bulk setup also included a force meter (25 LBF, Chatillon, Largo, FL) to monitor the amount of force on the vessel sample. Laser energy was applied for 5 s to create a thermal seal in the clamped vessel.

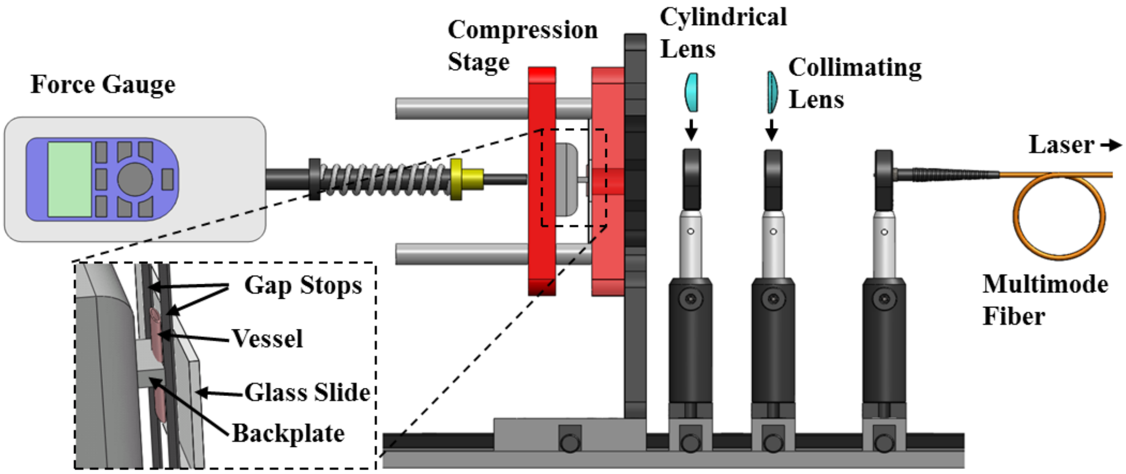

Figure 4.1: Diagram of experimental setup, including a mechanical force gauge mounted onto an optical rail system, cylindrical lens for beam shaping, and laser fiber.

4.2: Results

A general summary of qualitative vessel fusion success is provided in Table 4.1, including all of the near-IR lasers tested. During initial studies, several laser wavelengths were observed to produce minimal thermal alteration of the tissue and unacceptably low (< 100 mmHg, which is less than systolic blood pressure) vessel burst pressures. Such wavelengths were not studied in further detail. These laser wavelengths, including 808, 980, and 1075 nm, were all similar in that they provided optical penetration depths (OPD) that were too deep, on the scale of millimeters [41], rather than hundreds of micrometers, resulting in insufficient deposition and absorption of optical energy into the vessel during irradiation (Figure 4.2a). The majority of the laser energy was transmitted through the vessel walls, which were compressed to a thickness of 0.4 mm, rather than absorbed in the tissue. A brief experimentation with the application of higher laser powers and/or longer laser irradiation times could not compensate for this mismatch between OPD and tissue thickness.

Table 4.1: Summary comparison of continuous-wave infrared lasers used in this study.

Laser	Wavelength (nm)	Power (W)	OPD (mm)	Vessel Seal
Diode	808	30	1.5	No
Diode	980	50	1.5	No
Ytterbium Fiber	1075	50	3 - 4	No
Diode	1470	40	0.4	Yes
Erbium Fiber	1550	30	0.9	Yes
Thulium Fiber*	1850/1880	5.5	0.3 – 0.6	Yes
Thulium Fiber	1908	100	0.1	Yes

* Thulium fiber laser (1850/1880 nm) was limited to low power operation.

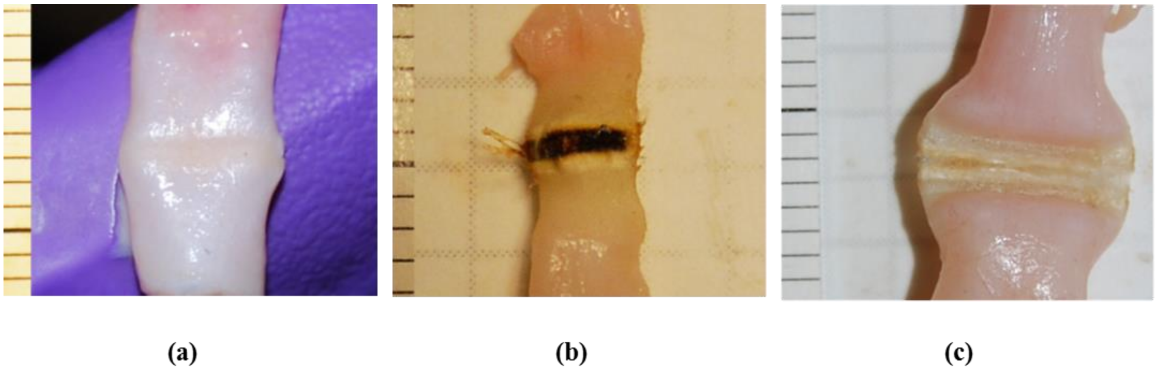

Figure 4.2: Photographs of the fusion regions for the porcine renal vessel samples. Ruler scale = 1 mm increments. (a) Unsuccessful fusion of a large (6-mm-diameter) vessel using the 1075 nm laser wavelength. Minimal thermal alteration of the tissue is observed; (b) Charred (4-mm-diameter) vessel fusion zone using the 1908 nm laser wavelength; (c) Successful fusion of a large (6-mm-diameter) vessel using the 1470 nm laser wavelength. A narrow, full width thermal coagulation zone extending ~ 1 mm on each side of the vessel seal site is visible.

Extensive studies performed with several other lasers produced improved results, but were limited by lower vessel seal pressures, excessive tissue charring, and/or low power output, which prevented treatment of large vessels. A comparison of the vessel burst pressures for these lasers is provided in Table 4.2. The 1850/1880 nm tunable thulium fiber laser was limited to operation at very low powers (5.5 W), so large vessels greater than 4 mm could not be sealed. The 1908 nm thulium fiber laser was limited by its shallow OPD (~ 0.1 mm), resulting in a steep thermal gradient, excessive charring on the front surface of the vessel, and borderline burst pressures for medium to large vessels (Figure 4.2 b). It was not possible to compress the vessels down to a thickness of only 0.1 mm for better matching with the OPD of the 1908 nm laser. On the contrary, the 1550 nm erbium fiber laser was limited by its large OPD (~ 0.9 mm) which did not match well with the compression thickness of the vessels (~ 0.4 mm), and also resulted in lower burst pressures for all vessel sizes. It should be noted that preliminary studies with the 1550 nm laser using a larger gap stop providing a compression thickness of ~ 0.8 mm to better match the wavelength's OPD did not result in improved vessel fusion, and was also unfeasible for smaller vessels, which simply fell out of the larger gap stop in the experimental setup. It should also be noted that one of our objectives was to have a single laser system and device capable of fusing all vessel sizes; this was not possible with a larger gap stop.

Table 4.2: Mean vessel seal burst pressure measurements as a function of laser power, irradiation time, and vessel size.

Wavelength (nm)	Power (W)	Time (s)	Vessel Size	BP (mmHg)	N
1470	31	5	Small (1.8 ± 0.2)	578 ± 154	6
			Medium (2.8 ± 0.5)	530 ± 171	10
			Large (4.4 ± 0.3)	426 ± 174	10
1550	29	5	Small (1.9 ± 0.2)	306 ± 87	6
			Medium (3.3 ± 0.4)	275 ± 83	8
			Large (5.2 ± 0.8)	264 ± 168	13
1850	4.3	5	Small (1.9 ± 0.2)	678 ± 134	5
			Medium (2.6 ± 0.3)	465 ± 105	17
	NA	NA	Large	NA	NA
1880	4.3	5	Small (1.8 ± 0.3)	507 ± 389	8
			Medium (2.5 ± 0.3)	484 ± 145	13
1880	NA	NA	Large	NA	NA
1908	NA	NA	Small	NA	NA
1908	16	5	Medium (2.9 ± 0.4)	397 ± 117	16
			Large (4.6 ± 0.3)	357 ± 195	9

The 532 nm frequency-doubled Neodymium:YAG (KTP) laser was also briefly explored, but this visible laser wavelength was not included in the study. In theory, KTP laser radiation is strongly absorbed by blood and would therefore appear to be an attractive option for fusing blood vessel walls. However, as mentioned earlier, during vessel sealing, the majority of blood normally located within the vessel lumen is displaced from the treatment area due to vessel compression, leaving no effective absorber for the 532 nm laser radiation, and hence, minimal thermal coagulation of the vessel was observed at this wavelength.

The 1470 nm diode laser wavelength produced rapid, precise, and strong vessel seals (> 426 ± 174 mmHg) over a wide range of vessel diameters (1-6 mm), with minimal thermal spread and charring (a lateral thermal damage width of 1.0 ± 0.4 mm including the seal was measured from the center of the seal to the end of the thermal coagulation zone) (Figure 4.2c and Table 4.3).

Table 4.3: Mean lateral thermal damage zones as a function of laser wavelength. Lateral thermal damage measurements were measured from the center of the seal.

Wavelength (nm)	**Thermal Damage (mm)**	**N**
1470	1.0 ± 0.4	15
1550	0.5 ± 0.3	21
1850/1880	0.4 ± 0.2	21
1908	0.8 ± 0.3	15

The 1470 nm laser wavelength produced the most consistent results over the widest range of vessel sizes with burst pressures exceeding the industry standard of three times the systolic blood pressure per vessel size.

4.3: Conclusion

In summary, a wide range of infrared lasers were tested in this preliminary study for thermal fusion of blood vessels. The 1470 nm diode laser was the most attractive laser due to its ability to fuse vessels ranging from 1-6 mm in diameter in a relatively short period of time (~5 s), with a narrow zone of collateral thermal damage (~ 1 mm including the seal) and minimal charring. The optical penetration depth for this wavelength closely matched the vessel compression thickness (~ 0.4 mm), thus providing high optical absorption and heat deposition in the tissue. The 1470 nm diode laser is also a relatively compact and affordable laser system capable of emitting high power.

While other laser wavelengths also produced reasonable results, they suffered from significant limitations. For example, the thulium fiber laser in the wavelength range of 1850-1880 nm produced strong fusion of small to medium vessels at very low power. A higher power system, not available during this study, may therefore warrant further investigation. However, it is worth noting that fiber laser technology in general is less efficient than direct diodes, since the fiber lasers themselves require diode laser pump sources for operation. While the primary advantage of the fiber laser is its improved spatial beam profile for beam shaping, it is not clear whether this provides any advantages in overall performance.

Although the seal strengths and lateral thermal damage zones obtained in this study are consistent with those published for radiofrequency and ultrasonic based surgical devices, more rigorous studies will be presented in future chapters in order to better understand the physical effect of temperature and pressure on the dynamic optical properties of the vessels during the procedure.

Chapter 4 has demonstrated the ability to seal blood vessels with laser energy. It shows that laser sealed blood vessels have a comparable seal strength and thermal damage region to competitive technology. In future chapters, it will be demonstrated that it is possible to reduce the infrared laser irradiation times from 5 s to 1 s by using higher laser power. Future chapters will also explore the possibility of cutting the blood vessel after it has been sealed using an optical approach (as opposed to a conventional mechanical blade, which is currently integrated in RF devices). With the optimization of other laser parameters, it may be possible to exceed the standards of current modalities and have a more rapid and precise method to seal and cut blood vessels.

CHAPTER 5: RAPID FUSION AND CUTTING OF BLOOD VESSELS *EX-VIVO*

5.1: Methods

Chapter 4 demonstrated the ability to successfully seal blood vessels using near-IR lasers. The optimal wavelength was determined to be at 1470 nm, which showed that a vessel compressed to match the OPD of 0.4 mm produced the highest and most consistent burst pressures. In this chapter, a higher power, 1470 nm, near-IR laser is explored. A higher power laser will provide the ability to both fuse and cut blood vessels in a more rapid, two-step optical process.

For this study, a total of 39 blood vessels were harvested ranging in outer diameter (OD) from 1.5 - 8.5 mm, and with a mean outer diameter of 3.6 mm ± 1.6 mm. Thirty of the 39 harvested vessels were sealed and cut with 55 vessel halves tested for burst pressures. Nine of the 39 harvested vessels were sealed and cut, resulting in 14 vessel halves preserved for processing and histologic analysis. During testing, the vessels were compressed to a fixed thickness of 0.4 mm. As mentioned in Chapter 3, water is the primary absorber of laser radiation in the near- to mid-IR spectrum, and soft tissues are composed primarily of water (~ 70% water content) [56]; the optical penetration depth (OPD) of 1470 nm radiation can be approximated by the water absorption coefficient ($\mu_a \approx 25\ \mathrm{cm}^{-1}$) [41] using Beer's Law (OPD ≈ 0.4 mm). This OPD also closely matches the compressed thickness of the blood vessels which provides more efficient delivery of light energy to tissue. A 110-Watt diode laser with a center wavelength of 1470 nm (BrightLase Ultra-500, QPC lasers, Sylmar, CA) was used for all of the studies in this chapter. The laser was operated in long-pulsed mode with a pulse duration of 1 s and at an output power of 110 W. This setup provided 90 W of average power incident on the tissue surface for thermal coagulation and vaporization. The laser power output was measured at a point after the beam shaping lenses by using a power meter (EPM1000, Coherent, Santa Clara, CA) and detector (PM-150, Coherent).

A similar bench top setup used in Chapter 4 was again used here to mimic the tissue contact aspects of a surgical instrument, while providing control over the experimental variables that may impact the future design of a handheld device. Infrared laser radiation delivered through an armored, 400-µm-core, low-OH, silica, optical fiber patch cord (QPC Lasers) was collimated to a 10-mm-diameter beam using a 35-mm-focal-length (FL) plano-convex lens (LA1951-C, Thorlabs, Newton, NJ). A second 100-mm-FL cylindrical lens (LJ1695RM-C, Thorlabs) was then used to convert the circular spatial beam profile to a linear beam profile (Figure 5.1).

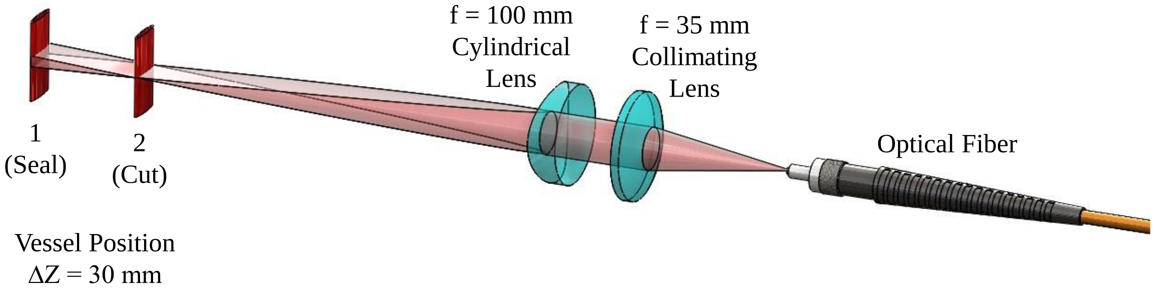

Figure 5.1: Diagram of linear beam shaping optics, as well as respective blood vessel positions used for infrared laser sealing and cutting.

Two distinct spatial beam profiles, for sealing and cutting, were achieved by translating the vessel position 30 mm along the optical axis, thus moving the tissue out of and into the focus for sealing and cutting, respectively. This resulted in a change in the power density ratio (sealing/cutting) by a factor of 2.7. These two linear beams (Figure 5.2), aligned perpendicular to the vessel direction, were imaged with an IR spatial beam profiler (Pyrocam III, Spiricon, North Logan, UT).

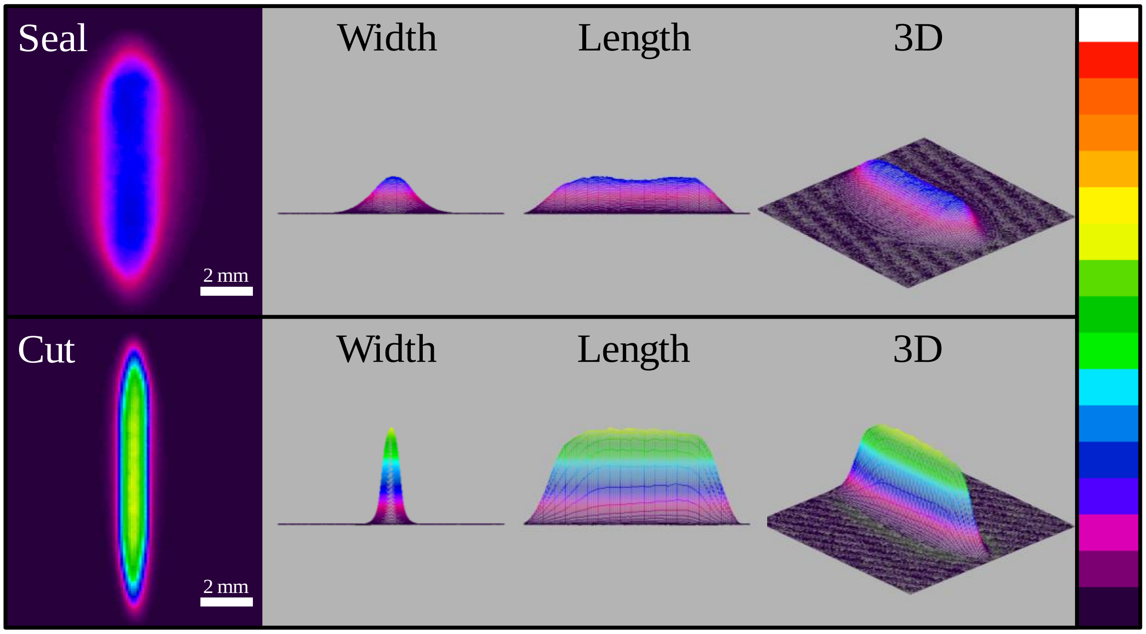

Figure 5.2: Dimensions of the sealing and cutting laser beam taken with an infrared beam profiler. The sealing beam measured 3.0 x 9.5 mm (FWHM) and the cutting beam measured 1.1 x 9.6 mm (FWHM), with a cutting / sealing beam irradiance ratio of 2.7 (1080 W/cm^2 versus 400 W/cm^2). The color scale representing beam irradiance is in arbitrary units but is consistent in scale between the seal and cut beam measurements.

The seal beam measured 9.5 mm long by 3.0 mm wide (FWHM) (power density of 400 W/cm^2) and the cut beam measured 9.6 mm long by 1.1 mm wide (FWHM) (power density of 1080 W/cm^2). The vessel sample was sandwiched between a 1-mm-thick front glass slide and a 5-mm-wide back metal faceplate with a glass slide insert, similar to the previously discussed bench top setup [51]. The gap between the tissue contact surfaces when fully closed was fixed at 0.4 mm in the experimental setup to provide tissue compression closely matching the OPD of the laser wavelength. A force meter (25 LBF, Chatillon, Largo, FL) monitored the amount of force applied to the vessel sample, which was held constant at 724 kPa (~ 105 psi). Laser energy was delivered in long-pulsed mode. This was first delivered with the seal beam dimensions for 1.0 s, to create a thermal seal in the clamped vessel. The clamped vessel was then translated 30 mm before cutting the vessel with an additional 1.0 s of laser irradiation at the beam focus. This large translation distance was a function of the cylindrical lens’s long focal length, required for adequate optical element spacing in our bench top vessel compression setup. The sealing and cutting times of 1 s each were chosen based on earlier preliminary studies that showed this to be the shortest period of time, at maximum laser power, that produced both strong seals and consistent cutting of a wide range of blood vessels.

5.2: Results

Figure 5.3b shows a representative image of a blood vessel sealed and cut using the high power 1470 nm laser. Burst pressure data points (each representing the average of each side of the seal) as a function of the exact vessel diameter (mm) are plotted in Figure 5.4. Normal systolic blood pressure (120 mmHg) and hypertension blood pressure (180 mmHg) are labeled in the Figure 5.4 for reference. Mean burst pressures measured 1305 ± 783 mmHg (*n* = 55 vessel halves) with a minimum value of 415 mmHg recorded for a 3-mm-OD vessel. As can be seen in the graph, there were no vessel sealing failures (< 180 mmHg).

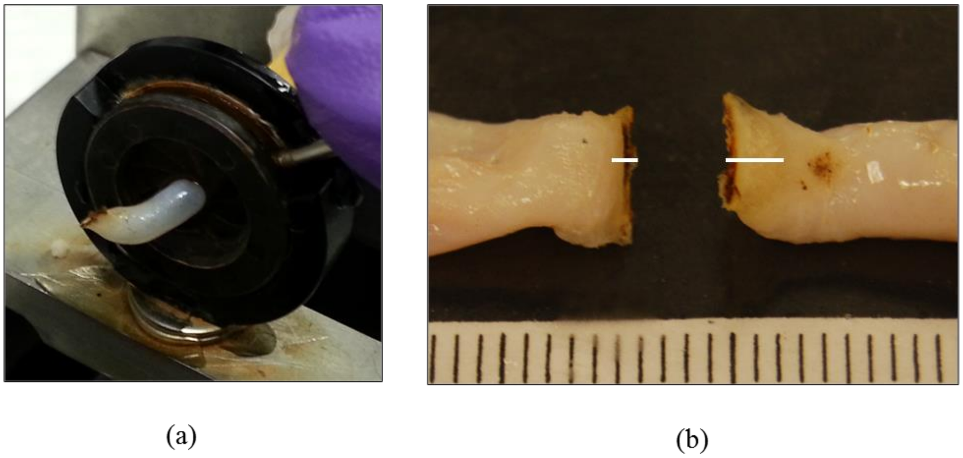
(a) (b)

Figure 5.3: (a) Close-up view of sealed and cut 2.1 mm vessel enclosed in the iris during burst pressure testing. The vessel withstood a burst pressure greater than 800 mmHg. (b) Representative image of 5.2 mm vessel after sealing and cutting (white lines indicate extent of lateral thermal damage including the seal). This vessel withstood burst pressures greater than 3000 mmHg. (Ruler increments = 1 mm).

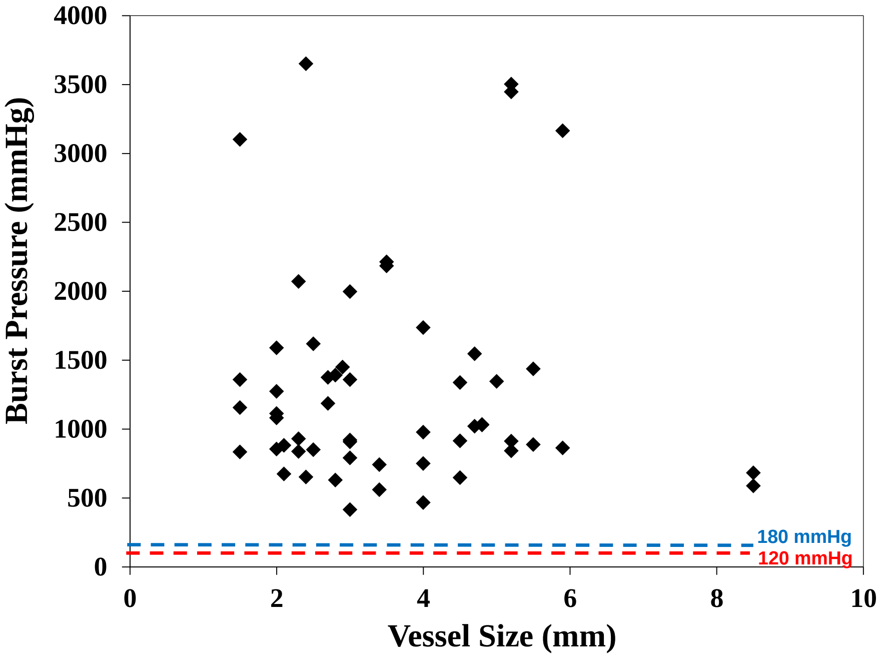

Figure 5.4: Vessel burst pressures plotted as a function of vessel size. Mean burst pressures measured 1305 ± 783 mmHg (*n* = 55 vessel halves) with a minimum value of 415 mmHg recorded for a 3-mm-OD vessel. Normal systolic blood pressure (120 mmHg) and hypertension (180 mmHg) thresholds are labeled for reference. All vessel halves tested burst above both of these thresholds.

5.3: Discussion

This chapter has shown that the high power 1470 nm diode laser is capable of consistently producing strong seals in a wide range of porcine renal vessel sizes, *ex vivo*. A two-step technique, combining both optical-based sealing and transection of vessels was demonstrated. The 2 s total irradiation time was comparable to (or slightly better than) other clinical radiofrequency and ultrasonic energy-based devices, which typically take 3 s or greater to seal and cut vessels, as seen in Table 5.1. It was postulated that larger seal regions would increase burst pressures; however, the beam widths used in this study were limited to 4 mm to allow for potential future integration into a standard 5-mm-outer-diameter laparoscopic device.

Table 5.1: Published ranges of mean values for seal time, burst strength, and thermal spread for commercially available vessel sealing devices [27,28,34,35].

Device	**Energy Source**	**Seal Time (s)**	**Burst Strength (mmHg)**	**Thermal Spread (mm)**
LigaSure™	RF	3.0 - 10.0	380 - 885	2.2 - 4
Harmonic Scalpel™	US	3.3 - 14.3	204 - 921	1 - 1.9
Gyrus PK™	RF	4.0 - 11.1	290 - 648	UK
EnSeal™	RF	4.1 - 19.2	255 - 928	1.1
This study	*Laser*	*2.0*	*1305*	*0.94*

It should be noted that blood pressure through a vessel varies proportionally with the size of the vessel [55]. In this chapter, all of the vessels tested exceeded both the normal systolic blood pressure of 120 mmHg and the severely elevated blood pressure levels of 180 mmHg, experienced during malignant hypertension. Histologic measurements showed about 1 mm of thermal damage. These values are similar to or less than those typically created by using RF or ultrasonic devices (Table 5.1).

5.4: Conclusion

In summary, this chapter describes several significant accomplishments. First, both sealing and cutting were consistently achieved in a wide range of vessels (1.5 – 8.5 mm) with a 100% (55/55) success rate. Second, the total laser irradiation time was only 2 s, comparable to other energy-based devices currently used in surgical procedures. Third, vessel burst strength averaged over 1300 mmHg, with the weakest vessel seal having a burst pressure of 415 mmHg, well above both normal systolic (120 mmHg) and hypertensive (180 mmHg) blood pressures. Although the bench top experimental setup described in this chapter was capable of sealing and cutting blood vessels, the matrix of parameters is vast. For optimizing these procedures, the next chapter will focus on simulating beam profiles and the interactions with compressed blood vessels to optimize the complex matrix of parameters.

CHAPTER 6: MODELING DYNAMIC OPTICAL PROPERTIES OF BLOOD VESSELS

6.1 Introduction

Previous chapters demonstrated the ability of IR laser sealing and cutting of blood vessels. Up to this point, the only optimization which had been performed in these experiments were benchtop design of experiment (DOE) studies. These DOE studies were aimed to optimize the benchtop setup through variation in the setup and statistical analyses. The most effective linear beam profiles tested utilize the optical beam density in a two-step method, first sealing (thermal coagulation) and second cutting (vaporization) of blood vessels. The sealing beam has a slightly wider dimension and lower irradiance, which provides a sufficient coagulated tissue to produce a seal. The cutting beam has a narrower dimension and higher irradiance, which vaporizes the soft tissue, leaving two equally coagulated halves of a bisected blood vessel. Simplified assumptions were made for these experimental studies such as considering the OPD of a blood vessel the same as the OPD in water at specific wavelengths. This is a rough approximation which works relatively well for static conditions. However, when high-power laser radiation is applied to soft tissue for any period of time, the hydration level and temperature of the soft tissue will change significantly. As discussed in previous chapters, a temperature rise produces thermal coagulation which results in a dynamic response to the optical properties of tissue. Since the matrix of laser and tissue parameters is vast, it is not practical to test all scenarios experimentally.

In this chapter, the two-step sealing and cutting method will be further explored through simulations for low (< 25 W), medium (< 100 W), and high (200 W) power diode lasers at a wavelength of 1470 nm. A standard three-step method will be used for this analysis: (1) Monte Carlo (MC) model of photon transport in tissue, (2) a heat transfer model to map maximum tissue temperatures, and (3) a tissue damage model to quantify thermal spread and coagulation zones. Coagulation and cutting laser beam profiles were optimized for specific temperatures based on optical beam density. The results were then compared with experimental vessel burst pressures quantifying the effectiveness of optimizing bifurcated seal zones (BSZ), whenever possible (200 W laser was not available for benchtop testing).

When creating a more robust model for sealing and cutting blood vessels, there are several different parameters which can alter the expected simplified model's outcome. A flat-top linear beam was used for all simulations with variable beam profiles (1-5 mm widths and 8.0-9.5 mm lengths), incident powers (20-200 W) and irradiation times (0.5 - 5.0 s). The constants in the model were the fixed thickness of 400 µm, matching an insert in the jaws of the laparoscopic device. As discussed in previous chapters, tissue compression displaces the blood away from the seal area and widens the effective tissue width; therefore, it is not necessary to include a layer of blood in the model. The simulations also represent a tissue with a widening effect of 50% its original diameter (Figure 2.4). For example, a 6 mm wide blood vessel is compressed to a 9 mm wide blood vessel. All simulations were performed with compressed vessel size matching the exact beam length to maximize efficiency of the beam irradiance.

In order to explore the details of laser tissue interactions, a combination of a Monte Carlo simulation, thermal mapping, and Arrhenius integral thermal damage simulation will be utilized. Simulations will be conducted at a wavelength of 1470 nm and with beam spot sizes as listed above to predict how light will be absorbed, temperature will rise over time, and when coagulation and ablation of blood vessels should be expected. The understanding of these parameters is critical in further optimizing sealing and cutting techniques and to developing a laparoscopic device.

The three-step process using three linked models will be used to predict successful laser sealing and cutting of blood vessels, include:

Step 1: Monte Carlo (MC) simulation of light transport in a compressed homogeneous tissue layer with a resulting map of photon absorption and energy deposition.

Step 2: Heat transfer simulations, using the input energy distributions from the MC model to determine starting temperatures, and then mapping the temperature rise as a function of time and spatial location.

Step 3: Thermal tissue damage simulations using an Arrhenius integral model, to determine whether the tissue has achieved a specific temperature for a sufficient period of time to be irreversibly damaged through thermal coagulation and protein denaturation.

The following sections describe these three phases and models in more detail.

6.2: Methods

6.2.1: Bifurcated Seal Zone

Coagulation and cutting laser beam profiles were optimized for specific temperatures based on optical beam density. The results were then entered into equation 6.1 for computing burst pressures, and also compared with experimental vessel burst pressures, quantifying the effectiveness of optimizing the bifurcated seal zone (BSZ), when possible. The bifurcated seal zone (BSZ) was defined by the following formula:

$$\text{BSZ} = (\text{thermal seal zone} - \text{ablation zone}) / 2 \tag{6.1}$$

where thermal seal zone was total distance across the thermally coagulated and sealed vessel before bisection, and ablation zone was the central part of the thermal seal zone that had been vaporized and removed for cutting. After cutting, two separate segments of sealed tissue were left, one on each side of the bisected vessel, referred to as the BSZ (Figure 6.1).

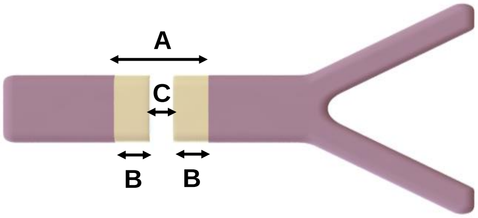

Figure 6.1: Representation of a sealed and cut vessel, showing how (A) thermal seal zone, (B) bifurcated seal zone, and (C) ablation zone were measured.

The BSZ is an important feature of a sealed and cut blood vessel. Once a blood vessel has been sealed and cut, the blood will reenter the treated area of the blood vessel lumen and create an internal pressure vessel at the end cap or BSZ. A healthy region of blood vessel can be approximated to be a thin walled pressure vessel [57]. However, unlike healthy blood vessel walls, the BSZ has been coagulated and has lost some of its elasticity. This creates a weak point at the end cap of the pressure vessel. If the BSZ is not sufficiently thick to sustain the blood flow pressure, then the BSZ becomes the first point of failure and the vessel will burst. A simplistic mathematical expression was used to estimate internal pressure on BSZ as a longitudinal stress in a cylindrical case on a flat circular end cap, provided in (6.2) [58]:

$$\sigma_{max} = [3a^2 (3m + 1) P] / 8mt^2 \qquad 6.2$$

where σ_{max} is the maximum stress at the center of the end cap, P is the pressure uniformly distributed over the end cap, a is the radius of the end cap, t is the thickness of the end cap, and m is the reciprocal of the Poisson's ratio (the expansion of the blood vessel wall perpendicular to the loading direction). Equation 6.2 is most accurate when the thickness of the end cap is no thicker than one-quarter of the effective diameter (ED) of the vessel. The burst or failure of the vessel will occur when the maximum stress is equal to the tensile strength of the material. The internal pressure of the vessel increases when the longitudinal stress on the BSZ increases. For a large BSZ value (within one-quarter of the ED), it is possible to inflate the thickness value, t, and create a seal that can withstand larger internal pressures which can be estimated with equation 6.2.

6.2.2: Step 1: Monte Carlo simulations for photon distribution

A standard Monte Carlo (MC) program in MATLAB [59] was adapted for these studies. MC simulations use a statistical "random walk" method to model light propagation, where tissues are assigned absorption and scattering coefficients as probability distributions that determine events [60]. The program determines the scattering angle and tracks multiple events for each photon. These vectors are a function of the total attenuation coefficient μ_t which is the sum of absorption (μ_a) and scattering (μ_s) coefficients. The photon deposits an amount of its energy in each of these locations and is re-weighted based on the tissue optical properties. The change in the weight of the photon (ΔP) is given by equation 6.3:

$$\Delta P = \mu_a / (\mu_a + \mu_s) \qquad 6.3$$

The photon then carries its new weight when it takes its next step forward in the tissue. This process continues until the photon weight is reduced to a fraction of its original weight. MC output provides the radiated energy density distribution as a function of space in tissue.

To simulate distribution of photons deposited into a compressed blood vessel, a plane parallel geometry was used. This is a valid assumption for cylindrical vessels compressed and flattened within the device jaws. Three million photons were simulated to achieve sufficient (4 μm axial) spatial resolution and distribution of light absorbed in tissue. Optical properties of normal and coagulated aorta at 1470 nm under compression of 195.8 kPa were extrapolated from existing literature and used for these simulations [61-62]. When aorta tissue is transformed from its normal to coagulated state, the scattering coefficient at 1470 nm rises approximately 34%, while the absorption coefficient remains relatively constant [62]. At 1470 nm, the anisotropy factor was assumed to remain constant between normal and coagulated tissue, consistent with only small fluctuations reported in previous studies [63]. Therefore, compressed normal tissue optical properties were used in the first step (sealing beam) and coagulated compressed tissue optical properties were used in the second step (cutting beam) for all two-step simulated procedures (Table 6.1). It should be noted that although the optical properties of laser irradiated tissue are dynamic and continuously change, for this study, simulations incorporated a discrete transformation of tissue optical properties.

Table 6.1: Optical parameters of normal and thermally coagulated, compressed tissue at a wavelength of 1470 nm [61-62,64].

Parameter	**Normal, Compressed**	**Coagulated, Compressed**
Seal beam length (mm)	8.0 – 9.5	NA
Seal beam width (mm)	2.0 – 5.0	NA
Cut beam length (mm)	NA	8.0 – 9.5
Cut beam width (mm)	NA	1.0 – 1.5
Absorption coefficient, μ_a (mm^{-1})	2.04	2.04
Scattering coefficient, μ_s (mm^{-1})	26.7	35.7
Anisotropy factor, g	0.875	0.875
Refractive index, n	1.52	1.52
Tissue thickness (mm)	0.4	0.4

6.2.3: Step 2: Thermal Heat Transfer Model

Tissue temperature simulations were conducted using an additional add-on module to the MATLAB program [59]. This model was directly integrated into the MC simulation inputs. As discussed in Chapter 3, when a photon is absorbed in soft tissue it converts its energy into heat. This heat causes the tissue temperature to rise. Mapping this rise in temperature over time is one goal of this chapter. Since long pulse durations (1-5 s) are being simulated based on the previous experimental studies, a heat transfer equation (HTE) will be used to determine heat dissipation over time in soft tissue [65&66]. The HTE is given by:

$$-\Delta T(\boldsymbol{r},t)+\frac{1}{\alpha}\frac{\partial T}{\partial t}(\boldsymbol{r},t)=\frac{1}{k}S(\boldsymbol{r},t) \qquad 6.4$$

where, T, is the temperature at point $\mathbf{r}$ and time t, k is the thermal conductivity, α is the thermal diffusivity, $\alpha=\frac{k}{\rho c}$ where ρ and c are the density and specific heat, respectively. S is the source term which is based on the absorption coefficient and irradiance and found by the equation below [59].

$$S(\boldsymbol{r}) = \mu_a(\boldsymbol{r})\varphi(\boldsymbol{r}) \tag{6.5}$$

These equations will be used for a simulation study conducted with a finite element model used for heat distribution solutions. The map of absorbed photons fluence rate and corresponding weight distributions from the MC simulations will be used as the input with mesh sizes in a MC add-on for temperature analysis. The combined blood vessel layers provided in Chapter 2 will be represented as a single homogeneous unit mesh of the simulation. The tissue layer was represented using thermal properties from the literature with a volumetric heat capacity of c = 3.5 J/cm^3-°C and thermal conductivity of k = 0.0062 W/cm-°C (Table 6.2) [66]. The initial tissue temperature was set at body temperature, T_0 = 37 °C.

Table 6.2: Thermal parameters for aorta tissue [66].

Parameter	Value
Initial temperature, T_0 (°C)	37
Volumetric heat capacity, c (J/cm^3-°C)	3.5
Thermal conductivity, k (W/cm-°C)	0.0062

Temperature is an important parameter during laser tissue interactions since it dictates if the tissue will be coagulated (sealed) or vaporized (cut). When soft tissue temperature rises, it experiences different stages which alter its physical and optical properties. At 100 °C, water begins to evaporate from the tissue. From 100-300 °C, a permanent seal of the vessel lumen starts to form. When tissue experiences temperatures of 300-400 °C, the tissue will begin to carbonize and char. Temperatures of 400-600 °C are sufficient to vaporize the tissue [67-76]. In this study, the objective for the first step, sealing (thermal coagulation), is to achieve a maximum tissue temperature of between 100-300 °C with the sealing beam profile. For the second step, cutting (vaporization), the goal is to achieve a maximum tissue temperature of 400-600 °C.

6.2.4: Step 3: Arrhenius Integral Thermal Damage Model

A standard Arrhenius integral model was used in MATLAB [59] to predict thermal injury using values for the frequency factor, ζ, and activation energy, E_a, from the literature, where $\zeta = 5.6 \times 10^{63}$ s^{-1} and $E_a = 4.3 \times 10^5$ J/mol (Table 6.3) [75].

Table 6.3: Tissue damage parameters for aorta tissue [75].

Parameter	Value
Frequency factor, ζ (s^{-1})	5.6×10^{63}
Activation energy, E_a (J/mol)	4.3×10^5
Universal gas constant, R (J/mol-K)	8.32

Tissue damage was bundled into a single parameter given by $\Omega(t)$. The temperature-time simulation data was compiled in a standard Arrhenius integral formulation in the form of a first-order chemical rate process equation used to determine thermal damage and tissue coagulation, as provided in equation 6.6 [45, 77-79].

$$\Omega(t) = \zeta \int_0^\tau \exp(-\frac{E_a}{RT(t)})dt \qquad 6.6$$

In equation 6.6, the integral time begins and ends with the laser irradiation time (t), where ζ is a frequency factor, E_a is activation energy of the transformation, R is universal gas constant, and T is absolute temperature. This integral is solved for each volume element, which will be predefined depending on the tissue geometry of the compressed blood vessel. This integral provides a ratio of damage of proteins before, C_b, and after heating, C_a. The ratio is calculated as equation 6.7:

$$\Omega(T,t) = -\ln (C_a / C_b) \qquad 6.7$$

The equation above can be transformed into a more meaningful form in equation 6.8:

$$\%C_{damage} = \%C_b\,(-e^{-\Omega(T,t)} + 1) \qquad 6.8$$

where $\%C_{damage}$ is percent damage to the proteins.

The simulated thermal damage sensor was placed in the center of the collapsed lumen, the most critical part of the blood vessel for the seal and cut procedure. Thermal damage was calculated for both sealed and cut beam profiles. The damaged cut profiles were observed as fully vaporized (ablated) tissue and subtracted from the thermal seal zone. The thermal seal zone was then divided by two because it would have been bisected by the cut profile (equation 6.1). This final calculation provided an accurate representation of the bifurcated seal zone (BSZ) on a blood vessel bisected by the laser, as confirmed in previous experimental studies as seen in Chapters 4 and 5. The BSZ was then correlated with experimental burst pressures to predict burst pressures for parameters that could not be tested in the laboratory. The BSZ was then substituted into equation 6.2, with an inverse Poisson ratio of 2 [80], and a tensile strength of 0.52 MPa [81], for an estimation of the burst pressure of a blood vessel with a diameter of 3.2 mm (the average experimental vessel size in our studies prior to compression).

6.3: Experimental setup

Both low and medium power 1470 nm laser diodes were tested experimentally in the laboratory; the high powered (200W) was unavailable for testing. Porcine renal blood vessels with mean outer diameters of 3.2 ± 1.4 mm, and a total sample size of n = 94, were harvested from fresh porcine kidney pairs and then stored in saline prior to same day use as described in Chapter 2. Blood vessels were tested on an experimental benchtop setup designed to mimic surgical instrumentation, compressing vessels to a fixed 0.4 mm thickness, as previously explained in Chapter 5. Each test was paired with two distinct spatial beam profiles: one for sealing and another for cutting. The change in beam size, which resulted in a change in fluence or energy density, was achieved by translating the vessel position along the optical axis. Beams were measured at FWHM and found to have small variations from the simulations, as a true flat-top beam profile could not be achieved in the laboratory. It should be noted that due to the high scattering coefficients for both native and coagulated blood vessels at the wavelength of 1470 nm, the photons undergo multiple scattering events through the compressed vessel thickness of 400 μm during the procedure, resulting in an altered and homogenized beam within the tissue, so small variations in the incident spatial beam profile probably are not significant.

Standard burst pressure measurements were conducted as discussed in Chapter 2, with the maximum pressure (in mmHg) corresponding to when a vessel seal burst. A seal was judged to be successful if its burst pressure exceeded both normal systolic blood pressure (120 mmHg) and hypertensive blood pressure (180 mmHg). The maximum burst pressure was recorded and correlated to the simulated BSZ. The BSZ was then measured for randomly selected blood vessels using photographs and pixel counting in ImageJ software. The 200 W laser was not available for experimental testing in these studies, but was simulated in these studies since 1470 nm diode lasers are commercially available at powers up to 200 W. It was possible to identify a trend in burst pressure versus BSZ data which helped to predict burst pressure results for the 200 W laser setting.

6.4: Results

A wide range of linear beam profiles (1-5 mm widths and 8-9.5 mm lengths), incident powers (20-200 W) and irradiation times (0.5 - 5.0 s) were simulated for low (~ 25 W), medium (~ 100 W), and high (200 W) power, 1470 nm diode lasers. Table 6.4 represents the optimal peak seal (coagulation) and cut (ablation) beam profiles with the shortest irradiation time for each laser power. Surgeons typically perform numerous blood vessel ligation applications during a single clinical procedure, so it is important to determine the optimal laser parameters that provide the shortest seal and cut times.

Table 6.4: Calculated and experimental BSZ and corresponding experimental BP measurements for low, medium, and high-power lasers [75].

Power (W)	**Seal/Cut Time (s)**	**Seal/Cut Beams (mm)**	**Calculated BSZ (mm)**	**Measured BSZ (mm)**	**Measured BP (mmHg)**
24	5 / 5	8 x 2 / 8 x 1	0.4	0.5 ± 0.2	457 ± 135
95	2 / 2	9 x 5 / 9 x 1.5	1.5	1.5 ± 0.4	1268 ± 771
90	1 / 1	9.5 x 3 / 9.5 x 1	0.9	0.9 ± 0.5	1305 ± 783
200	0.5 / 0.5	9 x 3 / 9 x 1	0.9	NA	NA

Figure 6.2 provides examples of both one- and two-dimensional plots of the Monte Carlo optical simulations for the 9 x 5 mm laser sealing beam. The fluence has a peak just below the surface of the vessel, due to contributions from back-scattered photons, and then follows an exponentially decaying trend. The chaotic color-coded data on the left and right sides of the 2D plot is due to enhanced light scattering effects along the periphery or edges of the laser beam width.

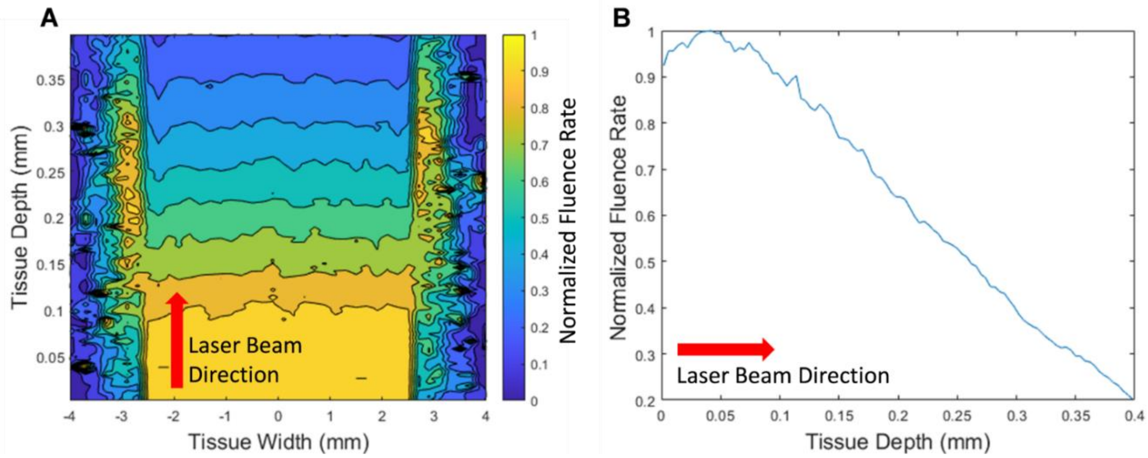

Figure 6.2: Center slice of Monte Carlo plots of the optical absorption for 3 million photons in the vessel for the laser parameters of 9 x 5 mm. (A) 2D plot; (B) 1D plot. This distribution of absorbed photons correlates with temperature, where temperature on the backside of the vessel is the lowest.

The simulation results for the thermal seal zones and ablation zones are provided in Tables 6.5 and 6.6 for the laser parameters studied. Maximum temperatures reported refer to the temperature at the backside of the vessel.

Table 6.5 shows the correspondence between fluence (energy density) and maximum temperature for the first step, laser coagulation and sealing of the vessel. Maximum tissue temperatures varied from 200 to 300 °C, within the temperature range necessary for significant BSZ for successful seals. Table 6.5 also shows the close correlation between the laser beam width (2 - 5 mm) and thermal seal zone or coagulated region on the vessel (2.2 - 4.8 mm).

Table 6.5: Thermal seal zones and maximum temperatures for vessel sealing.

Fluence (J/cm^2)	**Maximum Temperature (^{o}C)**	**Seal Beam (mm)**	**Thermal Seal Zone (mm)**
750	290	8 x 2	2.2
422	272	9 x 5	4.8
315	211	9.5 x 3	3.0
370	227	9 x 3	3.0

Similarly, Table 6.6 shows the correspondence between fluence and maximum temperature for the second step, laser ablation and cutting of the vessel. Maximum tissue temperature ranged from 500 to 750 °C, above the minimum temperature necessary for successful vessel ablation, Table 6.6 also shows the close correlation between the laser beam width (1.0 - 1.5 mm) and ablation zone or cut region on the vessel (1.2 - 1.8 mm).

Table 6.6: Ablation zones and maximum temperatures for vessel cutting.

Fluence (J/cm^2)	**Maximum Temperature (^oC)**	**Cut Beam (mm)**	**Ablation Zone (mm)**
1500	755	8 x 1	1.4
1407	682	9 x 1.5	1.8
947	496	9.5 x 1	1.2
1111	558	9 x 1	1.2

The BSZ was then calculated from equation 6.1 to be in the range of 0.4 to 1.5 mm (Table 6.4) which corresponded closely to previously measured and reported BSZ values (Figure 6.3A). These simulated BSZ were compared with gross images of BSZ and with both simulated and experimental burst pressures. A trend emerged of lower BSZ corresponding to lower burst pressure values (Figure 6.3B). Seal zones and burst pressures were plotted with error bars represented from experimental data evaluations and previous data seen in Chapters 4 and 5. It should be noted that experimental studies were performed with sealing beams tested without a second stage cutting beam present. Results showed high burst pressures, but no vessels were bifurcated. Similarly, cutting beams were tested without an initial sealing beam stage and blood vessels were all bifurcated, however, burst pressures were lower than accepted values (< 170 mmHg). These results confirmed that simulation temperatures were accurate and verified the need for a two-step, sequential, sealing and then cutting method.

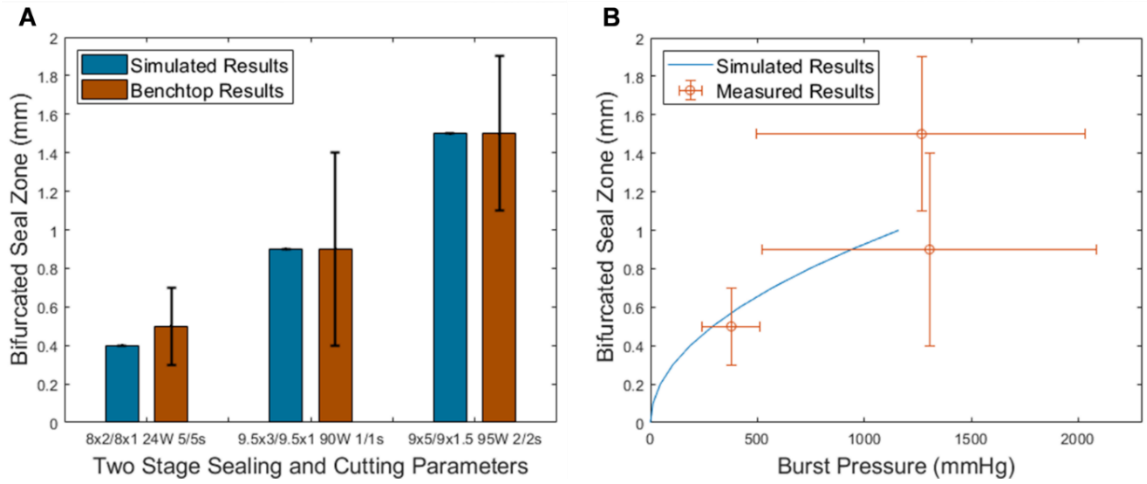

Figure 6.3: (A) Simulated BSZ (Blue) and gross measured experimental BSZ (Red) corresponding to optimum parameters in Tables 6.5 & 6.6. (B) Prediction of burst pressures by using only simulated bifurcated seal zones (BSZ), where BSZ = (thermal seal zone – ablation zone) / 2 and Equation 2 up to one-quarter of the vessel width. These BSZ values were compared to experimental burst pressure measurements. These measurements show a trend where larger BSZs resulted in larger burst pressures. There is also a cap to this increase of burst pressures, which levels out at a simulated BSZ of about 0.9 mm.

Figure 6.4 shows representative photographs of the experimental BSZ for each of the three laser settings tested, corresponding to the laser parameters in Table 6.5 and Table 6.6 the simulated BSZ and burst pressure data points shown in Figure 6.3.

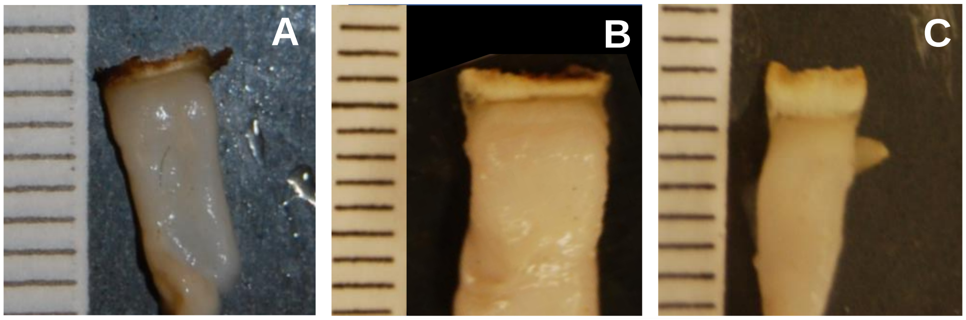

Figure 6.4: Photographs of experimental seals. Ruler lines are in millimeter scale. (A) 24 W (low power), 5 s seal / 5 s cut times, 8 x 2 mm seal beam, 8 x 1 mm cut beam dimensions, with BSZ of 0.47 mm; (B) 90 W (medium power), 1 s seal / 1 s cut times, 9.5 x 3 seal beam, 9.5 x 1 mm cut beam dimensions, with BSZ of 0.93 mm; (C) 95 W (medium power), 2 s seal / 2 s cut times, 9 x 5 mm seal beam, 6.5 x 1.5 cut beam dimensions, with BSZ of 1.6 mm.

6.5: Discussion

Preliminary computer simulations demonstrated the ability to predict and optimize the optical linear beam profiles for both sealing and cutting of blood vessels, utilizing a two-step variable optical beam density technique. Use of higher power lasers shortened vessel seal and cut times, while lower power lasers yielded times similar to other clinical ultrasonic and radiofrequency energy-based devices.

The trends and large error bars associated with the burst pressure measurements in Figure 6.3 can be explained. There were differences in burst pressures for BSZ lower than 0.9 mm. However, for a BSZ above 0.9 mm, burst pressures did not increase. The large standard deviation observed in the burst pressure measurements may be attributed to the range of the vessel sizes tested. Vessels with larger diameters have a smaller wall width and larger radius and are exposed to higher tensions and are more likely to burst at lower pressures, which is confirmed by Laplace's law [55,82]. However, a BSZ of 0.9 mm or higher makes this issue irrelevant since physiological blood pressures larger than 2000 mmHg are not encountered. Alternatively, when smaller blood vessels are compressed they do not stretch to the entire length of the laser beam and therefore do not absorb the entire laser energy deposited, which can also translate into lower experimental burst pressures. However, these are conflicting factors since blood pressure is proportional to blood vessel size, and smaller vessels only need to tolerate lower burst pressures to maintain hemostasis.

There are several limitations of these preliminary simulation studies. First, the optical properties of tissues are dynamic and non-linear in nature, and thus change at a continuous rate, for example, phase changes at temperatures above 100^{o} C. However, these computer simulations only incorporated a discrete transformation of optical tissue properties, which occurred at the moment the beam shape changed from a sealing to a cutting beam. This discrepancy may affect how light is deposited in the tissue, which could also translate into different values for the thermal seal zone widths. The dynamic optical parameters may also affect the second, cutting beam step as well. The tissue may experience a carbonization phase with increasing temperatures before the ablation phase. Again, these dynamics could not be incorporated into the model, but may translate into a significant increase in the tissue absorption coefficient.

A second limitation concerns the laser beam dimensions during the simulations. It was necessary to model a collimated flat-top beam incident on the tissue surface since this closely matched our benchtop studies. However, in our experimental studies, the laser output beam from the cylindrical lens was focused on the tissue, creating a variable spot width in the z direction of the tissue. The path length of the laser beam within the tissue is only 400 µm due to compression of the vessel to match the insert in the laparoscopic jaws, so the beam width change within the tissue is minimal. The benchtop study also did not achieve a full flat-top profile. This left a small region of lower power density on the beam periphery which, during the cutting beam process, could lead to a larger BSZ. However, despite this uncertainty, a close correlation was still observed between the results of the computer simulations and experimental results, as shown in Figure 6.3.

A third limitation of the simulations is due to the material used in the experimental setup that the blood vessel rests on, called the “backplate”. In particular, with smaller vessels, the backplate material may affect the results. When the laser beam overfills the vessel and is incident on the backplate without first interacting with the blood vessel, the backplate directly absorbs the energy and heats up. The heat from the backplate may then be reabsorbed by the back side of the blood vessel. For simplicity, these simulations assumed no laser beam overflow beyond the vessel width.

Finally, it should be noted that equation 6.2, used to simulate burst pressure strengths, is a simplified version of the actual mechanism which occurs during vessel burst pressures. The geometry used assumes a flat plate which is not a realistic geometry which occurs in a sealed vessel. Future work can improve on the correlation of BSZ and burst pressures by improving the geometry of the seal in the model. The mechanical properties used in this equation are taken from the mechanical properties of healthy vessels. When these vessels are thermally coagulated during laser irradiation, their mechanical properties change. In future work, these mechanical properties should be measured after laser irradiation to provide a more accurate model. The model also uses an average size vessel, however, burst pressures are a function of vessel size. Overall, the model provides a close approximation to experimental burst pressure measurements, but future refinements may continue to improve on the model.

6.6: Conclusion

These simulation studies enabled identification of successful sealing and cutting optical linear beam dimensions based on temperature and tissue damage, optimization of laser parameters including power and irradiation time, and correlation of bifurcated seal zones with expected vessel burst pressures. Low (25 W), medium (100 W), and high-power (200 W), 1470-nm infrared lasers are capable of rapidly sealing and cutting blood vessels with acceptable burst pressures. The low power laser provides a less expensive, more compact, portable, and air-cooled system. The medium and high-power lasers may enable shorter seal and cut treatment times in the operating room and the potential for treatment of larger blood vessels. A trend emerged which linked an optimal bifurcated seal zone with burst pressures. Future work will utilize these laser parameters to design a more efficient infrared laser vessel sealing and cutting device for laparoscopic surgical procedures.

These computer simulation studies demonstrate that low, medium, and high-power 1470-nm lasers are all capable of rapidly sealing and cutting blood vessels with acceptable burst pressures. A trend emerged which linked an optimal seal width with burst pressures. The optimal laser parameters for the shortest procedure time for low power laser parameters were: 24W/5s/2x8mm for sealing and 24W/5s/1x8mm for cutting, yielding thermal spread of 0.4 mm and corresponding to experimental vessel burst pressures of ~380 mmHg. Optimal medium-power laser parameters were: 90W/1s/3x9.5 mm for sealing and 90W/1s/1x9.5 mm for cutting, yielding thermal spread of 0.9 mm for burst pressures of ~1300 mmHg. Optimal high-power laser parameters were: 200W/0.5s/4x9mm for sealing and 200W/0.5s/1x9mm for cutting, yielding thermal spread of 1.3 mm with predicted burst pressures to be ~1300 mmHg. Future chapters will explore the optimized parameters for sealing and cutting into a laparoscopic probe design.

CHAPTER 7: NOVEL LAPAROSCOPIC PROTOTYPE DESIGNS

7.1: Introduction

Previous chapters established the optimal parameters to seal blood vessels using IR laser technology demonstrating this ability in *ex vivo* laboratory setups. Laser based sealing technology has also been proven, in our laboratory, to work *in vivo* utilizing a non-laparoscopic handheld device which is very similar to the benchtop design used in previous chapters [83]. The custom built, optical sealing probe (Figure 7.1), with a plunger style clamping mechanism, successfully performed open procedure blood vessel ligation on a 54 kg farm pig under general anesthesia. It is important to note that this device design (>10 mm outer diameter (OD)) was not a laparoscopic device and is incompatible with standard laparoscopic surgical instruments (Figure 7.1). Since energy-based devices are used in about 80% of the approximately 15 million laparoscopic procedures performed globally each year [2], laser-based technology must be able to linearly beam shape within the laparoscopic probe size to compete in the vessel ligation space. The goal of this chapter is to introduce a series of optical designs for integration into a standard laparoscopic 5-mm-OD with a Maryland jaw configuration similar to current devices shown in Figure 7.1.

Figure 7.1: (Left) Maryland style laparoscopic RF electrosurgical device, including handle, 5-mm-OD arm/shaft, and jaws for grasping vascular tissue bundles. (Right) Open surgical infrared laser vessel sealing device, featuring a plunger style tissue clasping mechanism in a cylindrical head with ½ inch (12.7-mm-OD) components, too large for laparoscopic surgery [82].

The fundamental limitation for a laparoscopic instrument is the size constraints of the jaw configuration and the 5-mm-OD shaft of standard laparoscopic devices. The basic jaw-style design will ideally need to incorporate a multimode optical fiber within the arm, with either divergent or collimated output beam, illuminating a beam shaping chamber with a fixed and parallel orientation to the device arm, as seen in Figure 7.2. Within this chamber, the incident beam needs to be transformed into a linear beam, exiting through a window at a 90^o angle. A top jaw with a pivoting hinge opens and closes allowing a grasping motion to provide compression during sealing and cutting of blood vessels. All beam shaping designs considered emitted from an optical fiber within a beam shaping chamber (in Figure 7.2), and then deliver a linear beam at a 90^o angle to the blood vessel located between the window and top jaw. In order for the design to be the best for our application, it must: create a high-quality linear beam shape, be affordable to manufacture in quantities, minimize custom components, have a high damage threshold, and be both repeatable and reproducible. Assessments of each design are described below in Section 7.2. Designs with the most potential will be explored in depth in later chapters.

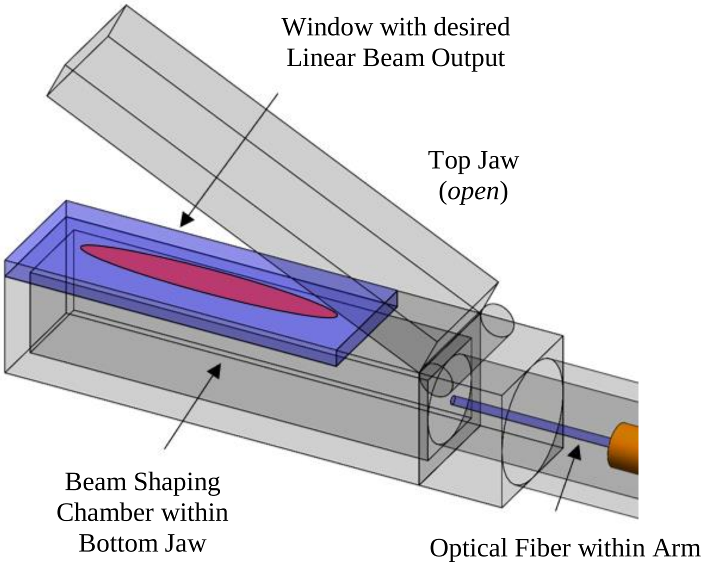

Figure 7.2: Jaw-style laparoscopic clamp design model. Multimode fiber output enters beam shaping chamber and is transformed into a longitudinal linear beam, depicted in red, which exits through the window.

7.2: Potential Beam Shaping Designs

Design #1 (Static Mirror): A simple method for side firing delivery of the laser beam is to use an angled mirror. Utilizing beam divergence from the fiber, the incident light will reflect upward at various angles. To form a linear beam profile, the light is confined to a fixed width using two side mirrors. One limitation of this design is that the power profile along the major axis of the linear beam is heavily weighted at the distal tip, due to the glancing angle off of the single mirror. This is because a portion of the light leaving the fiber is never reflected exiting the window at the tip, and most reflection that does occur is at a glancing angle. However, a simple hinged top jaw should provide less vessel compression in the tip region, possibly offsetting this concern in the sealing process. Simulations for the single mirror were performed, using a reflecting ramp. The linear beam seen in Figure 7.3 would run across the inside of the jaw in the linear direction. The ideal profile for our application is a flattop linear beam profile. However, as it can be seen in Figure 7.3 the profile is not flat due to the diverging light from the fiber and the ramped mirror. To optimize to the flattest profiles, the fiber spacing was set at 0 mm and 0°. However, this limited beam length to ~13 mm and distal tip had an intensity spike approximately 2 times higher than profile, making this not an ideal solution for the laparoscopic device.

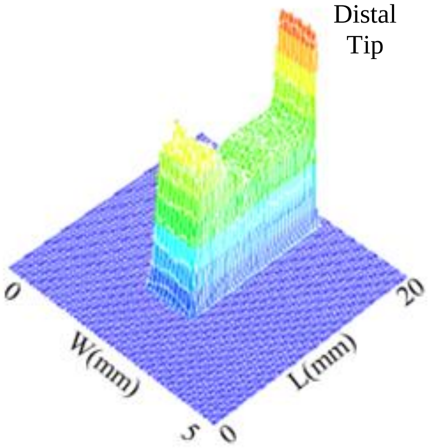

Figure 7.3: FRED simulations of linear beam output. Single mirror parameters: 0.5 mm fiber height, 0 mm fiber spacing, 0° fiber tilt.

Design #2 (Side Firing Fiber Bundle): Multiple side-firing beams of equal intensity could be achieved by coupling single or multiple laser beams into a fiber optic bundle. The fibers would be staggered with increasing lengths at the distal, output end of the fiber optic bundle. Angle polishing the fiber tips to allow for side firing output, along with overlapping outputs of consecutive fibers, would thus, produce a quasi-linear beam profile. One major challenge to this design is efficient coupling of a single high-power laser beam into the proximal end of the fiber optic bundle, without overflow of the laser power causing damage to individual fibers. In general, fiber optic bundles are traditionally used in low power medical applications including for illumination and detection in conventional flexible endoscopes, as well as in spectroscopy. It is unclear whether a fiber optic bundle could handle 100 W from the 1470 nm diode laser source without significant fatigue. Alternatively, utilizing multiple laser sources for each fiber in the bundle may produce a desired outcome and will be explored in later chapters.

Design #3 (Beam Splitters): Another similar approach to turn a single circular laser beam into multiple beams oriented in a linear pattern can be achieved by stacking beam splitters with gradually increasing reflection at 45°. The partially transmitting angled surfaces create multiple side firing beams. To achieve equal intensity of each beam, the first beamsplitter would need to be 1/*n* reflective, with *n* equal to number of beams, and increasing reflectance thereafter, until the final two mirrors, which would be 50% and 100% reflective. The fiber output would preferably be collimated by a small lens for this design. However, fabrication of this gradient reflection beam splitter stack is a significant challenge. For conceptual purposes, a consecutive beamsplitter prototype was built using 5 mm cube beamsplitters and cylindrical lenses, as seen in Figure 7.4. The initial beam splitter was 30% R / 70% T, the second was 50% R / 50% T, and the final element was 45° mirror. Collimated light with approximately 4 mm diameter with cylindrical lenses was used to condense 4 mm wide beams to approximately 1 mm. Cylindrical mirrors may not be necessary if smaller and additional beamsplitters are used. High laser power (~100 W) did not damage optical components, so the concept is feasible with smaller components. It should be noted that smaller components are not available off the shelf and would be expensive to manufacture. Another drawback for this design is the complexity in designing a curved jaw which may be a necessary future feature of an *in vivo* device. Because of the need for many custom components, the high cost, and the unknown damage thresholds of miniature optics, this design was not studied in further detail.

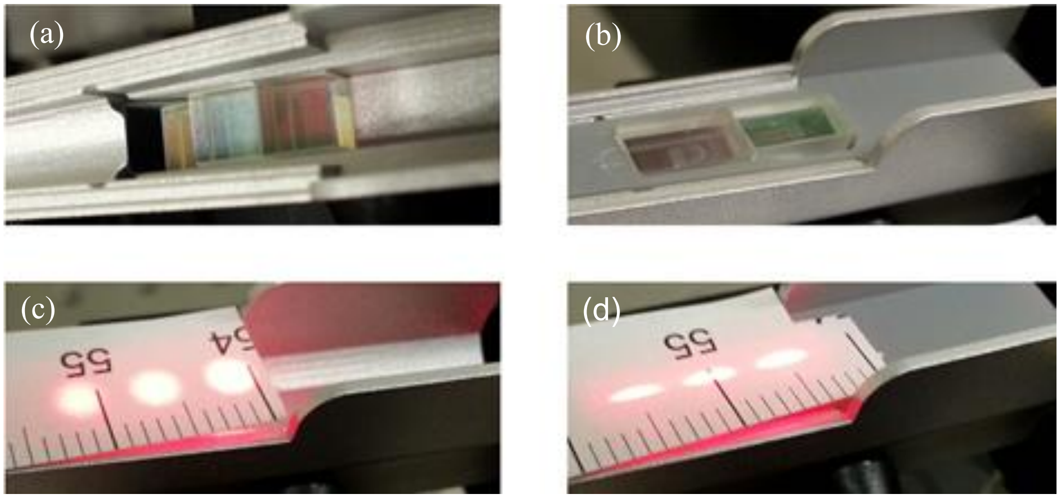

Figure 7.4: (a) Beamsplitters and angle mirror in jaw. (b) Cylindrical lenses used to condense 5 mm beams into ~ 1 mm width linear beam. (c) Beam outputs without cylindrical lenses, and (d) with cylindrical lenses. Ruler increments in mm.

Design #4 (Mirror/Side Firing Fiber Scanning): Another novel approach, entails a mirror which would output a single side firing circular beam, but raster scan in a linear motion. The fiber output would preferably be collimated by a small lens for this design. Previous studies have used continuous wave (CW) laser energy with operation times on the order of seconds. CW light coagulates tissue by thermal effect. While a rastering beam would not be illuminating each vessel region continuously, the vessel's temperature would still increase after consecutive "pulses." Assuming similar fiber power output, the single circular beam would have a higher instantaneous intensity than a long linear beam, but total power averaged over a few seconds, dependent on dwell times, would be similar. Another variation of this concept could be a sliding fiber with side firing output which will be explored in future chapters. This mirror-side firing fiber scanning design provides several advantages, including use of lower laser power, which is less likely to damage the optical components, reflective coatings in the device, and easier integration into curved and longer jaw configurations. The sliding mirror concept was prototyped on a large scale using a 30 mm linear translation reciprocating saw with 45° mirror attached, illuminated with 5 mm collimated 1470 nm laser energy. To test feasibility, a 4.2 mm diameter vessel was successfully sealed using previously reported methods on benchtop compression setup, with a seal time of 10 s and measured burst pressure of 834 mmHg. Dwell time at the ends of the linear beam are longer, but may be compensated for by precisely controlling translation speeds. When tested smaller mirrors (< 2 mm diameter) did fail at higher powers, not having the damage threshold necessary to achieve competitive sealing times. Rather than an oscillating mirror, an oscillating side firing fiber could be used. This fiber would need to be angle polished reflecting the light from the tip at a 90^o angle. The reciprocating side firing fiber will be explored in later chapters.

Design #5 (Diffuse Fiber): An additional design included a longitudinal parabolic mirror which can be placed in the laparoscopic chamber to focus illumination of 360^o, radially diffusing distal fiber optic tip onto the vessel. By placing the fiber above the focal point of the parabola, the light emerging from the fiber away from the tissue will be reflected into focus in the tissue, narrowing the linear beam's intensity profile. Disadvantages of this design are (1) that diffusing fibers have lower laser damage thresholds than standard fibers, and (2) a significant portion of energy exits distal tip instead of radially. With the limitation of using low laser energy, we would compromise the speed of the device and not be competitive with existing technologies. In preliminary benchtop studies we were also not able to achieve a consistent and repeatable etched fiber, and could not reliably produce a fiber with a high enough damage threshold. Due to these reasons this design was not pursued further.

Design #6: (Cylindrical Mirror) Experiments and simulations demonstrated that a collimated light beam striking a cylindrical mirror off center produces a side firing linear beam. The rapidly changing angle of reflection across the beam's spatial profile diverges the beam across one axis. To achieve a flattop beam across the longitudinal direction, an ellipse or parabolic mirror could be used. However, to achieve longer linear beams the cylindrical mirror would have to be placed further from the window, increasing the dimensions of the small laparoscopic jaw, or the radius of curvature of the mirror would have to be decreased smaller than the beam width. The single cylindrical mirror case, was ray traced to demonstrate capability to create a linear side firing beam, as seen in Figure 7.5. However, to create a linear beam of sufficient length the size of the jaw would be too large. Therefore, further testing was not performed on this design.

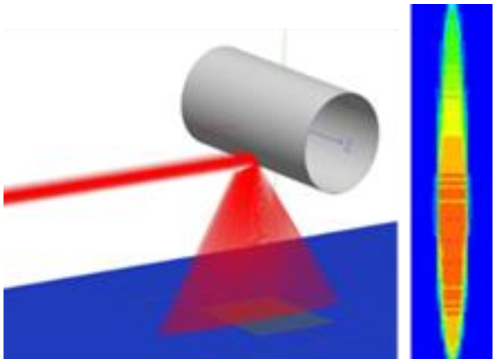

Figure 7.5: FRED simulation of single cylindrical mirror.

Design #7 (Cylindrical Staircase): To address the limitations of Design 6, a cylindrical mirror “staircase” design was tested. With this design, it is possible for the radius of curvatures to be small, achieving greater divergence angles, and the bottom halves of the mirrors can be blocked by the top of another consecutive mirror. Advantages of this design include: no moving parts; the use of only reflective elements, allowing for higher damage thresholds; and design flexibility regarding cylindrical mirror size and number and side mirror width to achieve desired linear beam profile. Simulations for the cylindrical staircase added the additional parameter of cylinder diameter. For this study, only three-cylinder diameters were tested and in each case all diameters were equal and coincident with no overlap. Multiple cases showed promising linear beam profiles over the entire 20 mm length, with one selected case as seen in Figure 7.6. Unlike the single mirror, the cylindrical staircase showed highest regions of intensity closer to the fiber tip or in the middle of the profile. This is viable as clinically most vessels would be clamped in this region of the jaw, similar to clamping with scissors. The cylindrical staircase design was pursued for further study but was ultimately found to have a non-consistent beam shape, no way of dynamically changing its beam shape for cutting, and extremely costly time-consuming manufacturing process [84].

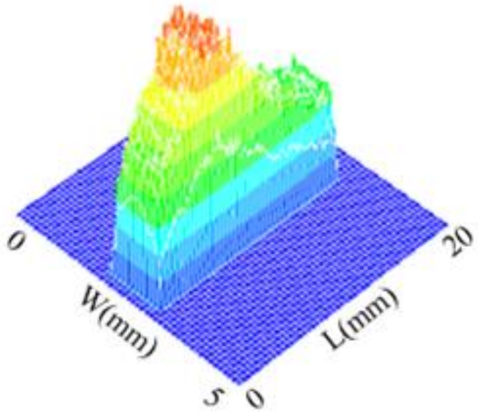

Figure 7.6: Cylindrical staircase parameters: 0.5 mm diameter cylinders, 1.5 mm fiber height, 2.5 mm fiber spacing, 0° fiber angle.

7.3: Conclusion

Several optical beam shaping geometries for transforming a circular laser beam into a linear beam shape within a standard Maryland jaw and 5-mm-OD shaft of a laparoscopic vessel sealing device were evaluated for potential success. Table 7.1 summarizes advantages and disadvantages of each design. The reciprocating side firing fiber and the fiber bundle were indicated to have the most potential and will be explored further in the next chapter.

Table 7.1: Comparison of optical beam shaping designs.

	Low Cost	**High Damage Threshold**	**Repeatable**	**Minimal Custom Components**	**Linear Beam Quality**	**Study Further**
Flat Mirror	Yes	Yes	Yes	Yes	No	No
Fiber Bundle	Yes	Yes	Yes	Yes	Yes	Yes
Beamsplitters	No	NA	Yes	Yes	Yes	No
Reciprocating side firing fiber	Yes	Yes	Yes	Yes	Yes	Yes
Diffusing fiber	Yes	No	No	Yes	NA	No
Cylindrical Mirror	Yes	Yes	Yes	Yes	No	No
Cylindrical Staircase	No	Yes	No	No	No	No

NA=Not Available

Chapter 8: Novel Fiber Optic Linear Beam Shaping Designs for Laparoscopic Laser Sealing of Vascular Tissues

8.1: Introduction

The fundamental limitation in a laparoscopic device is the size constraints of the Maryland style jaw and the 5-mm-OD shaft of standard laparoscopic devices. As discussed in Chapter 7, the bottom jaw design will need to both reflect the beam at a 90^o angle and create a uniform linear beam profile, all within the limited space of a standard jaw. The top jaw, with a pivoting hinge, serves to open and close for grasping vessels and provides tissue compression during sealing. Chapter 7 narrowed the potential laparoscopic designs based on cost, damage threshold, repeatability, beam quality, and minimizing external vendor custom components. All of the designs we will pursue in this chapter are optical fiber delivery designs. An optical fiber delivery method is best for our particular application because it is relatively compact, low cost, and has a high damage threshold. In particular, this chapter explores three novel optical fiber designs that can produce a linear beam profile and be integrated into a standard 5-mm-OD laparoscopic device.

8.2: Designs and Simulations

8.2.1: Fiber Optic Beam Shaping Designs

Three fiber optic-based beam shaping designs were considered to deliver a linear beam perpendicular to the blood vessel length, with the vessel sample located between the window and top jaw. Brief assessments of each design are provided below.

Design #1 (Reciprocating Side-Firing Fiber): A multimode fiber was angle polished to create a side-firing fiber. The fiber was constrained to one degree of freedom and reciprocated back and forth, transforming a circular spot to a linear spot through its linear motion. Utilizing beam divergence from the side-firing fiber, incident light reflects upward as the fiber is scanned along the vessel width. Beam width is fixed while beam length can be changed by programming the translation length. When the distal end of a fiber is cleaved and polished at the optimal angle, it is possible for the light to be reflected in the orthogonal direction. There will also be losses in the form of refracted light due to small allowable tolerances in angle and glass impurities.

For our application, two criteria must be met for the side-firing fiber. The first criteria is the total internal reflection (TIR) must occur for all incident rays [85-86]. Since the fiber is much larger than the wavelength, geometrical optics can be used to approximate the optimal angle of the fiber tip to achieve TIR of all incident rays. To maximize reflection of light from the fiber, the optimal polishing angle is calculated using the following Fresnel equations:

$$R = \frac{R_s + R_p}{2} \qquad 8.1$$

where, R_s and R_p are perpendicular and parallel polarization, respectively, and are given in terms of index of refraction of the core (n_1), index of refraction of air (n_2), the angle the indecent ray makes with the tip boundary normal (ρ_i), and the angle of transmitted light exiting the fiber (ρ_t):

$$R_s = \left|\frac{n_1 \cos \rho_i - n_2 \cos \rho_t}{n_1 \cos \rho_i + n_2 \cos \rho_t}\right|^2 \tag{8.2}$$

$$R_p = \left|\frac{n_1 \cos \rho_t - n_2 \cos \rho_i}{n_1 \cos \rho_t + n_2 \cos \rho_i}\right|^2 \tag{8.3}$$

The second optimal parameter is governed by the chief ray propagating out of the fiber as close to an orthoginal position as possible (Figure 8.1). Both of these criteria depend on the numerical aperture (NA) of the fiber and the polish angle. Since the fibers used for this experiment have an NA with a standard deviation (S.D.) of ± 0.02, the optimal polish angle was calculated to be between 38-41° (Figure 8.1).

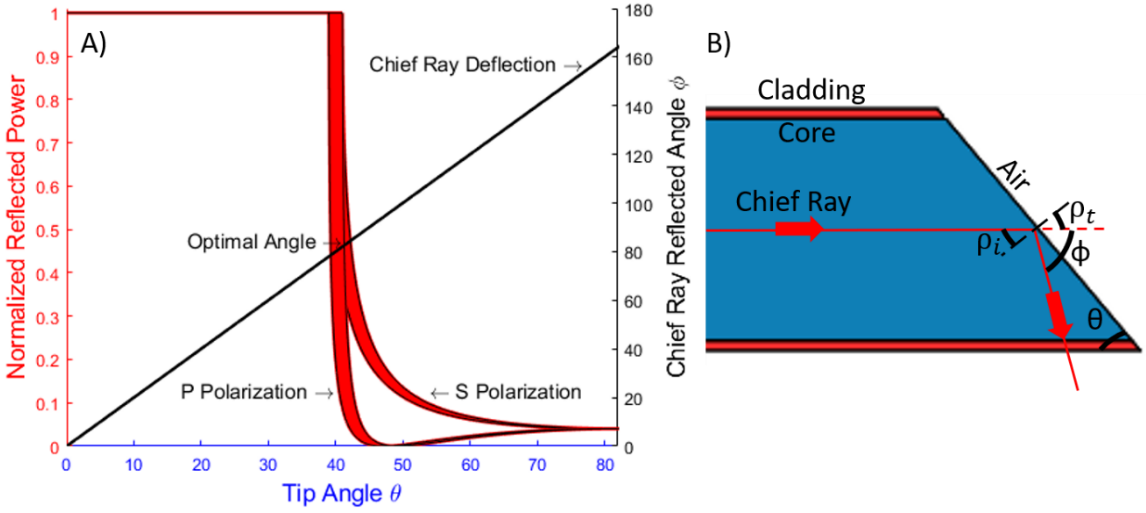

Figure 8.1: (A) The normalized optical power of reflected light from the side firing fiber for both the S and P polarization states as a function of tip angle. The width of these lines is the percent error given by the standard deviation in the numerical aperture of the fibers used in this study. The black line represents the angle at which the chief ray will propagate out of the fiber as a function of tip angle. (B) Conceptual representation of the geometrical ray tracing for a side-firing fiber with incident (ρ_i), polished tip (θ), and deflection angles (Φ), labeled.

Design #2 (Side-Firing Fiber Bundle): This design uses a similar side-firing fiber concept as Design #1, but without linear translation. Instead, beam-splitters divided the laser energy into three equal increments. The light was then coupled into three separate side-firing fibers. These fibers were stacked and staggered by a 1 mm differential in the z-direction, with increasing lengths at the distal end of the fiber bundle. The 1 mm differential of the side-firing fiber tips enables overlapping outputs of consecutive fibers and produces a quasi-linear beam profile. Beam length is held fixed, which is dictated by the number of fibers in the bundle. However, beam width along the axis changes for each stacked fiber due to divergence of light from the fiber (Figure 8.2).

Design #3 (Forward-Firing Fiber Bundle): Similar to Design #2, an external beam-splitter was used to couple laser power equally into three fibers. However, these distal fiber tips are polished flat, providing normal axial transmission. The fibers are also stacked and staggered so they are 2.2 mm from the tilted glass slide. The traditional jaw will have to be re-designed into a sloped configuration to accommodate this bundle geometry in a laparoscopic jaw (Figure 8.2).

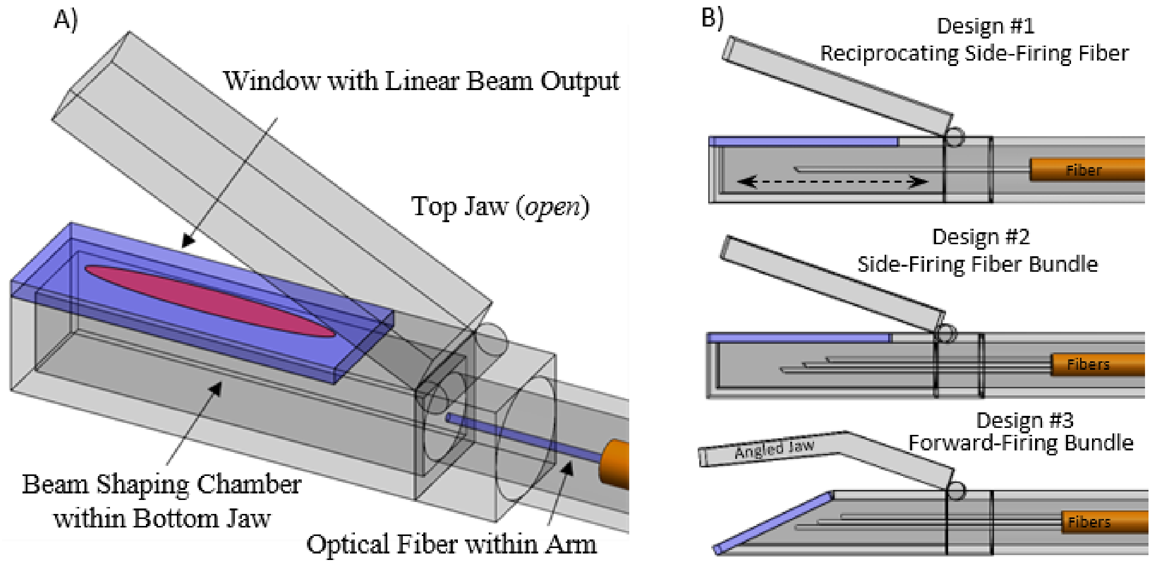

Figure 8.2: (A) Jaw-style laparoscopic clamp design model. Multimode fiber output enters beam shaping chamber and is transformed into a longitudinal linear beam (red), which exits through the window. (B) Conceptual designs considered for beam shaping in a laparoscopic device. The concept art shown is not intended to be to scale.

8.2.2: Computer Simulations

Simulations were performed using models created in a computer aided design (CAD) program (Solidworks, Dassault Systemes, France) and then analyzed using optical software (FRED, Photon Engineering, Tucson, AZ). Optimization of spacing between individual fibers in the fiber bundles was simulated and then used in the benchtop designs. For fiber bundles, the independent beam profiles needed to be sufficiently long to span the entire width of a blood vessel, and sufficiently overlap to create a uniform beam profile across the entire vessel (to produce a strong full width seal). The reciprocating fiber was modeled to include hysteresis for the directional change in oscillation. Simulations and benchtop profiles were then compared. Due to the rapid divergence of the beam profiles, the most effective way to characterize benchtop profiles was through image of carbon “burn” paper using MATLAB (MathWorks, Portola Valley, CA) (Figure 8.3).

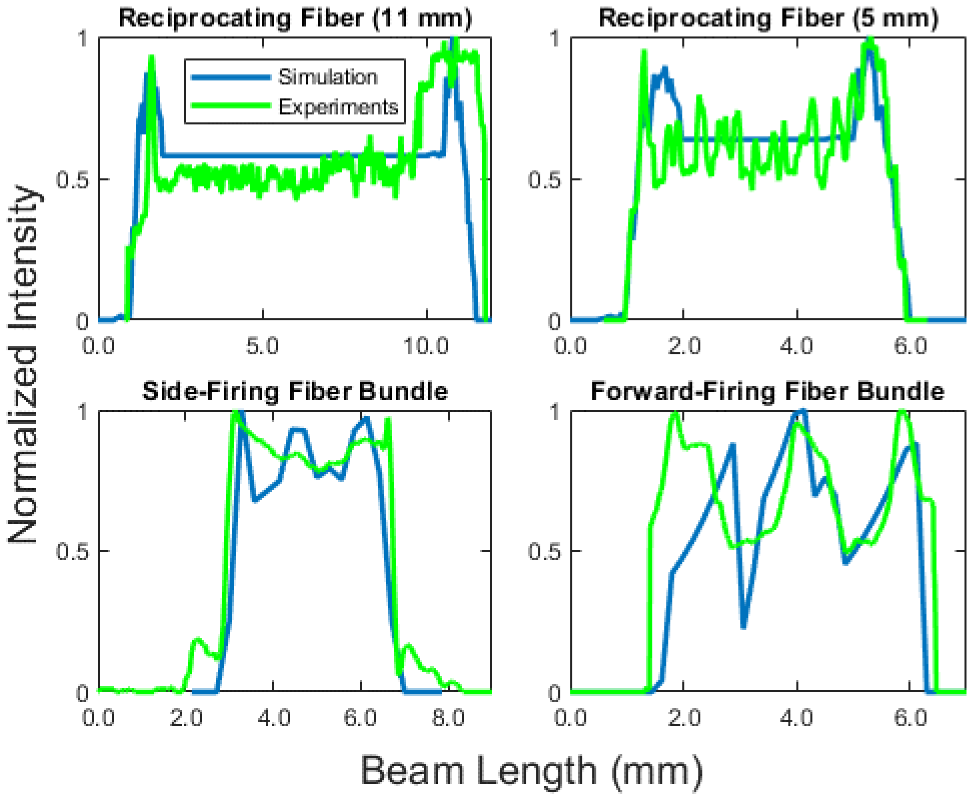

Figure 8.3: Simulation (blue lines) of spatial beam profile and experimental results (green lines) for spatial beam output in the linear direction.

8.3: Methods

Fresh porcine kidney pairs were obtained (Spear Products, Coopersburg, PA) and renal arteries were dissected, cleaned of fat, and stored in physiological saline prior to same day use as described in detail in Chapter 2. A total of 41 blood vessels were harvested, with a mean OD of 2.8 ± 0.9 mm.

A 110-Watt diode laser (BrightLase Ultra-500, QPC Lasers, Sylmar, CA) with wavelength of 1470 nm was used. Blood vessel samples were compressed to a fixed thickness of 0.4 mm, closely matching the OPD, for more uniform delivery of light energy to tissue. The laser was operated in continuous-wave (CW) mode for short durations of 1-5 s, and at output powers of 30-60 W. Laser power output was measured after the beam shaping optics using a power meter (EPM1000, Coherent, Santa Clara, CA) and detector (PM-150, Coherent). The laser exposure duration and power were chosen based on the beam shape to keep the fluence (total energy density) below 900 J/cm^2, which was previously identified as optimal for successful sealing of blood vessels in Chapter 6.

8.3.1: Fiber Angle Polishing

Multimode, 550-µm-core optical fibers (FG550LEC-CUSTOM, Thorlabs, Newton, NJ) with NA of 0.22 ± 0.02 and high-power proximal SMA905 connectors, were used in this study. The bare distal fiber tip was prepared by manually stripping, cleaving, cleaning, and flat polishing to a 16-µm grit (PF16.0A-P-4, Krelltech, Neptune City, NJ). The fiber was then mounted in a bare fiber polisher (Radian^{TM}, Krelltech) using a 600 µm side polishing ferrule. The polisher was then rotated to achieve a 40^o angle, accurate to 0.5^o of repeatability (Figure 8.4). An initial two stage aluminum oxide polish of 16-µm and 0.3-µm (PF16.0A-P-4, PF00.3A-P, Krelltech) grit were used to align and angle the fiber. The final polishing stage used a diamond 0.1-µm grit

(PF0.1D-P-4, Krelltech) to achieve a smooth mirror-like surface. The side-firing fiber tip was then inspected under magnification. During preliminary damage threshold studies, a single distal angled fiber tip transmitted laser power > 80 W at 1470 nm for 5 s, without evidence of fiber tip degradation. Due to the standard deviation in the fiber NA and the half angle accuracy of the side angle polish, a value of 90% reflection of power was considered acceptable for QC (Figure 8.4).

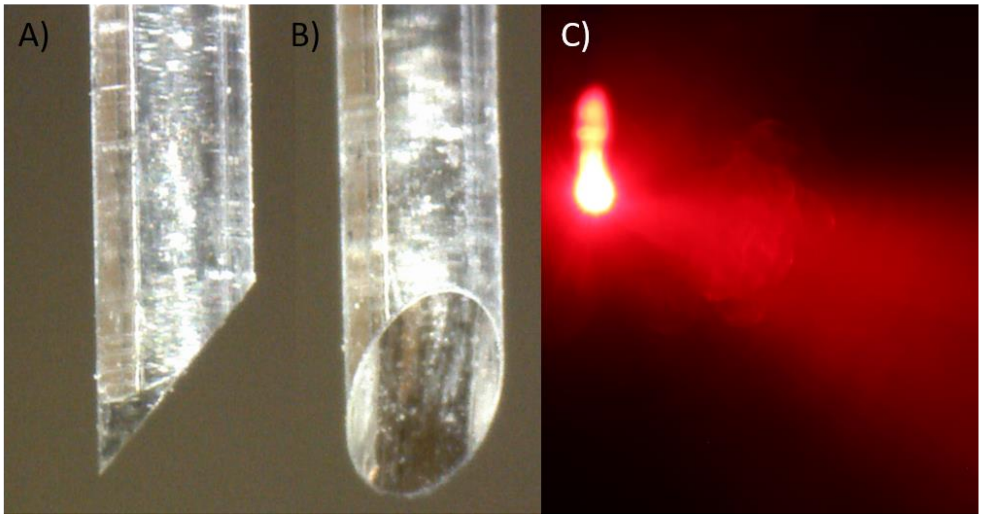

Figure 8.4: (A) Magnified image of a 40° angle side polished fiber tip; (B) Polished surface to 0.1 µm grit; (C) Photograph of visible red aiming beam, showing 90% reflection of light from the side-firing fiber with a 1 s prolonged shutter time in a water misted environment.

8.3.2: Benchtop Experimental Setup

Design #1: This setup was designed to mimic the tissue contact aspects of a laparoscopic instrument. Infrared laser radiation delivered through an armored, 400-µm-core, low-hydroxyl (OH), silica optical fiber patchcord (QPC Lasers) connected to a high-power fiber optic shutter system (SH-200-55-1470-M-0-T-BH-SP, OZ Optics, Ottawa, Canada). Laser energy was then delivered through a 550-µm-core fiber (FG550LECCustom, Thorlabs) with high power proximal SMA connector, from the optical shutter output port to the benchtop compression system. The side-firing fiber was attached to a servo motor using a custom 3D printed mount. The fiber was also inserted through a guide rail to ensure all but the linear degree of freedom was locked. The fiber was then positioned under a glass slide. Above the glass slide, a compression precision milled backplate was mounted, which incorporated a 0.4 mm gap stop and a 3 mm thick glass slide insert. The gap between tissue contact surfaces when fully closed was fixed at 0.4 mm in the setup to provide tissue compression closely matching the OPD. Blood vessels were sandwiched between the backplate and glass slide, similar to previous chapters. The fiber was then reciprocated by the servo motor for 5 s. The servo motor was programmed with a two length 11 mm stroke for larger blood vessels (> 2.6 mm) and a 5 mm stroke length for smaller blood vessels (< 2.6 mm). Figure 8.5 shows an image with a prolonged shutter exposure time of the reciprocating side-firing fiber producing a linear beam profile. This linear beam was aligned perpendicular to the vessel length, and measured either 11 mm long by 2.0 mm wide (fluence of 636 J/cm^2) or 5 mm long by 2.0 mm wide (716 J/cm^2). Large vessel laser seals were performed at a duty cycle of 0.1 and irradiated at 40 W for 5 s, and small vessel laser seals were performed at a duty cycle of 0.25 and irradiated at 30 W for 3 s.

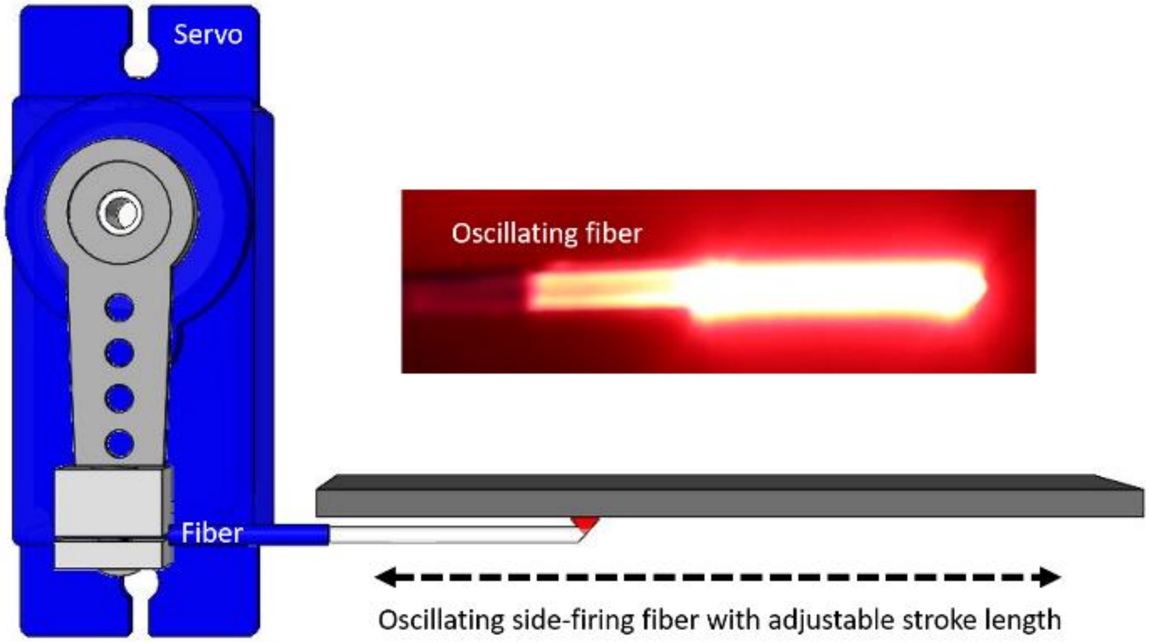

Figure 8.5: Tabletop setup for testing a reciprocating side-firing fiber and its laser beam profile captured with a prolonged shutter exposure of 3 s. *(Image not drawn to scale)*

Design #2: This setup was designed to incorporate three fibers in an orientation capable of delivering sufficient laser energy for sealing blood vessels within the constraints of a standard Maryland style laparoscopic jaw configuration. First, near-IR laser radiation was delivered to an armored, 400-µm-core, low-hydroxyl (OH), silica optical fiber patchcord (QPC Lasers). The laser energy was then collimated into 25.4-mm standard optics, and divided almost equally (30/35/35 split) before delivery through three separate, side-firing, 550-µm-core-diameter fibers (FG550LECCustom, Thorlabs) (Figure 8.6). To achieve a linear beam profile, the fibers were staggered 1 mm in Z axis and a 90^{o} orientation (Figure 8.6). All three fibers were attached to two 3D printed custom mounts to achieve these specific mounting parameters. The first mount locked angular degrees of freedom, and the second mount locked Z axis distance. After alignment, the fibers were positioned under a 1 mm thick glass slide. Above the glass slide, a compression precision milled backplate was mounted, which incorporated a 0.4 mm gap stop and a 3 mm thick glass slide insert. The gap between the tissue contact surfaces when fully closed was fixed at 0.4 mm in the setup. The vessel sample was sandwiched between the backplate and glass slide. This linear beam was aligned perpendicular to the vessel direction, and measured 4 mm long by and 2.0 mm wide (fluence of 750 J/cm^2). Beam width varied with length since the fibers were stacked on top of one another and the beam was diverging out of the fibers. Laser seals were performed on arteries of 1-2 mm diameter (n = 10) irradiated at 30 W for 2 s.

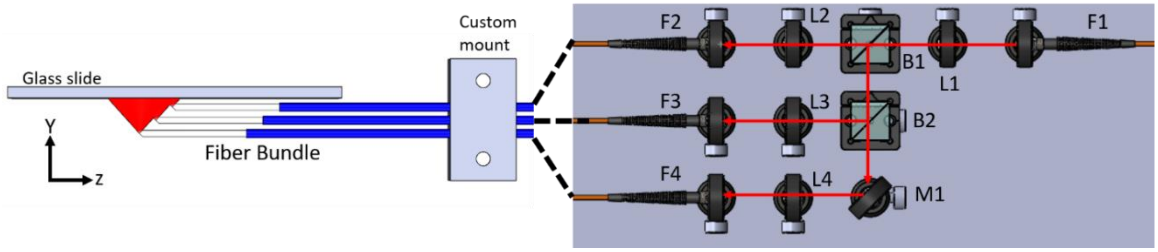

Figure 8.6: Benchtop setup for side-firing fiber bundle design. (Left) Design of stacked side-firing fibers making a linear beam profile (second custom mount is not pictured). (Right) Diagram showing laser energy entering system via a MM fiber (F1), external beam-splitters (B1, B2) and mirror (M1) for splitting light, and lenses (L2-4) needed to couple light into three fibers (F2-4).

Design 3: This setup utilized a novel sloped jaw design to enable use of a forward-firing fiber bundle and permit surgeons to grasp blood vessels more easily. This sloped jaw design incorporated three forward-firing fibers in an orientation which both meets the space constraints and delivers laser energy to blood vessels. The setup was similar to Design #2, except for the orientation and placement of the forward-firing fibers (Figure 8.7). This linear beam was aligned perpendicular to the vessel direction, and measured 5 mm long by 1.5 mm wide (fluence of 800 J/cm^2). Laser seals were performed on arteries of 1-2 mm diameter (n = 11) at 60 W for 1 s.

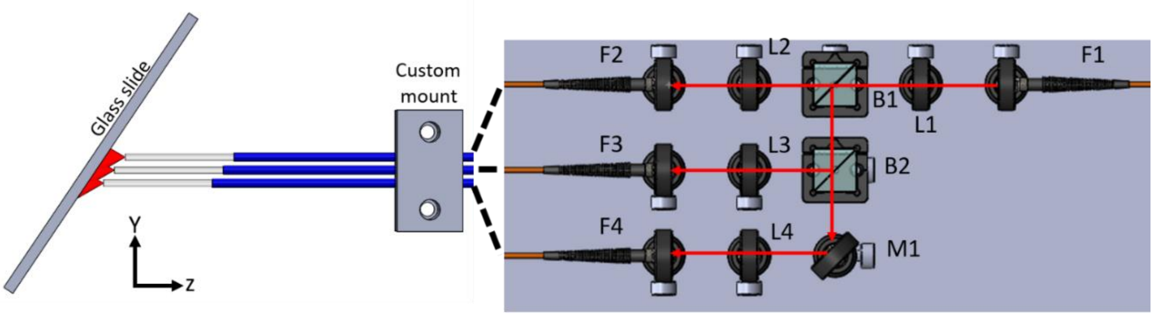

Figure 8.7: Benchtop set for the forward-firing fiber bundle design. (Left) Design of forward-firing fibers and a tilted jaw at 40° (not to scale) making a linear beam profile. (Right) Diagram shows external beam-splitters, mirrors, and lenses, needed to couple light into three fibers.

Vessel burst pressure measurements were performed, as discussed in Chapter 2, and used as the indicator of success for this study. The burst pressure setup consisted of a pressure meter (Model 717 100 G, Fluke, Everett, WA), infusion pump (78- 01000C, Cole Parmer, Vernon Hills, IL), and an iris clamp. The vessel lumen was clamped over a cannula attached to the infusion pump. Deionized water was flowed at a rate of 100 ml/h and maximum pressure (mmHg) was recorded. A successful seal exceeded physiological values for both normal systolic blood pressure (120 mmHg) and hypertensive blood pressure (180 mmHg). A two-tailed t-test was used in comparing burst pressures between modalities with similar vessel widths, with values of $p < 0.05$ considered to be statistically significant, as noted by an asterisk in the tabulated data sets (Table 8.1).

8.4: Results

Burst pressure data for each design is summarized for the three fiber designs (reciprocating side-firing fiber, side-firing fiber bundle, and forward-firing fiber bundle) in Table 8.1. All burst pressures measured were above both normal systolic blood pressure (120 mmHg) and malignant hypertension blood pressure (180 mmHg) (Figure 8.8). Mean burst pressure for Designs 1, 2 and 3 was 475 mmHg for a total of 41 seal samples, with no failed burst pressures (< 180 mmHg).

Table 8.1: Summary of laser parameter and vessel specification and vessel burst pressure results.

Method	**Vessel Size (mm)**	**Burst Pressure (mmHg)**	**Beam Size (mm)**	**Fluence (J/cm^2)**	**Sample size (n)**
Design #1: Reciprocating side-firing fiber	3.7 ± 0.9	524 ± 132	11 x 2	636	10
	1.8 ± 0.3	554 ± 142*×	5 x 2	716	10
Design #2: Side-firing fiber bundle	1.8 ± 0.2	429 ± 99	4 x 2	750	10
Design #3: Forward-firing fiber bundle	1.8 ± 0.4	390 ± 140	5 x 1.5	800	11

* Denotes statistically significant difference ($p < 0.05$) for burst pressures compared to Design #2.
× Denotes statistically significant difference ($p < 0.05$) for burst pressures compared to Design #3.

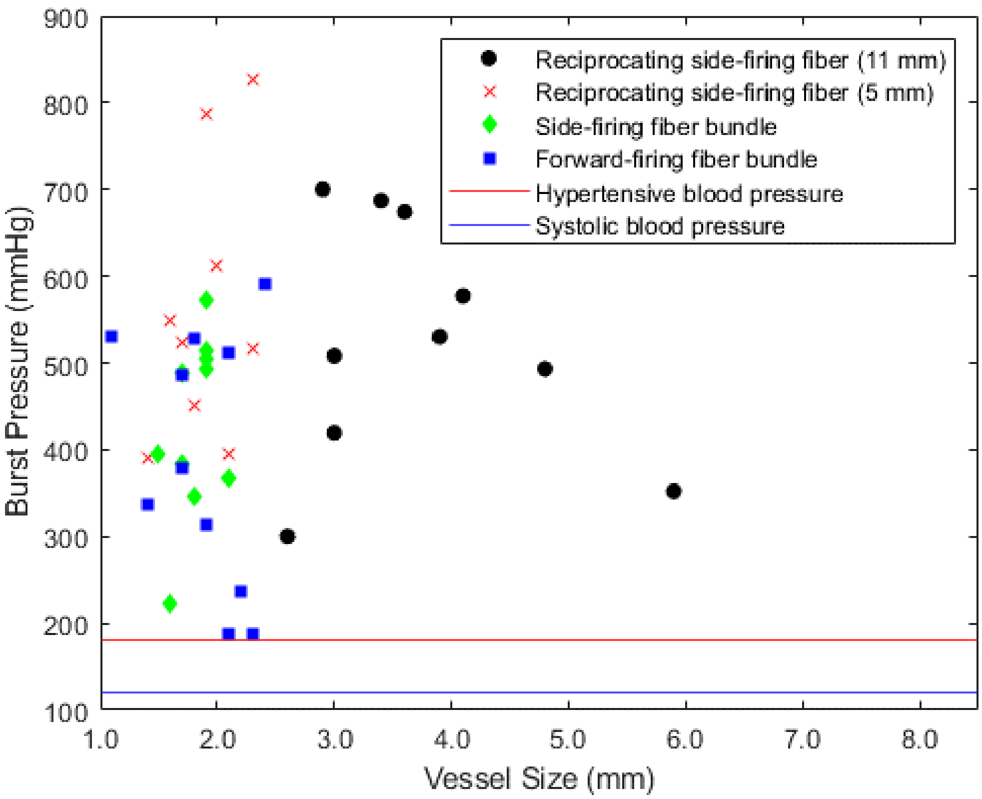

Figure 8.8: Blood vessel burst pressure plotted as a function of vessel size. Normal systolic blood pressure of 120 mmHg (blue line) and hypertensive blood pressure of 180 mmHg (red line) are labeled for reference. All vessel seals tested (n = 41) produced burst pressures above the hypertensive blood pressure threshold.

Fluences (total energy density incident on tissue surface) ranged from 600-800 J/cm^2, and were selected based on previous computer simulations and experimental results [87]. This range of fluences consistently provides strong vessel seals, while higher fluences, from approximately 950-1500 J/cm^2, can potentially be used for cutting and bisection of vessels [87].

All three fiber designs consistently sealed small-to-medium blood vessels (mean diameter of 1.8 mm), as shown in the three data groups in Table 8.1. It should be noted that vessel diameter is listed prior to compression. Typically, compressed vessels have a width up to 50% greater than that of uncompressed vessels [88]. Compression widths have been previously confirmed in Chapter 2 with average percent increases of vessel widths of 47 ± 28%. Therefore, linear beam profiles of 4-5 mm length were chosen for the three fiber designs, to ensure that the entire vessel width was treated by the linear beam profile, and to provide complete seals.

Figure 8.9 shows representative images of blood vessels sealed using all methods, demonstrating that a full width seal was achieved. The blanched or whitened region represents the seal zone. During a surgical application, such a seal would then be cut in half or bifurcated, such that the remaining seal region on each vessel half, referred to as the bifurcated seal zone, is also half as thick.

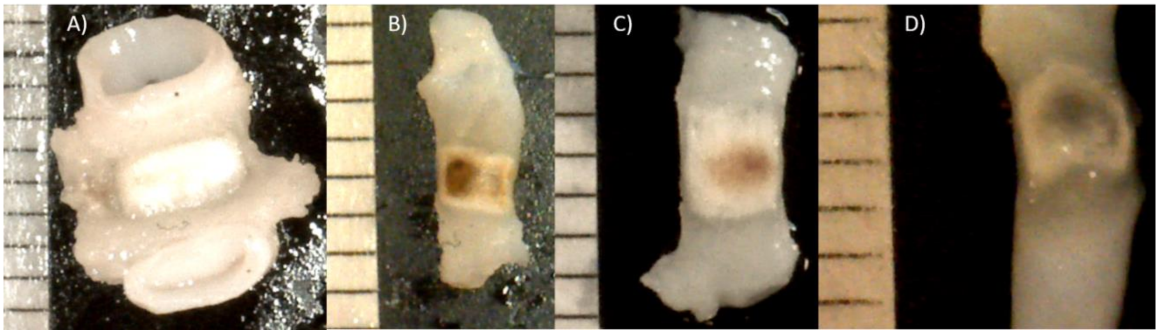

Figure 8.9: Representative images of sealed porcine blood vessels from all three designs. (A) Sealed porcine blood vessel (5 mm diameter) after laser irradiation from Design #1 at 11 mm stroke length. (B) Sealed porcine blood vessel (2.0 mm diameter) after laser irradiation from Design #1 at 5 mm stroke length. (C) Sealed porcine blood vessel (2.2 mm diameter) after laser irradiation from Design #2 and (D) Sealed porcine blood vessel (2.0 mm diameter) after laser irradiation from Design #3.

To demonstrate the versatility of the reciprocating fiber and its ability to seal a wide range of blood vessels, typically encountered during surgery, a fourth data group with medium-to-large vessels (mean diameter of 3.7 mm), was also sealed. The reciprocating fiber was programmed for a longer scan length (11 mm vs. 5 mm), and demonstrated successful seals well above both systolic and hypertensive blood pressure values for all vessels treated (Table 8.1 and Figure 8.8).

8.5: Discussion

Previous preliminary laboratory studies demonstrated that near-IR lasers have several potential advantages compared to conventional electrosurgical and ultrasonic energy-based devices for laparoscopic sealing of blood vessels. These advantages include more rapid sealing and cutting of vascular tissues, more directed deposition of energy into tissue with less collateral thermal spread, stronger vessel seals, the potential for an integrated device capable of optical sealing and cutting without a separate, deployable, mechanical blade to bisect tissue seals, and lower jaw temperatures.

The main objective of this study was to explore novel methods for optical beam shaping utilizing fiber optics, under the existing constraints of a standard Maryland style laparoscopic jaw design. Three optical beam shaping geometries for transforming a circular laser beam into a linear beam shape within a 5-mm-OD shaft of a laparoscopic vessel sealing device were studied. The advantages and disadvantages of each design are summarized in Table 8.2. A reciprocating side-firing fiber (Design #1) was the most promising design, since it provided a continuous, uniform linear beam profile with a versatile, programmable beam length (for treating a wide range of blood vessel diameters), all in a relatively low-cost design. Design #1 was also superior to the other designs because it achieved higher burst pressures. The burst pressure from Design #1 (5 mm reciprocating fiber) was statistically significant ($p < 0.05$) compared to Designs #2 and #3.

Table 8.2: Comparison of advantages and disadvantages for each fiber delivery system.

Designs	Advantages	Disadvantages
Design #1: Reciprocating side-firing fiber	• Low cost • Uniform beam profile and scan length • No constraint on beam length in Y axis	• Complexity of moving parts • Hysteresis effects • Delicate angled fiber tip
Design #2: Side-firing fiber bundle	• Optical components outside device • Higher laser damage thresholds	• Cost of optical components • Delicate angled fiber tip • Poor linear beam quality in X axis and constraint on Y axis length • Fibers sensitive to position and rotation
Design #3: Forward-firing fiber bundle	• Optical components outside device • Robust flat distal fiber tip • Higher laser damage thresholds	• Cost of optical components • Constraint to Y axis length • Not compatible with Maryland jaw • Fibers sensitive to position

However, challenges include consistent polishing to the correct angle, motion artifacts associated with the translating fiber (Figure 8.3) and integration of the servo motor (Figure 8.5) into the handle of the laparoscopic device. The polishing system used in this study consisted of a ferrule fiber holder which was 50 µm larger than the OD of the fiber. This contributed to a small amount of slack and wobble in the fiber during polishing and caused small inconstancies in fiber tip angle, which resulted in a 90% side-firing output. To mitigate motion artifacts, improvements will be made to the servo in the reciprocating side-firing fiber by more efficiently changing circular motion to linear motion with the help of precision gears and more robust guide rails.

Designs #2 and #3 had major limitations associated with the aspect ratio for the spatial beam profiles, with the beam length limited to treatment of small blood vessels only. It is possible for Designs #2 and #3 to be modified for treatment of medium and large blood vessels, simply by increasing the number of individual fibers in the bundle and/or decreasing the diameter of the individual fibers. Such modifications would require more optical components, in turn increasing size, complexity, and cost of the setup. It should be noted, however, that the entire optical setup may potentially be enclosed in a box connected to the laser system and external to the disposable laparoscopic device, thus, representing a one-time capital cost to the entire optical sealing system.

Perhaps the most significant challenge for Design #2 would be design of custom mounts to keep position and orientation of each individual fiber fixed to preserve the overall spatial beam profile, under the rigorous conditions of manual use by the surgeons in a hospital-based setting. For Design #3, incorporating forward-firing fibers, there are no concerns about rotational misalignment of individual fibers, which is an advantage compared to Design #2. However, for Design #3, which incorporates a custom sloped jaw design instead of the standard Maryland style jaw design, an additional concern is whether surgeons would readily adopt the new jaw design for accessing tissues in closely confined anatomical areas.

Overall, there were several limitations of this study. Previous benchtop laboratory studies demonstrated both sealing and cutting of vessels by dynamically changing fluence at the tissue surface in a two-step process. This study focused on developing novel fiber delivery systems for consistently sealing vessels. Future work will involve incorporating cutting and bisection of vessels after a successful seal has been created. This cutting ability may be achieved by integrating a simple mechanism for pushing the fiber optic tip closer to the vessel within the device jaw, so that the energy density is sufficiently increased to provide consistent bisection of sealed vessels.

The benchtop setups used in this study were capable of simulating tissue contact parameters of a surgical device. Future work will need to focus on design, construction, and characterization of a prototype, handheld probe to be used during in vivo animal surgical studies.

Only bottom jaw designs were considered in this study. New designs for the top jaw will be further explored in the future for potential integration of a real-time, closed-loop, optical feedback system to deactivate the laser immediately once a strong vessel seal has been achieved.

8.6: Conclusion

Three novel fiber optic beam shaping geometries for transforming a circular laser beam into a linear beam profile, within the space limitations of a standard 5-mm-OD shaft of a laparoscopic vessel sealing device, were studied. The reciprocating side-firing fiber design is the most promising approach for clinical applications, based on its inexpensive design, uniform linear beam profile, and custom programmable scan length. This design also allows for a customizable beam width which can be varied by the distance the tissue is to the fiber. Having this ability will allow for future work with a two-step sealing and cutting device similar to that described in Chapter 5. Now that we have established a reliable therapeutic delivery system for integration into a laparoscopic device, the next chapter will focus on the real-time diagnostic feedback system for seal strength analysis during procedures.

CHAPTER 9: NON-REAL-TIME OPTICAL MEASUREMENTS FOR CONFIRMATION OF VASCULAR SEAL STRUCTURE

9.1: Introduction

Some RF and US laparoscopic devices incorporate electrical impedance and/or temperature sensors as real-time, closed-loop, feedback to indicate successful vessel seal endpoints during surgery. Our proposed infrared sealing device will also need to incorporate a real-time feedback system for indicating successful vessel seals. In this chapter, a benchtop proof of concept study will utilize optical techniques, such as optical coherence tomography (OCT) and optical signal transmission, to identify potential markers in blood vessels which signify tissue thermal denaturization endpoints for a successful seal. These techniques will be correlated with traditional burst pressure measurements for seal strength verification.

9.2: Optical Coherence Tomography (OCT)

Recently, Doppler OCT was used for experimental evaluation of blood flow and hemostasis after vessel seals [89]. OCT has previously been shown to successfully differentiate between native and coagulated blood vessels [90]. This study examines if OCT A-scans can repeatedly identify the difference between native and coagulated tissue through unique identification markers. Since optical properties of tissues change upon thermal coagulation, with the reduced scattering coefficient increasing by over 50% (10.2 cm^{-1} to 15.5 cm^{-1}) [61,62] which lowers the optical penetration depth, post processing of A-scans will look for identification markers of higher scattering in coagulated regions. Several properties of OCT make it promising for use with vessel sealing instruments. The OCT system is compact and inexpensive and uses a small, disposable, single-mode fiber for potential incorporation within 5-mm-diameter laparoscopic devices. OCT also provides high-resolution, micrometer scale resolution. The near-IR wavelengths used in OCT provide image depths in opaque tissues (e.g. blood vessels) up to a few millimeters, more than sufficient to image the entire vessel thickness under compression (with no blood in lumen) within the laparoscopic device jaws.

The OCT system (Niris, Imalux, Cleveland, OH) used for this study utilized a handheld 8 Fr (2.67 mm-OD) probe, as shown in Figure 9.1. The fiber-based OCT system operated at a wavelength of 1310 nm, with axial and lateral resolutions of 11 and 25 µm. Images had 1.6 mm and 2.0 mm axial and lateral dimensions. An X-Y-Z linear translation stage (460A-XYZ, Newport, Irvine, CA) was used to align the OCT probe in contact with the sample. 2D OCT images were exported and analyzed in MATLAB code, which incorporated greyscale image processing and an A-scan selection system for using the same depth in all A-scans. The A-scan was then integrated to find the area under the greyscale intensity peaks.

Fresh porcine renal arteries were obtained from a slaughterhouse (Spear Products, Coopersburg, PA). The vascular network of blood vessels in the kidneys were dissected, cleaned of fat, and stored in saline, as described in Chapter 2. Medium-size vessels measuring 2-4 mm diameter were used in the studies. Prior to IR laser irradiation, the blood vessel was compressed to a fixed thickness of 400 µm within the tabletop setup, as seen in Chapter 5, simulating the pressure applied by the jaws of a standard laparoscopic device. Parameters for this study were based on the findings in previous chapters such as: an IR diode laser (Brightlase, QPC Lasers, Sylmar, CA) with wavelength of 1470 nm, incident laser power of 30 W, and laser irradiation time of 5 s was used for vessel sealing. A linear beam profile, measuring 8 x 2 mm was applied perpendicular to the vessel length, to provide a uniform and full width seal.

After the blood vessel was sealed and scanned with OCT system, the maximum BP measurements (in mmHg) were taken in accordance with the methods in Chapter 2. A seal was judged to be successful if its BP measurement was greater than both normal systolic (120 mmHg) and hypertensive (180 mmHg) blood pressures.

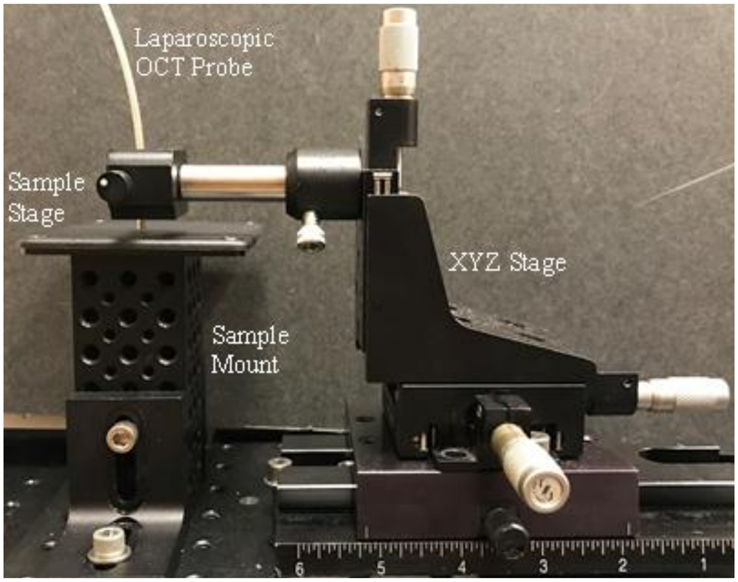

Figure 9.1: Niris, Imalux OCT system

9.2.1: Results

A total of 25 blood vessels measuring 2.4 ± 0.4 mm were sealed using fixed laser parameters. Mean burst pressure measured 532 ± 239 mmHg, with all vessels providing BP > 180 mmHg.

OCT images demonstrate the ability to differentiate visually from native and denatured tissue. Figure 9.2A shows two merged OCT frames, with cut section, compressed coagulated region, native compressed area, native uncompressed region, and blood vessel with saline in lumen. Figure 9.2B is an image with inset A-scan from native compressed region. Vessel walls produce two distinct reflection intensity peaks. Figure 9.2C is the same image with inset A-scan through coagulated region. The reflection intensity profile shows decay in reflection with depth through the tissue. Figure 9.3 shows the difference in optical transmission through native and coagulated sections of a blood vessel. A clear decrease in image depth and vessel structure is observed in the coagulated region as compared with the native tissue.

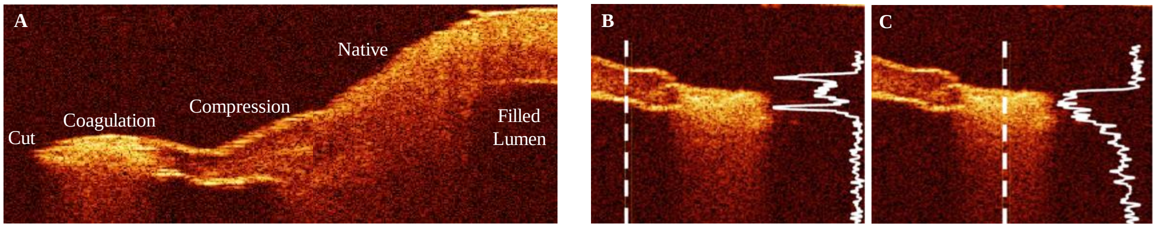

Figure. 9.2: (A) Merged OCT images of blood vessel, showing cut, compressed coagulated area, compressed native tissue, uncompressed native tissue, and vessel lumen with saline; (B) OCT images and A-scans (dashed lines) in native and (C) coagulated vessel. Native region has distinct reflection peaks at front and back vessel walls. Coagulated region has gradual decay in intensity, due to loss in vessel wall integrity and increased light scattering.

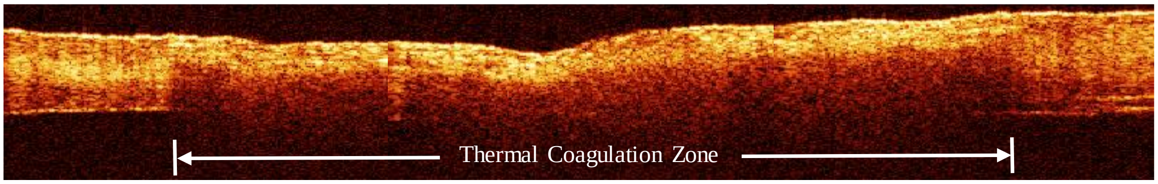

Figure 9.3: Merged OCT images showing compressed, native vessel on left and right sides and coagulated vessel in the middle region. Coagulated region measured greater than 2 mm OCT lateral scan length, so three images were taken and merged together.

Integrated reflectance intensity in OCT A-scans decreased by an average of 20 ± 6% in sealed vs. native vessels ($p < 0.01$). Figure 9.4 shows a representative OCT images with A-scans taken through unsealed and sealed regions, which are marked for comparison.

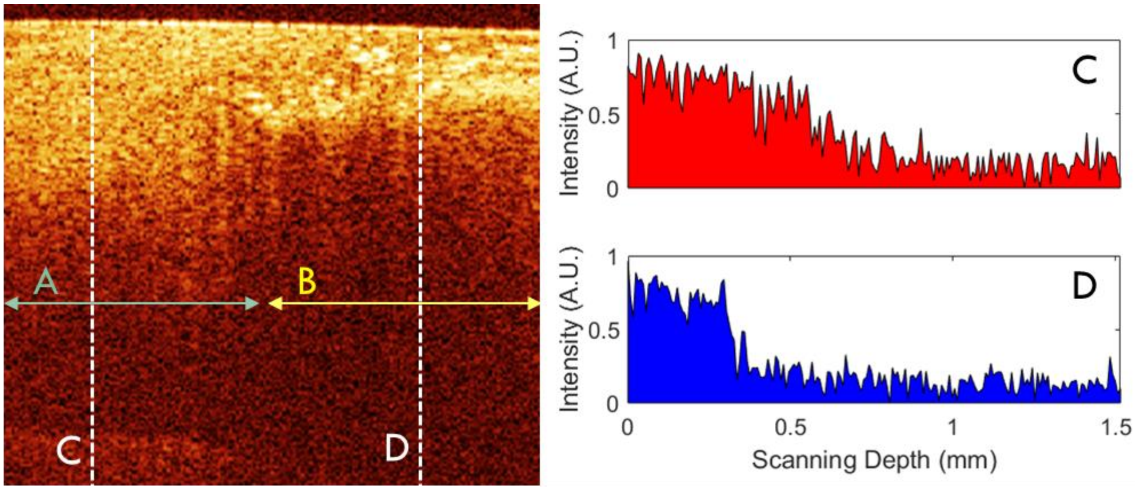

Figure 9.4: A representative OCT image of a 2.2 mm blood vessel and analysis. Left shows the raw OCT image of both the native (A) and coagulated seal (B) sections of an infrared sealed blood vessel with burst pressure measuring 450 mmHg. The right (C, D) shows two integrated reflectance intensity plots over the depth of the vessel (corrected for the vessel wall refractive index of 1.38) [91].

9.2.2: Discussion

This study demonstrated that a time-domain OCT system and compact laparoscopic probe is capable of consistently differentiating between unsealed and sealed regions of blood vessels. Although spectral domain and swept source OCT systems are also readily available, these systems are significantly more expensive, and their improved resolution, image acquisition speeds, and 3D imaging capability may be unnecessary for this simple application. Instead, it is anticipated that utilization of A-scan depth profilometry data through the center of the seal zone may be sufficient. A smaller probe may also be more easily integrated into one of the jaws of the laparoscopic device, if lateral scanning is not needed.

Recently, Doppler imaging using a spectral domain OCT system was also used as a novel approach for experimental evaluation of blood flow and hemostasis after vessel seals [89]. However, this study was performed with a thulium fiber laser at about 1940 nm and using small vessels of only 0.5 mm diameter, and without vessel compression as a variable. By contrast, standard RF and US sealing device are commonly used clinically on larger vessels of 1-5 mm. It is also typical of such devices to compress the vessel and thus displace any blood present at the seal site prior to sealing.

Although spectral domain and swept source OCT systems are also available, these systems are more expensive, and their improved resolution and acquisition speeds with 3D imaging capability may be unnecessary for this application. OCT is capable of sufficient resolution and image depth to differentiate native and coagulated blood vessels during IR laser sealing.

Another optical approach, utilizing change in optical properties, is optical transmission from a diagnostic beam during IR coagulation of blood vessels, which our lab is also developing as another potential feedback system. The next section will focus on the feasibility of transmission optical feedback systems.

9.3: Compressed Transmission Signal Collection

Another method to observe changes in optical properties of coagulated tissue is through changes in the optical signal transmission. This presents a simpler and more cost-effective detection method over OCT when transitioning the technology to a laparoscopic probe. A direct optical measurement of transmission through a thin sample can be taken to determine the total attenuation coefficient, μ_t. As shown in Chapter 3, the total attenuation coefficient is defined as the summation of the absorption and scattering coefficients. When a sample of a human aorta is subject to sufficient heat to affect its cellular structure, it is accompanied by a significant increase in the reduced scattering coefficient [62]. Previously discussed in Chapter 3, the reduced scattering coefficient is directly related to the scattering coefficient and the anisotropy factor. When soft tissue under goes photo-thermal events the scattering coefficient, OPD, anisotropy factor, index of refraction, albedo, and the scattering angle of the tissue are all effected. The scattering coefficient has been seen to change more drastically than any of the other parameters. At 1470 nm, the light scattering coefficient of native, compressed blood vessels is about 267 cm^{-1} versus 357 cm^{-1} for coagulated, compressed blood vessels [87,61,62]. Under these conditions, the reduction of transmission of 1470 nm light through tissue due to only scattering increase will be reduced by about 30%. The objective of this study is to determine whether the reduction in light transmission signal, indicating thermal coagulation, also correlates with vessel strength in terms of burst pressure (BP) measurements. If this is the case, then instead of using fixed laser parameters for vessels of different size and composition, the optical transmission signal can potentially be used as a more reliable, non-destructive indicator of a successful blood vessel seal.

9.3.1: Optical Simulations of Diffuse Light Transmission through Tissue

A basic Monte Carlo (MC) model using MATLAB code [59,60] was used as a proof-of-concept model to observe photon distribution in a compressed blood vessel before and after IR laser thermal coagulation of tissues and to determine if this difference can be used as a detection method.

The MC model considered a random walk simulation in 3D space. As a photon travels through the model, it moves from one absorption or scattering event to the next, until the photon either exits the tissue sample or becomes fully absorbed by the tissue. The fluence rate pattern exiting the compressed blood vessel at r = 400 μm is calculated by:

$$\delta(r) = \frac{N_a(r)}{\Delta V(r) N \mu_a(r) \zeta} \tag{9.1}$$

where r is the depth in the sample, $\delta(r)$ is the fluence rate, $N_a(r)$ is the total fractional absorbed packet in a given matrix element and is based on the absorption and scattering and coefficients, $\Delta V(r)$ is the volume of tissue element, N is the total number of photons which enter the simulation, $\mu_a(r)$ is the absorption coefficient, and ζ is the initial weight of each photon [92].

A homogenous plane parallel geometry was used to simulate distribution of photons deposited in a compressed (flattened) blood vessel. Three million photons were simulated to achieve sufficient (4 μm axial) spatial resolution and distribution of light absorbed in tissue. Both 1470 nm (near-IR) and 635 nm (visible) wavelengths were simulated because both wavelengths were used in this dissertation for diagnostic purposes, during non-real-time and real-time detection, respectively (real-time feedback will be explored more in Chapter 10).

Figure 9.5 shows a center slice for both native and coagulated tissue of the MC plots in the vessel for the laser spatial beam profile of 8.4 × 2.0 mm at 1470 nm and 635 nm. The fluence exhibits a peak just below the surface of the vessel, due to contributions from back-scattered photons, and then follows an exponentially decaying trend, as expected. The decay in fluence rate for the coagulated blood vessel is steep, due to enhanced light scattering effects in coagulated tissue. The discrete optical properties of normal and coagulated aorta under compression were extrapolated from existing literature for all wavelengths used in this study (Figure 9.5) [61,62]. Figure 9.5 also provides the calculated percent change of normalized fluence rate at 400 μm between native and coagulated blood vessels for 1470 nm and 635 nm. This percent change in normalized fluence is the minimum amount of expected change which should present itself as a decrease in optical power readings, during optical transmission studies for IR laser sealing of blood vessels.

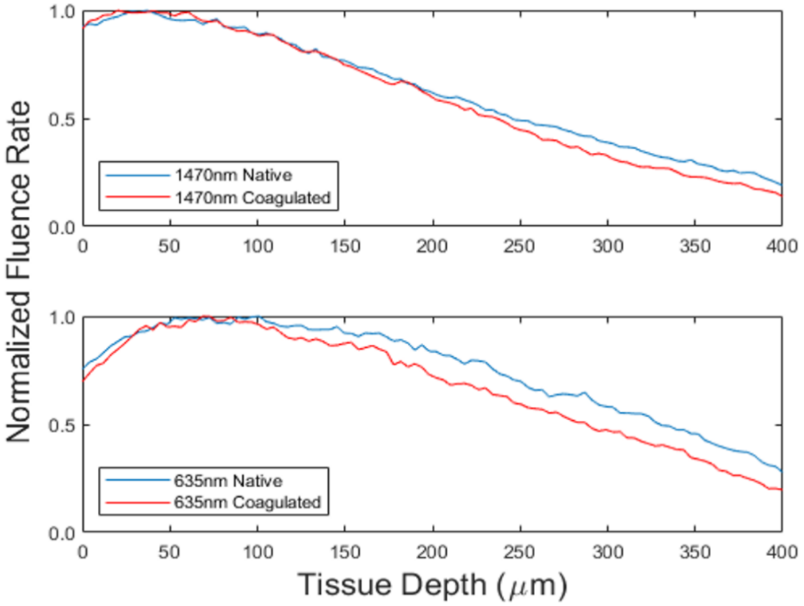

Wavelength, λ (nm)		1470	635
Absorption Coefficient μ_a (cm^{-1})	Native / Coagulated	20.4	1.5
Scattering Coefficient μ_s (cm^{-1})	Native	267	440
	Coagulated	357	590
Anisotropy Factor g	Native / Coagulated	0.875	0.875
Tissue thickness (mm)	Native / Coagulated	0.4	0.4
Simulated Change in Fluence (%)		26	29

Figure 9.5: A center slice of MC simulation after absorption of three million photons in the vessel (compressed to a fixed thickness of 400 μm) using a laser spatial beam profile of 8.4 × 2.0 mm. (Top) Normalized fluence rate 1D plot of 1470 nm for both native and coagulated tissue; (Bottom) Normalized fluence rate 1D plot of 635 nm for both native and coagulated tissue. (Right) Optical properties of native and coagulated compressed blood vessels at 1470 and 635 nm. Calculated percent change in fluence rate at 400 μm penetration depth from native to coagulated state [61,62].

9.3.2: Diffuse Optical Transmission Bench Test Methods

Two bench-top experimental setups were used in this study for a non-real-time diffuse optical transmission detection system. This experiment was designed to create both weak (BP < 360 mmHg) and strong (BP ≥ 360 mmHg) seals on medium size (2-4 mm diameter) blood vessels of equivalent size in each of the three treatment groups. Variable seal structures were created by delivering laser energy at three different times (1, 3, and 5 s). The diagnostic arm of this experiment analyzed the blood vessel samples before and after therapeutic treatment, for comparison of the results to their corresponding BP measurements. A correlation was then determined between BP strengths and non-destructive testing modalities.

The therapeutic sealing treatment benchtop setup consisted of 110-W, 1470 nm, near-IR diode laser (BrightLase Ultra-500, QPC Lasers, Sylmar, CA) radiation delivered through an armored, 400-μm-core, silica fiber optic patch-cord (QPC Lasers). Previous studies demonstrated that the laser operating at either 90 W or 30 W was capable of consistently sealing blood vessels with laser irradiation times of 1 s or 5 s, respectively. The beam was collimated by a 35 mm focal length plano-convex lens to an 8.4 mm diameter beam spot. This collimated beam was then converted into a linear beam profile by a cylindrical lens with a 100 mm focal length, thus creating a therapeutic sealing beam measuring 8.4 x 2.0 mm. An IR spatial beam profiler (Pyrocam III, Spiricon, North Logan, UT) was used to image the beam. The linear beam was aligned perpendicular to the blood vessel direction. The blood vessel was compressed to a fixed thickness of 0.4 mm between a 1 mm thick glass slide and a backplate with a 3 mm thick glass slide insert.

The diagnostic collimated light transmission benchtop setup data was collected with a separate experimental setup, both before and after high-power laser seals treatments were completed. These optical transmission measurements were acquired on an optical benchtop setup designed to optimize the collection of collimated light and exclude large scattered angles. A low power 1470 nm, pigtailed, single-mode, near-IR diode laser (QFLD-1470, Qphotonics, Ann Arbor, MI) was operated at 10 mW and the light was transmitted through a single-mode fiber (SMF) and coupled with a red aiming beam (QFLD-660, QPhotonics) with a power of 20 mW, using a SMF 90/10 fiber coupler (1×2 SM Dual Window Coupler, FIS, Oriskany, NY) and collimated to a 3 mm beam spot (Thorlabs, CFS-1550-APC, Newton, NJ). The beam was then passed through a neutral density (ND) filter to create a 5.6 mW circular beam profile. In this case, the red aiming beam was used for alignment only and was turned off during measurements.

A custom tissue compression system was then used to compress the blood vessel to a fixed thickness of 0.4 mm, similar to that of the high-power laser seal setup. The tissue compression system consisted of two custom aluminum plates with 2.5 cm holes, two 1 mm thick glass slides, two 0.4 mm compression gauge, and two wing nuts which were spring-loaded to ensure constant pressure on the compressed blood vessel. An iris closed down to 1 mm was placed on the front end of an Indium Gallium Arsenide (InGaAs) photodetector (PDA400, Thorlabs, Newton, NJ) to eliminate scattered light. The iris and detector were then placed against the back glass of the tissue compression system. The detector was connected to a digital voltage meter. Tissue was tested for collimated light transmission before and after the therapeutic seals. For detection after creation of the therapeutic seals, an aiming beam was used to visually align the beam with the seal zone. The optical components for both the therapeutic seal beam treatment setup and the collimated light transmission detection setup are shown in Figure 9.6. For this study, a lower power of 30 W was chosen, so that the laser irradiation time could be extended and separated into three distinct treatment groups of 1, 3, or 5 s, with the intention that the shortest laser irradiation time (1 s) would purposely and consistently result in failed seals, and thus, serve as a control group for the study.

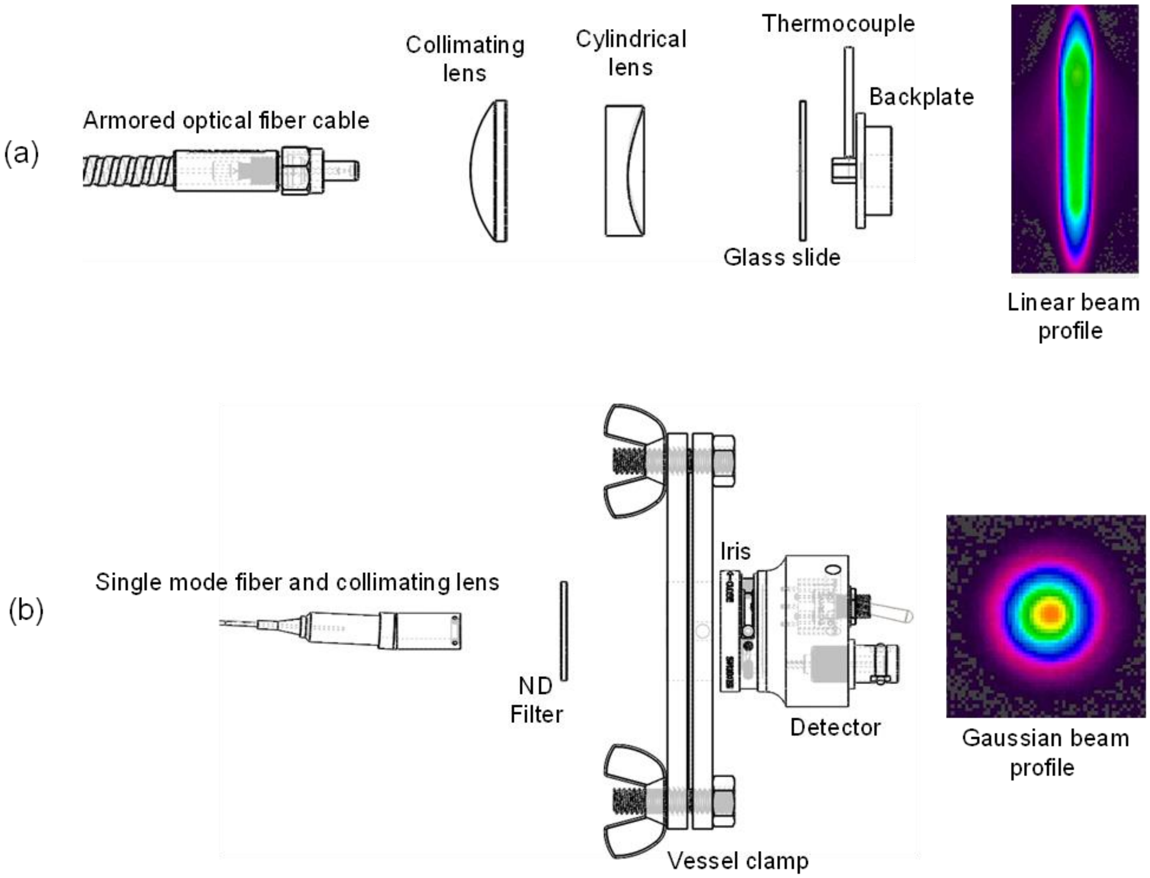

Figure 9.6: (a) Diagram of optical components used for high power laser sealing of the blood vessels, with linear beam profile shown on right; (b) Diagram of low power transmission measurements before and after sealing, with Gaussian single-mode beam profile on right.

9.3.3: Results

In general, a longer laser irradiation time corresponded to a higher BP and a decrease in transmission percentage, as expected. Figure 9.7a shows a scatter plot of the individual BP data for all of the blood vessels tested (n = 57), with the criteria for success (≥ 360 mmHg), hypertensive blood pressure (180 mmHg), and systolic blood pressure (120 mmHg) marked as horizontal colored lines, for reference. Figure 9.7b shows a representative photograph of a successful blood vessel seal. The thermal spread (TS) is indicated as a vertical dashed red line across the seal zone.

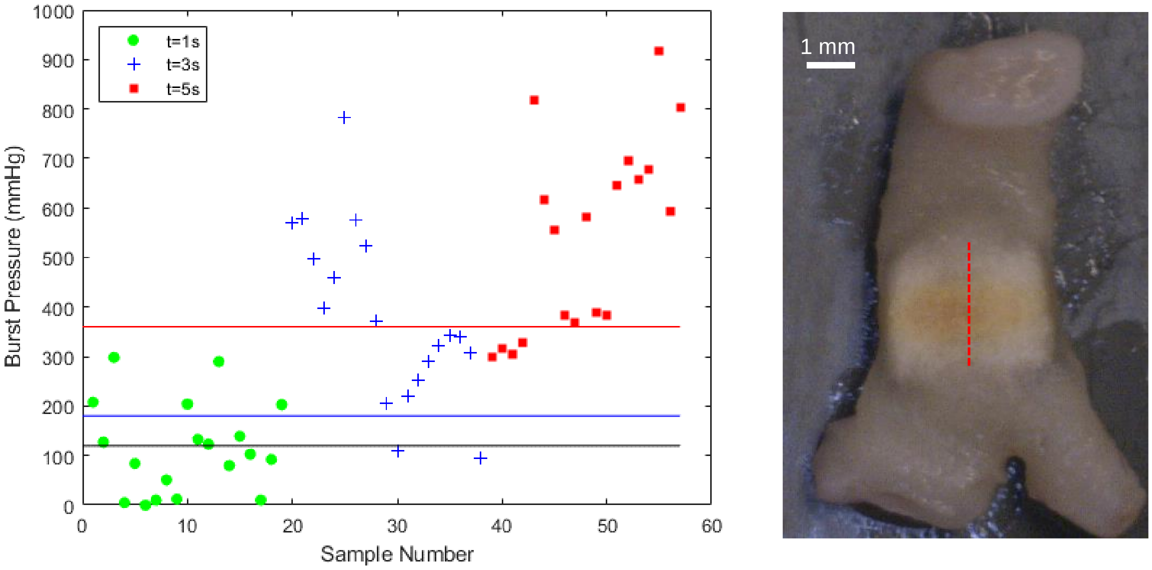

(a) (b)

Figure 9.7: (a) Scatter plot showing BP data for 57 vessels tested. Colored data points separate out data as a function of treatment time (1, 3, or 5 s). Horizontal lines show criteria for success (> 360 mmHg), hypertensive blood pressure (180 mmHg), and systolic blood pressure (120 mmHg). (b) Photograph of successful laser seal (t = 5 s, d = 3.3 mm, TS = 2.7 mm, BP = 581 mmHg).

Table 9.1 classifies the results as a function of the vessel burst pressure, with successful seals exceeding the industry test standard of 360 mmHg. The differences in burst pressure and percentage decrease in optical transmission were both statistically significant ($p < 0.01$). There was no statistical difference in blood vessel diameters between test groups ($p > 0.01$), as designed.

Table 9.1: Decrease in optical power transmission at a near-IR wavelength of λ = 1470 nm for successful seals (≥ 360 mmHg) and failed seals (< 360 mmHg).

Burst Pressure (mmHg)	**Vessel Size (mm)**	**Laser Time (s)**	**ΔPower (%)**	**Sample Number (n)**
Success (≥ 360)	2.8 ± 0.7	4.2 ± 0.9	56 ± 25	24
Failure (< 360)	3.0 ± 0.7	2.0 ± 1.4	31 ± 24	33
Significance	$p > 0.01$	$p < 0.01$	$p < 0.01$	

9.3.4: Discussion

There were several limitations of this study to be addressed in future studies. First, diffuse optical transmission measurements were not performed in real-time or with the high-power sealing setup. Instead, the goal was to demonstrate a correlation between destructive BP measurements and non-destructive optical transmission measurements, which can potentially be implemented in a clinical setting. Second, a closed-loop, automated feedback system was not used to deactivate the laser when a seal was completed. Instead, short laser irradiation times were intentionally used to produce failed seals for comparison with successful seals. Third, the photodetector was not integrated into a laparoscopic device. Instead, this study focused on demonstrating the feasibility of the concept. Fourth, only a narrow range of laser parameters were tested, again, to demonstrate proof of principle.

9.4: Conclusion

This chapter demonstrated optical sensing methods which were statistically significant in the changes between successful and failed blood vessel seals, after laser irradiation. Both of these optical sensing methods, OCT and diffuse optical transmission detection, were capable of distinguishing between coagulated and native tissue. OCT is capable of sufficient resolution and image depth to differentiate native and coagulated blood vessels under compression during infrared laser sealing. However, OCT can be cumbersome, delicate, and expensive as compared with diffuse optical transmission power detection. For these reasons, future chapters will primarily pursue the transmission detection method for laparoscopic vessel sealing. The next chapter will focus on integrating a photodetector into a real-time diagnostic feedback device during near-IR laser vessel sealing.

CHAPTER 10: REAL-TIME DIFFUSE OPTICAL TRANSMISSION MEASUREMENTS FOR CONFIRMATION OF VASCULAR SEAL STRUCTURE

10.1: Introduction

The current method in which our laboratory has quantified seal strengths of blood vessels is through destructive testing (burst pressure tests). Such tests are the industry standard method for benchtop testing of current commercial blood vessel sealing devices. However, if the seal strength is to be quantified in real-time during a surgical procedure, destructive testing of the blood vessel is not a viable option. It is common for conventional energy-based devices to incorporate real-time diagnostic feedback during surgery, in the form of electrical impedance measurements and/or temperature sensors [93-95]. This real-time feedback enables the surgeon to have a higher degree of confidence that a strong vessel seal has been achieved and also may serve as a closed feedback loop for automating energy delivery, thus saving valuable operating room time.

This chapter will explore various options for real-time monitoring of vessel seal strengths using a bulk bench top laboratory setup. First, an integrated real -time optical transmission signal change in coagulated tissue will be implemented. Previously, in Chapter 9, the ability to distinguish between native and coagulated tissue in a non-real-time environment was demonstrated. This chapter will attempt to expand on this approach and determine if this evaluation is valid in real-time. A second approach will track in real- time the temperature in a bulk optic sealing setup to indicate when a successful seal in the blood vessel has been formed. As discussed in previous chapters, temperature can be a strong indicator for thermal coagulation of proteins in soft tissues. Both methods will be judged based on their potential for laparoscopic probe integration for real- time seal detection.

10.2: Fiber Optic Measurements

10.2.1: Methods

This section explores an optical method for diagnostic feedback of blood vessel sealing using a real-time approach, to complement optical based sealing and bisection of blood vessels. The diagnostic feedback system will take advantage of the difference in the distribution of photons through native and thermally coagulated tissue. It is well known that when soft tissues are coagulated, the light scattering coefficient (μ_s) increases significantly, resulting in a reduced optical transmission through the tissue [61-63,96,97]. This reduced optical signal can therefore, potentially be used as a non-destructive source of feedback, in vivo, if a strong correlation is determined with the standard destructive indicator of a successful vessel seal in the form of blood vessel burst pressure (BP). The objective of this preliminary laboratory study is to determine whether the reduction in light transmission correlates with blood vessel strengths using a standard destructive BP setup. During this study, arteries (ranging from 2-4 mm in diameter) were surgically dissected from fresh porcine kidney pairs as discussed in detail in Chapter 2.

This section describes simultaneous detection and sealing of blood vessels using an integrated real -time diffuse optical transmission feedback system. This feedback system collected diffused light transmitted through a blood vessel sample during the transformation from its native to thermally coagulated state. The intensity of the light collected decreased as the vessel became coagulated which is a direct result of the dynamic scattering coefficient observed during laser coagulation of blood vessels. Due to the deeper optical penetration depth and need to control power output before and during diagnostics, all sensing was performed with a low power visible aiming beam, thus enabling filtering out of the high-power near-IR therapeutic sealing beam.

This experiment utilized a single bulk benchtop setup which mirrored a classic Maryland style jaw, potentially utilizing the bottom jaw for therapeutic applications while simultaneously utilizing the top jaw for transmission diagnostics. The setup consisted of a 1470-nm laser (for therapeutics) and an integrated co-aligned aiming beam 635 nm (for diagnostics), delivered via a multimode (MM) optical fiber controlled by a time gated shutter. The light was then collimated by a 35 mm focal length plano-convex lens to an 8.4 mm diameter beam spot and focused by a cylindrical lens with a 100 mm focal length onto a compressed blood vessel sample. The sample was compressed between a 1 mm glass slide and a custom backplate, which was precision machined to seat a 3 mm glass slide with a 400-µm gap stop for uniform compression. The backplate contained a 1 mm hole open to the glass slide to allow diffuse light from the tissue to be transmitted. The backplate was also machined and threaded to accommodate an SMA fiber connector attachment which was concentric with the 1 mm through hole for MM fiber connection.

A 1000-µm-core-diameter optical fiber with 0.50 NA was attached to the backplate, which was opposite the vessel from the incident laser beam and collected diffusely transmitted light. A large core, large NA fiber was used to capture the dynamic change in photon scattering during laser irradiation. The fiber output was attenuated and filtered with a low pass filter, and then focused onto a silicon photodetector (DET110, Thorlabs). Data was then collected via an oscilloscope (Figure 10.1).

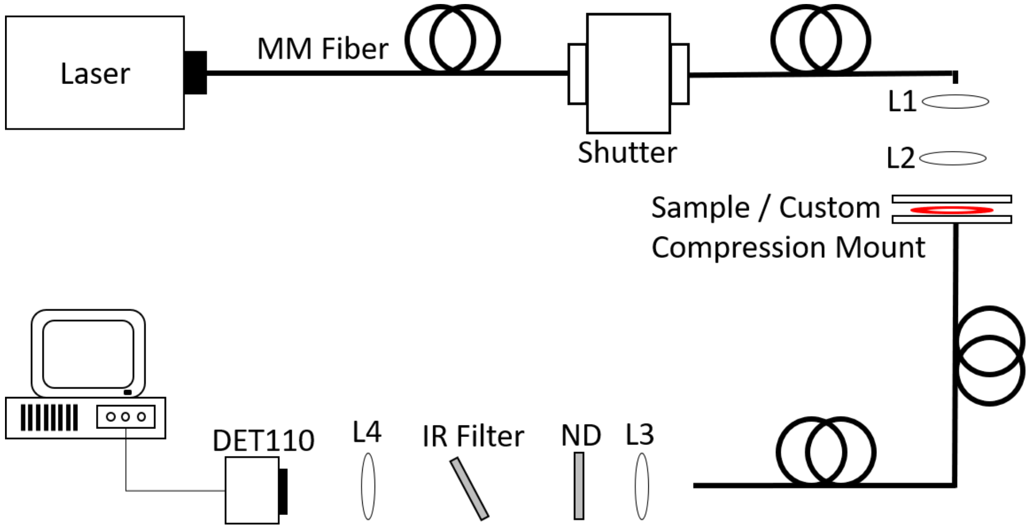

Figure 10.1. Real-time optical transmission setup, with 1470 nm therapeutic and 635 nm diagnostic beams coupled into a multimode (MM) fiber with beam shaping via a collimating lens (L1) and cylindrical lens (L2) to form a linear beam profile of 8.4 x 2 mm. The blood vessel sample was clamped with a custom mount, allowing diffuse scattered light to be collected by a MM fiber. The diagnostic beam was collimated (L3), filtered (ND & IR filters), and focused (L4) into a detector.

The 1470 nm laser was either operated at 30 W for 5 s, for successful seals or 5 W for 5 s for failed seals (control). The red aiming beam (1.2 mW at 635 nm), co-aligned with the near-IR beam, was used for real-time optical feedback during sealing. All studies used a linear beam measuring 8.4 x 2.0 mm. Optical signals for successful (n = 12) and failed (n = 12) seals were correlated with vessel burst pressures using destructive testing via a standard BP setup. After completion of near-IR laser vessel sealing and non-destructive testing of all vessel seals, standard BP measurements were conducted to determine seal strength. The BP setup consisted of a pressure meter (Model 717 100 G, Fluke, Everett, WA), syringe pump (Cole Parmer, Vernon Hills, IL), and an iris as a clamp. Deionized water was pumped at a rate of 28 mm^3/s and maximum pressure achieved was recorded. A seal was considered successful if it reached three times systolic blood pressure (360 mmHg), consistent with industry standards for testing in the field.

10.2.2: Results

Light scattering increased significantly as vessel lumens were thermally coagulated, leading to a decay in real-time power readings. Figure 10.2a shows a scatter plot of the BP data for all vessels tested (n = 24), with criteria for success (360 mmHg), hypertensive blood pressure (180 mmHg), and systolic blood pressure (120 mmHg) marked for reference. Successful seals correlated with a percent decrease in optical transmission signal of 59 ± 11 % while seal failures corresponded to a decrease of only 23 ± 8% ($p < 0.01$). The smaller decrease in transmission for failed seals was due to increased scattering of the light from the surface of the partially thermally coagulated vessel. For the vessel lumen to be completely sealed, the scattering coefficient must rise sufficiently to produce a 59% decrease in optical transmission. Figure 10.2b shows a representation of the real-time power data acquired during a sealing procedure. The signal begins with a high amplitude at $t = 0$ s, when the laser is first activated, and then continues to decay, until the laser is de-activated at $t = 5$ s. The first, lower power treatment group (5 W for 5 s) exhibits a slower decay rate than that of the second, higher power treatment group (30 W for 5 s). The large initial decay in signal, observed in Figure 10.2 in the 30 W group, is representative of the initial rapid change in the tissue optical properties and was constant for all samples collected at these settings. The decay in both signals represents the rise in the scattering coefficient during the procedure. As the scattering coefficient increases, the angle of the light exiting the tissue exceeds the NA of the fiber, which in turn translates into the lower signal acquisition.

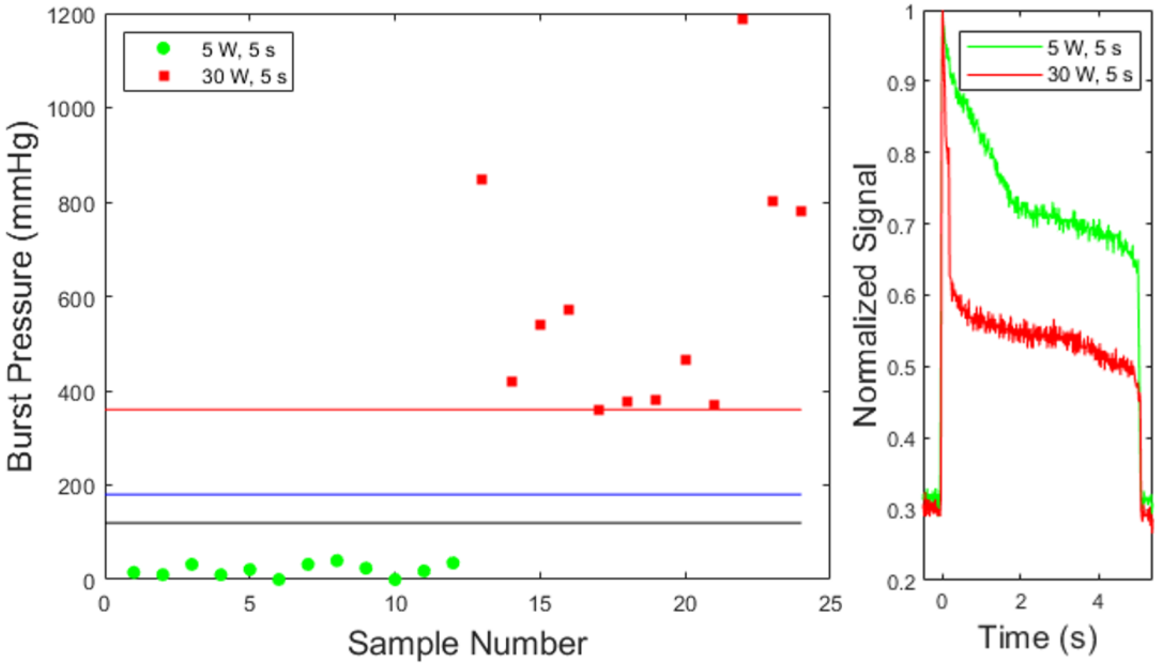

Figure 10.2: (a) Scatter plot showing BP data for the 24 vessels tested. Colored data points separate data as a function of laser irradiation time (30 W for 5 s and 5 W for 5 s), while horizontal colored lines represent criteria for success (360 mmHg), hypertensive blood pressure (180 mmHg), and systolic blood pressure (120 mmHg). (b) Representation of real time power data acquired during the sealing procedure. The green line represents a 5 W, 5 s seal of a 3.1 mm diameter blood vessel with BP = 10 mmHg (failed seal) and a percent decrease in signal of 34%. The red line represents a 30 W 5 s seal of a 3.1 mm blood vessel with a BP = 540mmHg (successful seal) and a percent decrease in signal of 50%.

Table 10.1 classifies the results as a function of vessel BP, with successful seals exceeding the industry test standard of 360 mmHg. Differences in BP and percentage decrease in optical power transmission were both statistically significant ($p < 0.01$). There was no statistical difference in blood vessel diameters between test groups ($p > 0.01$), as designed.

Table 10.1: Decrease in optical power transmission at the visible wavelength of λ = 635 nm for successful seals (≥ 360 mmHg) and failed seals (< 360 mmHg).

Burst Pressure (mmHg)	**Vessel Size (mm)**	**Mean Burst Pressure (mmHg)**	**ΔPower (%)**	**Sample Number (n)**
Success (≥ 360)	3.3 ± 1.0	592 ± 248	59 ± 11	12
Failure (< 360)	2.4 ± 0.7	19 ± 12	23 ± 8	12
Significance	$p > 0.01$	$p < 0.01$	$p < 0.01$	

10.2.3: Real-Time Detection (Optical Diffuse Transmission in Near-IR, λ = 1470 nm)

Figure 10.3 shows the erratic signal acquired when the high-power therapeutic beam at 1470 nm is also used for diagnostic feedback as well. The data was inconsistent and unreliable due in part to competing changes in the dynamic tissue optical properties. For example, the water absorption coefficient decreased upon tissue dehydration during laser heating, translating to an increase in the optical transmission signal. However, the scattering coefficient increases upon tissue coagulation, translating into a decrease in the optical transmission signal.

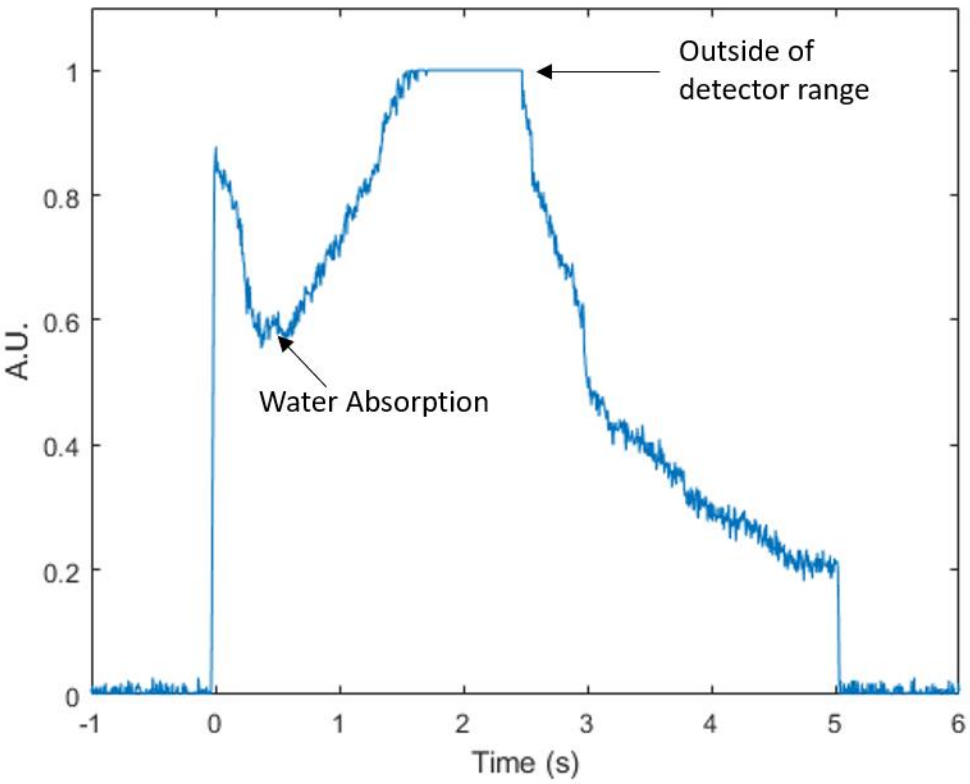

Figure 10.3: Representative real-time optical power transmission data during the sealing procedure, using the high power therapeutic 1470 nm wavelength as the diagnostic beam. At t = 0 s, the laser is activated, leading to an initial instantaneous rise in signal. The erratic signal between t = 0 and t = 5 s can be attributed in part to the different contributions and time scales of competing changes in the dynamic tissue optical properties: increased transmission signal due to tissue dehydration (lower absorption coefficient), but also decreasing transmission signal due to tissue coagulation (increased scattering coefficient). The loss of signal in the range of t = 1.5 - 2.5 s is due to saturation for the given detector setting.

10.2.4: Discussion

Results of real-time optical transmission measurements demonstrated the ability to non-destructively predict successful vessel seals (≥ 360 mmHg). The increase in the scattering coefficient for a successfully sealed blood vessel corresponded to a 59% loss in transmitted power. This percent difference is significantly higher than the MC model predicted in Chapter 9. This discrepancy originates, in part, due to the model using scattering and absorption coefficients derived from existing literature, for human aorta thermally damaged at 100°C, while the vessel must experience a much higher temperature of 200-300°C to achieve a successful seal [87]. This difference in temperature accounts for the higher scattering and greater decrease in signal during the experiments. It may also account for percent change in transmitted power for seal failures closely correlating with the calculated value, since the maximum temperature reached in these failed samples is much closer to the 100°C used in the scattering coefficient estimation.

Another factor in the discrepancy between the MC model simulation results and the experimental results involves the NA of the collection fiber. The simulations do not have an aperture to filter out light at scattered angles too large for the fiber to collect. This factor also contributes in part to the larger decrease in signal measured during the experiments. This model also did not account for the small changes in absorption, index of refraction, and anisotropy factor, which can create a larger discrepancy in the before and after signal transmission.

The 635 nm visible aiming beam is preferable to the 1470 nm near-IR beam for real-time diagnostic feedback, for several reasons. First, the 635 nm beam was operated at a low power, thus enabling a safe and simple means to acquire a calibrated, baseline starting signal for each individual blood vessel of variable diameter. This is an important criterion, since the marker for a successful seal is observed by a relative measurement in the form of a percent change. Since the 1470 nm laser is operated at high power, it is impossible to safely collect a baseline transmission before beginning the procedure. Any high-power laser beam should be filtered out, translating into the need for two different wavelengths for the therapeutic and diagnostic arms of this study.

Second, the 635 nm beam is preferable for diagnostic purposes because its wavelength avoids a major water absorption peak in soft tissues. On the contrary, a major water absorption peak present at 1450 nm prevents reliable real-time diagnostics using the 1470 nm diode laser. At 1470 nm, a large initial spike in the data was observed after the tissue became dehydrated during laser irradiation, which resulted in an inherently unstable optical transmission signal, in turn making analysis inconsistent and unpredictable (Figure 10.3). The source of the problem is that tissue hydration level is altered within a given tissue sample during rapid laser heating and dehydration, and may also vary across different tissue samples as well, based on the vessel thickness or diameter.

Third, the optical diagnostic setup using the 635 nm beam as a probe enabled the high power 1470 nm beam to be completely filtered out during detection. Any potential risk of laser-induced damage to the optical detector from direct incidence of the high power 1470 nm beam was therefore eliminated.

There are several limitations to this study. First, the studies were all performed in a bulk optics setup not practical for use in a clinical setting. This technology will need to be miniaturized for integration into a standard laparoscopic device and Maryland jaw configuration, as a next step in its development, before in vivo tests can be performed. To aid in this miniaturization process, a smaller collection fiber may be necessary, which could make signal collection more difficult to achieve, unless a larger NA can be used to compensate for the smaller fiber optic core diameter.

A second limitation concerns the fixed laser beam length used for all blood vessels, regardless of their diameter. In practice, use of a fixed laser beam length may result in partial overflow of the beam when incident on smaller diameter blood vessels, in turn corresponding to an initially inflated optical power transmission signal. In future laparoscopic probes, adjustable beam lengths via a reciprocating side firing fiber may be available for different vessel diameters, to compensate for this limitation.

10.3: Thermocouple Measurements

10.3.1: Methods

A similar bulk optics compression set up as discussed in Chapter 5 will be used for sealing blood vessels. Temperature will be monitored from the back of the compression plates via a micro-thermocouple. A thermocouple (Omega, 5TC-TT-T-24-72, Norwalk, CT) was placed on top of the backplate and receded 5 mm away from the glass insert for protection and to prevent the potential for erroneous temperature measurements from potential direct absorption of scattered photons by the thermocouple. A digital data acquisition system (OM-USB-TC, Omega) was connected to the micro-thermocouple to record all of the data. The temperature readout measured the heat that is transferred from the vessel through the glass slide to the backplate. The baseline temperature and maximum temperature during laser sealing were then compared and the difference recorded. The change in temperate was then compared to the burst pressure of each vessel.

10.3.2: Results

In a total of 57 blood vessels samples, samples with burst pressures greater than 360 mmHg achieved a percent change in temperature of 59 ± 32%, burst pressures between 180-360 mmHg achieved a percent change in temperature of 32 ± 2.9%, and burst pressures less than 180 mmHg achieved a percent change in temperature 14.7 ± 9.4 % as seen in Table 10.2. As expected, the lower irradiation times corresponded to lower burst pressures which gave us a wide range of blood vessels seal strength to analyze. Figure 10.4 shows representative peak temperatures measured directly corresponding to the specific vessel samples tested. In general, a longer laser irradiation time corresponded to a larger burst pressure and increase in backplate temperature.

Table 10.2: Percent change in temperature between samples sealed with burst pressures >360 mmHg, 180 – 360 mmHg, and < 180mmHg.

	> 360 (mmHg)	**180-360 (mmHg)**	**< 180 (mmHg)**
% Change	59 ± 32^{a,c}	32 ± 2.9^{b,c}	14.7 ± 9.4^{a,b}
Time (s)	4.3 ± 1.0	2.8 ± 1.5	1.3 ± 0.7
Vessel Size (mm)	2.8 ± 0.8	2.8 ± 0.8	3.2 ± 0.8
Sample Number	24	17	16

a: Statistically significant ($p < 0.01$) > 360 mmHg, b: Statistically significant ($p < 0.01$) 180-360 mmHg, c: Statistically significant ($p < 0.01$) < 180 mmHg.

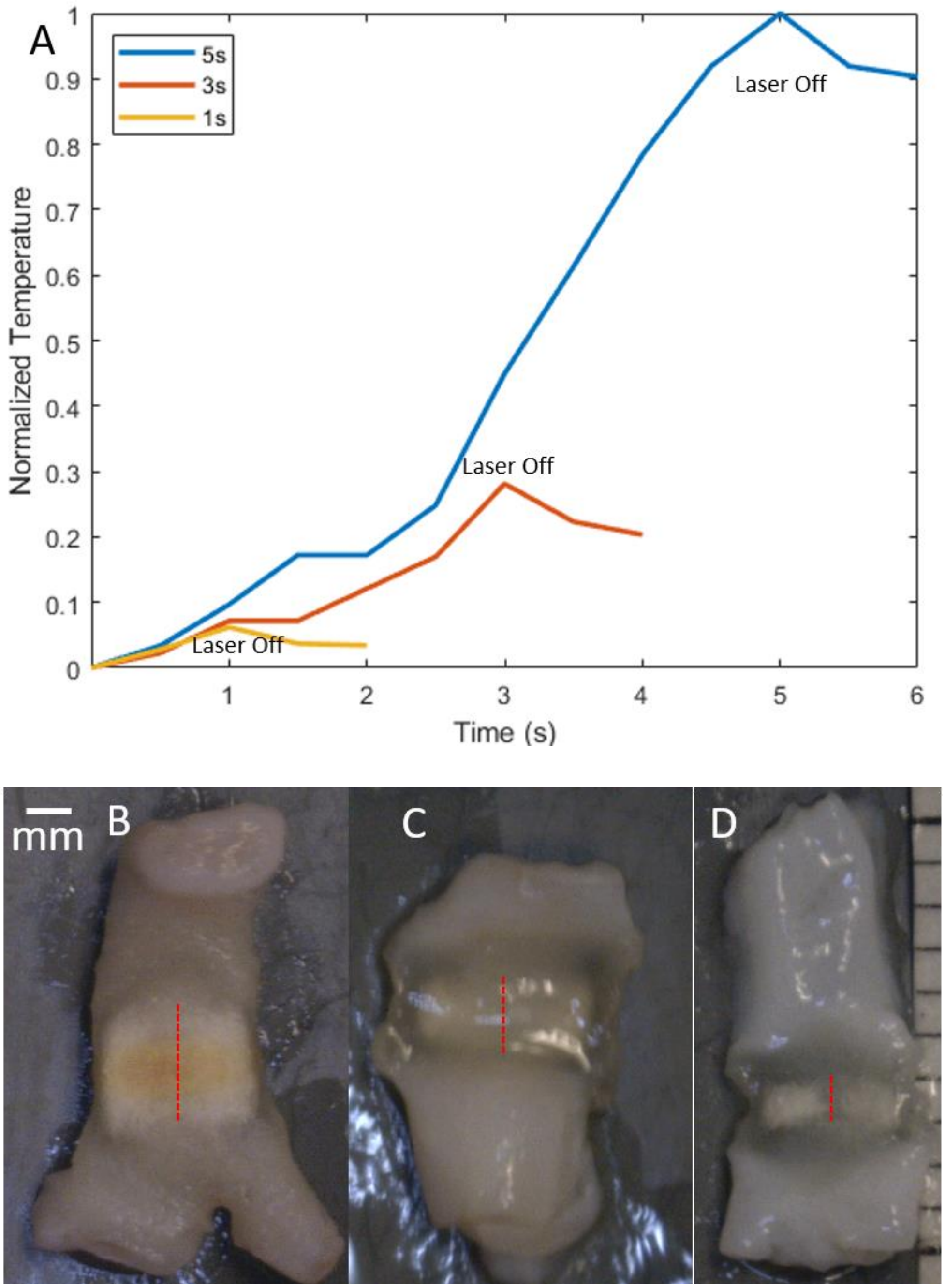

Figure 10.4: (A) Representative temperature lines are shown corresponding to the specific vessel samples photographs. The temperature peak for each curve corresponds to the time at which the laser was turned off. (B) 5 s seal: 3.3 mm diameter vessel with thermal spread 2.7 mm and burst pressure of 581 mmHg. (C) 3 s seal: 2.8 mm diameter vessel with thermal spread 1.7 mm and burst pressure of 340 mmHg. (D) 1 s seal: 3.0 mm diameter vessel with thermal spread 1.0 mm and burst pressure of 80 mmHg.

10.4: Conclusions

This study demonstrated that a non-destructive method utilizing thermal diffusion and optical transmission of scattered visible light through a blood vessel consistently predicts a strong vessel seal during irradiation and thermal coagulation with a high-power infrared laser. With further development, both micro-thermocouples and fiber optic collection component of the real-time optical transmission feedback method technology may be integrated into the laparoscopic device jaw. These preliminary studies provide the foundation for development of a laparoscopic device which has the capability to both seal blood vessels and provide real-time feedback using only optical technology. The prototyping of this device will be explored in the next chapter.

CHAPTER 11: LAPAROSCOPIC BLOOD VESSEL SEALING AND CUTTING PROBE DESIGN WITH REAL-TIME OPTICAL FEEDBACK

11.1: Introduction

This dissertation has developed the proof of concept for a laparoscopic laser sealing and cutting technology and has developed both the therapeutic and diagnostic instrumentation for miniaturizing into a laparoscopic prototype. This chapter will outline the potential mark 1 design for the Detection Aided Laser Sealing and Cutting Instrument (DALSCI). Feedback designs will be incorporated both for blood vessel sealing confirmation and for safety. This chapter will be an engineering guide for design and fabrication of the mark 1 DALSCI.

The laser, chiller, shutter, controller, and power supply will be on an external supply rack. This supply rack will be described in detail in a later section. The therapeutic delivery system in the DALSCI will be, as discussed in Chapter 8, the oscillating 40-degree angled side-firing fiber in the bottom jaw. A fiber will run from the shutter to the body of the device through a port in the back. This port will be a fiber coupler connection with the side angled fiber. This side angled fiber will be aligned with the shaft of the device and mounted on a custom servo. The oscillatory motion will be achieved through the servo motor equipped with a custom 3D printed clamp for maintaining the fiber orientation. The servo motor will be mounted inside the body of the device and operated by a momentary switch located on the handle. The servo will run on a preprogramed Arduino Uno board, as seen in Chapter 8, which will be externally mounted in the controller box (program found in APPENDIX E). Standard Amphenol style stranded wire assembly will be used for power and ground lines and coaxial cable connections should be used for data lines. The duration of the CW beam will be regulated by the external shutter. The shutter will be operated manually by a momentary switch located on the handle of the device, but will also feature a safety override system regulated by external temperature registered by micro-thermocouples mounted on the jaw. The override cutoff system temperature should be easily changed by external users. In order to transform the sealing device to a cutting device the blood vessel will need to be translated closer to the fiber for a tighter beam spot as discussed in Chapter 5. The servo motor which is holding the fiber should translate up after the sealing procedure is complete. The spot size will be reduced from 2 mm in diameter to 1 mm in diameter, shown in Chapter 5 to produce significant power density for cutting blood vessels.

The diagnostic feedback system within the DALSCI will be integrated into the top jaw of the laparoscopic device. The top jaw will consist of a 0.5 mm thick glass slide followed by a metal backing plate. A 1 mm diameter hole will be put in the center of the backplate. Above and hole will be a small 1 mm, 45-degree angled, mirror (Part# 47-628, Edmund Optics, Barrington, NJ) which will be reflective for 630 nm matching the diagnostic beam as discussed in Chapter 10**.** Concentric with the center of the mirror will be a fiber collection system very similar to the setup in Chapter 10. This fiber will run the length of the shaft into the body of the device. In the back of the body of the device it will connect to a mounted fiber coupler. On the other side of this coupler will be another fiber which will connect to the external supply rack for diagnostics. Inside the diagnostic box, on the supply rack, will be a series of optics which lead to the detector with the same set up as in Chapter 10. The detector will change the optical input into a voltage output. This voltage output can be monitored with a small microprocessor and can signal a successful seal when the power drops 60% from its original starting value as demonstrated in Chapter 10. The indication of the seal will be indicated by a green LED as a readout on the front of the diagnostic box. A potential future engineering guide for both the therapeutic and diagnostic integration into a laparoscopic probe is provided in Sections 11.2.

11.2: Mark 1: Design for Detection Aided Laser Seal and Cutting Instrument (DALSCI)

11.2.1: Assembly 1: External Tower

The external tower will consist of six individually assembled boxes: Power supply, Laser, Chiller, Safety system, Shutter, and Diagnostic box each will be explained in further detail below. The tower will be 50 x 50 x 70 cm in size, a relatively small but heavy footprint, requiring it to be on wheels, similar to that of the Olympus empower H100 100 W laser system used in surgical rooms for kidney stone ablation. The Assembly of the tower is seen in Figure 11.1 in perspective with a commercially available Olympus system currently being used in surgical settings.

Figure 11.1: Comparison of (Left) 1470nm 100W DALSCI system and (Right) Olympus 100W kidney stone ablation system, drawn to scale.

11.2.2: Subassembly 1: Safety System

This safety system will be used to monitor the external temperature of the device. If the external temperature approaches a predetermined temperature, a yellow LED will flash. If the temperature exceeds this temperature, a red LED will flash. Two of these electrical systems are run in tandem; the first for the top jaw and the second for the bottom jaw. The jaws will be monitored by micro-thermocouples (300-µm diameter, OMEGA, 5TC-TT-T-36), which run back to a DAQ (MAX31855k, Sparkfun, Boulder, CO) located inside the handle of the device. The DAQ will than transmit the temperature information to the Arduino located inside the safety box. The Arduino will run modified open source code to signal the indicating lights which will be mounted to the front panel of the safety box.

11.2.3: Subassembly 2: Laser, Chiller, and Power Supply

The laser (BrightLase, Ultra-500 High Power Fiber Coupled Module, QPC Lasers, Sylmar, CA)), chiller (T225P_1R, Thermotek, Flower Mound, TX), and power supply (LDX-36000, ILX Lightwave, Bozeman, MT) will be the same as used in the previous studies. The laser diode module sits on an external cooling plate which is kept at 20^{o}C by the chiller. The aiming beam will also need to be powered by an external power supply of 3 V. This external power supply can be found in the Output Shutter and Oscillation controller box. If the aiming beam is to be used for detection, the ideal power supply needs to be stable to ± 0.1 V. All modules are relatively compact and can be mounted in a configuration, as shown in Figure 11.2.

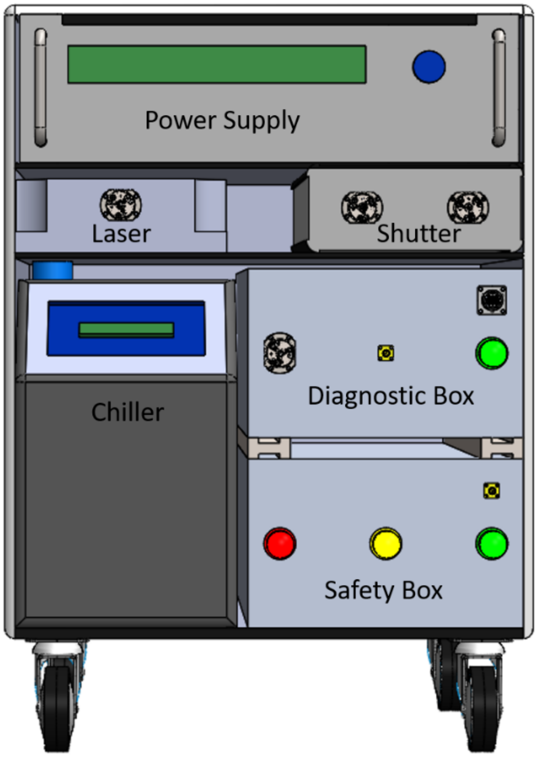

Figure 11.2: Layout of all external tower components with dimensions of 70 x 50 x 50 cm.

11.2.4: Subassembly 3: Output Shutter and Oscillation Controller

The optical shutter layout will use a high-powered optical shutter (SH-200-55-1470-M-0-T-BH-SP, OZ Optics, Ottawa, Canada). This optical shutter box will operate with fiber optics with no open-air optics needed. The box will have two box mounted mating sleeves, one for input and another for output. Signal lines will also be run to the handheld device which will be operate the shutter with a momentary button. The oscillation controller will be a pre-programmed Arduino with a signal line running to the handheld device operated with a switch. A fail safe might also be necessarily to prevent the shutter from remaining open if the fiber is not oscillating which could help avoid errant operation.

11.2.5: Subassembly 4: Diagnostic Box

Similar to Chapter 10, the diagnostic beam will be channeled from the diagnostic arm of the handheld device to a diagnostic box located on the external tower assembly. The diagnostic box contents can be seen in Figure 11.3. The diagnostic box will consist of two lenses, one for collimation and the other to focus the light into the detector, and a near-IR filter to allow only the 635 nm diagnostic beam to propagate throughout the system. ND filters will also be integrated into the design to attenuate the beam to a level inside the detectors range. A filter wheel can be used in the diagnostic box for the mounting option for the ND filter, this might be necessary for dealing with smaller or larger vessels if the beam intensity variation exceeds the detector range. The diagnostic box also shows a micro controller, Arduino Uno, which can be used to signal the green light on the front of the box once the vessel has been determined to be sealed. It should be noted that along with the micro-controller, a micro-processor may also be necessary for this evaluation.

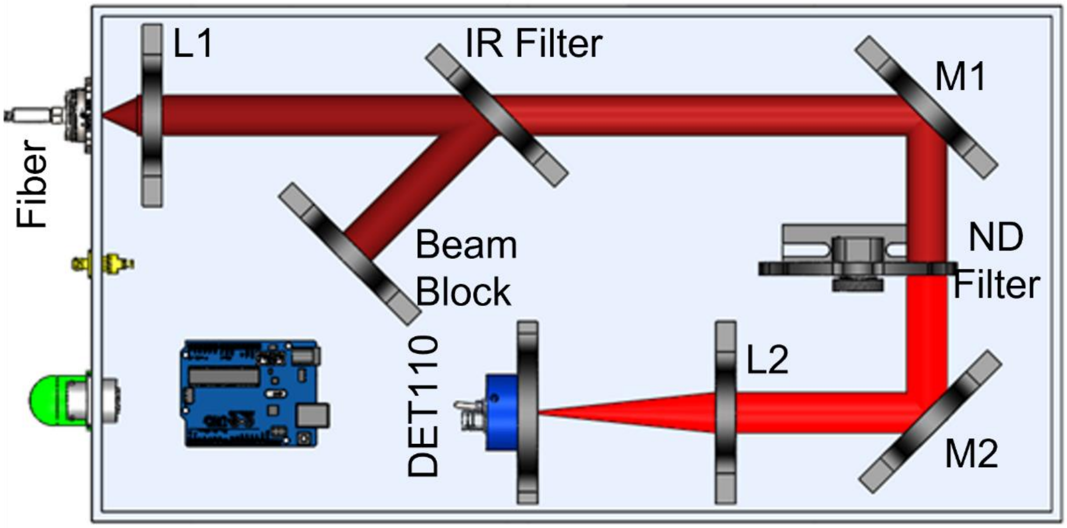

Figure 11.3: The diagnostic box: shows a SMA fiber connection, lens for collimation, IR filter and beam block, mirrors (for light guides), ND filters for attenuation, and silicon detector (DET110, Thorlabs).

11.2.6: Assembly 2: Handheld Device

A handheld device similar to existing devices, as seen in Figure 7.1, will be created for surgical procedures. The handheld portion of the device will consist of three distinct parts: diagnostic upper jaw, therapeutic lower jaw, and the device housing. The device housing, seen in Figure 11.4, will house two DAQ boards for computing the external thermocouple temperatures, a servo motor with rail system, and a diagnostic fiber. The servo motor with rail system will be mounted on a piezo operated platform. The servo system will be similar to the design in Chapter 8 but will be redesigned to allow for a more fluid motion creating a more uniform linear beam profile. The diagnostic fiber will be mounted on an optical sleeve mount on the back part of the housing. The housing will also feature an 8 pin for all power, signal and ground connections as well as two fiber optic mounts for therapeutic and diagnostic fibers. The housing and handles will be 3D printed. The handles should be constructed to incorporate the mechanical draw for the jaw actuation, one momentary button to control the shutter and a switch to control the motion oscillation.

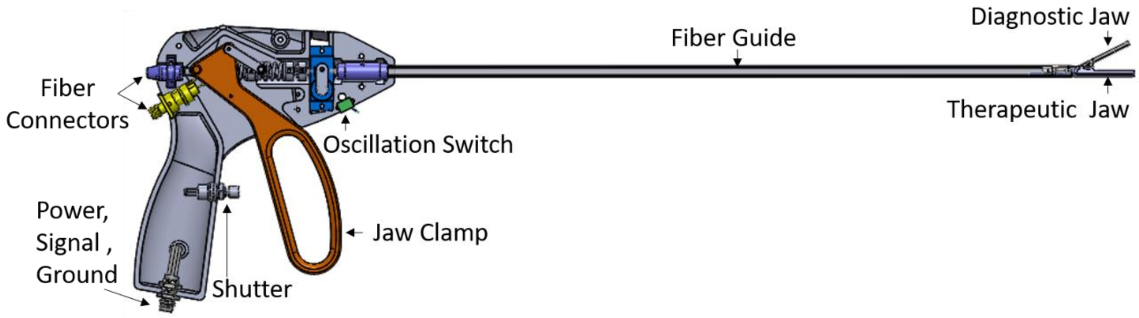

Figure 11.4: Section view of the DALSCI.

11.2.7: Subassembly 1: Therapeutic Fiber Oscillation

The therapeutic aspect of the jaws will operate solely in the lower jaw. The side-firing fiber will be actuated back and forth creating a linear beam profile, as discussed in Chapter 8. The light will diverge out of the side of the distal fiber tip and propagate through the glass slide into the compressed tissue above. The distance from the fiber tip to the tissue will provide a 2 mm beam profile, as seen in Chapter 8. Once the blood vessel is sealed, the fiber will be translated upward towards the glass slide. This translation will cause the tissue to be irradiated with a smaller beam profile, 1 mm in diameter. This smaller beam profile will create a larger fluence which is large enough to cut the vessel in the center of the sealed region, as seen in Chapters 4-6. The translation of fiber will take place in the handle of the device by moving the servo and guide rail with precision piezo actuators.

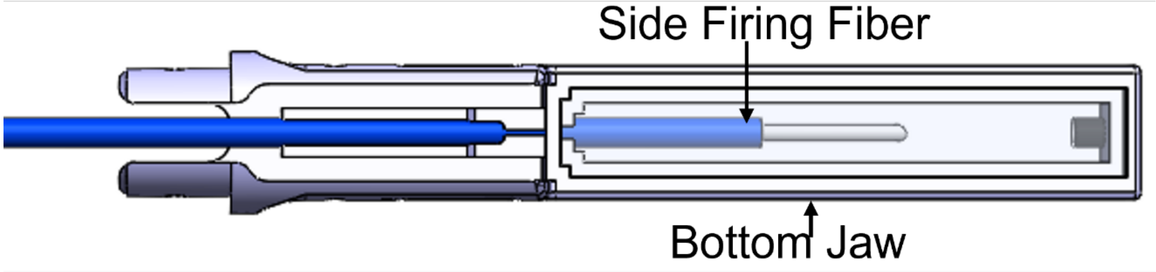

Figure 11.5: Therapeutic jaw.

11.2.8: Subassembly 2: Diagnostic Fiber Delivery

The transmission optical power diagnostic will be packaged in the top jaw. The top jaw will be made up of a glass slide with a metal backing. In the metal backing, a 1 mm hole will be made in the center to allow light to transmit through to the diagnostic area, as seen in Chapter 10.

A flat 1 mm mirror will reflect the light into a fiber. This fiber will run the length of the device and be connected to a fiber sleeve in the housing of the handheld device.

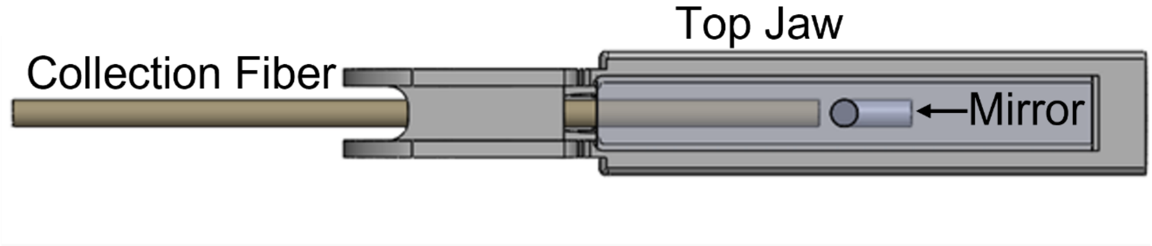

Figure 11.6: Diagnostic jaw design.

CHAPTER 12: CONCLUSIONS

This dissertation developed a scientific understanding for developing a novel laser system for vessel ligation, bisection, and real-time feedback tool. Chapters 1 - 4 underlined the fundamental understanding for interactions between lasers and soft tissues with the emphasis on blood vessel coagulation and vaporization. Potential wavelengths for sealing and cutting blood vessels were also reviewed, which ultimately lead to the use of the 1470 nm wavelength. Chapters 5 and 6 introduced the understanding of power density and fluence, and how beam shaping can be used to dynamically transition from a tissue state of coagulation to a state of vaporization. These chapters also modeled the extensive matrix of parameters which are involved in order to optimize the sealing and cutting beams. Since Chapters 1 - 6 demonstrated the basic underlining fundamental principles of vessel sealing, Chapters 7 - 8 moved away from a proof-of-concept bench top optical configuration and focused on the fabrication of a miniaturized optical setup. The miniaturization of the optical components was constrained to the size of a standard laparoscopic probe (5 mm in diameter). The optimal configuration was found to be an oscillating or reciprocating side-firing fiber. The side-firing fiber was polished at an angle of 40^o and oscillated using custom mounts and servos. This configuration was able to withstand the appropriate power and compete with the sealing times of devices currently available on the market.

Chapters 9 and 10 focused on an optical feedback system which can be implemented during the laser blood vessel sealing procedure to indicate when a successful seal is created. Diffuse optical transmission feedback was chosen as the most promising technology for seal indication and integration into a laparoscopic device. This approach is premised upon the large change in the scattering coefficient of the blood vessel during vessel coagulation. By taking advantage of the dynamic change in optical properties of the biological sample, during a photothermal interaction, a reduction in signal which corresponded to the coagulation point of the blood vessel was recorded. Chapter 11 detailed the potential engineering construction of the first laparoscopic laser sealing and cutting device utilizing optical feedback for seal confirmation. This construction incorporates both the side-firing oscillating therapeutic fiber and the diagnostic fiber for collection for real-time collection of diffusely transmitted light.

The advances described in this dissertation enable the potential for a competitive, inexpensive, robust, and repeatable laparoscopic laser sealing and cutting device with real-time optical detection.

REFERENCES

[1] P. Niki, T. Papavramidis, and T. Demetriou, "Ancient Greek and Greco–Roman methods in modern surgical treatment of cancer," Annals of surgical oncology, 17(3), 665-667 (2010).

[2] N. S. Blencowe, R. Waldon and M. N. Vipond, "Management of patients after laparoscopic procedures," BMJ, 360, k120 (2018).

[3] D. Dutta, D. Kumar, and I. Dutta, “The Harmonic Scalpel,” Journal of obstetrics and gynaecology of India, 66(3), 209-210 (2016).

[4] “Valleylab Ligasure Vessel Sealing System,” Avante Health Solutions, avantehs.com/p/valleylab-ligasure-vessel-sealing-system/952.

[5] V. C, Karande, “LigaSure™ 5-Mm Blunt Tip Laparoscopic Instrument,” J. Obstetrics and Gynecology of India, 65(5), 350–352 (2015).

[6] M. Risselada, G. W. Ellison, G. W., Bacon *et al*., “Comparison of 5 surgical techniques for partial liver lobectomy in the dog for intraoperative blood loss and surgical time,” Vet. Surg., 39(7), 856-862 (2010).

[7] Garancini, Mattia, L. Gianotti, I. Mattavelli et al. "Bipolar vessel sealing system vs. clamp crushing technique for liver parenchyma transection," Hepato-gastroenterology, 58(105), 127-132 (2011).

[8] C. Leonardo, S. Guaglianone, P. De Carli *et al.*, Laparoscopic nephrectomy using Ligasure system: preliminary experience,” J. Endourology, 19(8), 976-978 (2005).

[9] J. E. Ettinger, A. C. Ramos, E. Azaro, M. P. Galvao-Neto, *et al.*, “Staplerless laparoscopic gastric bypass: a new option in bariatric surgery,” Obes. Surg., 16(5), 638-645 (2006).

[10] A. Stoff, M. A. Reichenberger, and D. F. Richter, “Comparing the ultrasonically activated scalpel (Harmonic) with high-frequency electrocautery for postoperative serious drainage in massive weight loss surgery,” Plastic Reconstrue Surg, 120(4), 1092-1093 (2007).

[11] R. E. Brolin, and R. P. Cody, “Impact of technological advances on complications of revisional bariatric operations,” J. Am. Coll. Surg., 206(3), 1137-1144 (2008).

[12] Y. Kurt, E. Yucel, A. I. Filiz *et al.*, “New energy-based devices in laparoscopic splenectomy: comparison of Ligasure alone versus Ligasure and Ultracision together,” Surgical Practice, 16(1), 28-32 (2012).

[13] H. Shabadong, G. Maddah, A. Tavassoli, A. Jangjoo *et al.*, “Laparoscopic splenectomy: ligasure or clip ligation,” Surg. Laparosc. Endosc. Percutan. Tech, 22(2), 136-138 (2012).

[14] T. L. Smith, and J. M. Smith, “Electrosurgery in otolaryngology-head and neck surgery: principles, advances, and complications,” Laryngoscope, 111(5), 769-780 (2001).

[15] U. Lepner, and T. Vaasna, “Ligasure vessel sealing system versus conventional vessel ligation in thyroidectomy,” Scand. J. Surg, 96(1), 31-34 (2007).

[16] Y. Pons, J. Gauthier, E. Ukkola-Pons *et al.*, “Comparison of LigaSure vessel sealing system, harmonic scalpel, and conventional hemostasis in total thyroidectomy,” Otolaryngol. Head Neck Surg., 141(4), 496-501 (2009).

[17] E. P. Prokopakis, V. A. Lachanas, A. S. Vardouniotis *et al.*, “The use of the Ligasure vessel sealing system in head and neck surgery: a report on six years of experience and a review of the literature,” B-ENT, 6(1), 19-25 (2010).

[18] B. Zarebczan, D. Mohanty, and H. Chen, “A comparison of the Ligasure and harmonic scalpel in thyroid surgery: a single institution review,” Ann. Surg. Oncol., 18(1), 214-218 (2011).

[19] C. J. O’Neill, L. Y. Chang, J. W. Suliburk, *et al.*, “Sutureless thyroidectomy: surgical technique,” ANZ J. Surg., 81(7-8), 515-518 (2011).

[20] J. Kroft and A. Selk, “Energy-based vessel sealing in vaginal hysterectomy: a systematic review and meta-analysis,” Obstet. Gynecol., 118(5), 1127-1136 (2011).

[21] S. Msilka, G. Deroide, R. Kianmanesh *et al.*, “Harmonic scalpel in laparoscopic colorectal surgery,” Dis. Colon. Rectum, 44(3), 432-436 (2001).

[22] R. Rimonda, A. Arezzo, C. Garrone *et al.*, “Electrothermal bipolar vessel sealing system vs. harmonic scalpel in colorectal laparoscopic surgery; a prospective, randomized study,” Dis. Colon. Rectum, 52(4), 657-661 (2009).

[23] M. Adamina, B.J. Champagne, L. Hoffman *et al.*, “Randomized clinical trial comparing the cost and effectiveness of bipolar vessel sealers versus clips and vascular staplers for laparoscopic colorectal resection,” Br. J. Surg., 98(12), 1703-1712 (2011).

[24] T. Samson, A. Malik, S.D. Wexner *et al.*, "Energy source instruments for laparoscopic colectomy. "Cochrane Database of Systematic Reviews” 5 (2011).

[25] J. Landman, K. Kerbl, J. Rehman, *et al.*, “Evaluation of a vessel sealing system, bipolar electrosurgery, harmonic scalpel, titanium clips, endoscopic gastrointestinal anastomosis vascular staples and sutures for arterial and venous ligation in a porcine model,” J. Urol., 169(2), 697-700 (2003).

[26] S. Tou, A. I. Malik, S. D. Wexner *et al.*, “Energy source instruments for laparoscopic colectomy,” Cochrane Database Syst. Rev., 11(5), (2011).

[27] G. W. Hruby, F. C. Marrufo, E. Durak *et al.*, “Evaluation of surgical energy devices for vessel sealing and peripheral energy spread in a porcine model,” J. Urol., 178(6), 2689-2693 (2007).

[28] G. R. Lamberton, R. S. His, D. H. Jin *et al.*, “Prospective comparison of four laparoscopic vessel ligation devices,” J. Endourol., 22(10), 2307-2312 (2008).

[29] P. A. Sutton, S. Awad, A. C. Perkins *et al.*, “Comparison of lateral thermal spread using monopolar and bipolar diathermy, the Harmonic scalpel, and the Ligasure,” Br. J. Surg., 97(3), 428-433 (2010).

[30] A. M. Ong, L. M. Su, I. Varkarakis *et al.*, “Nerve sparing radical prostatectomy: effects of hemostatic energy sources on recovery of cavernous nerve function in a canine model,” J. Urol., 172(4), 1318-1322 (2004).

[31] I. S. Gill and O. Ukimura, “Thermal energy-free laparoscopic nerve-sparing radical prostatectomy: one-year potency outcomes,” Urology, 70(2), 309-314 (2007).

[32] C. K. Phillips, G. W. Hruby, E. Durak *et al.*, “Tissue response to surgical energy devices,” Urology, 71(4), 744-748 (2008).

[33] F. J. Kim, M. F. Chammas Jr, E. Gewehr *et al.*, “Temperature safety profile of laparoscopic devices: harmonic ACE, Ligasure V, and plasma trisector,” Surg. Endosc., 22(6), 1464-1469 (2008).

[34] W. L. Newcomb, W. W. Hope, T. M. Schmelzer *et al.*, “Comparison of blood vessel sealing among new electrosurgical and ultrasonic devices,” Surg. Endosc., 23(1), 90-96 (2009).

[35] B. Person, D. A. Vivas, D. Ruiz *et al.*, “Comparison of four energy-based vascular sealing and cutting instruments,” Surg. Endosc., 22(2), 534-538 (2008).

[36] R. Tanaka, M. Ryota, D. Meiselman *et al*. “Evaluation of Vessel Sealing Performance Among Ultrasonic Devices in a Porcine Model.” Surgical Innovation, 22(4), 338-343 (2015).

[37] M. N. Szyrach, P. Paschenda, M. Afify *et al.*, “Evaluation of the novel bipolar vessel sealing and cutting device BiCision in a porcine model,” Minimally Invasive Therapy & Allied Technologies, 21(6), 402-407 (2012).

[38] A. Leppäniemi, D. Wherry, E. Pikoulis *et al.*, “Arterial and Venous Repair with Vascular Clips: Comparison with Suture Closure.” Journal of Vascular Surgery, 26(1), 24-28 (1997).

[39] N. C. Giglio, T. C. Hutchens, W. C. Perkins *et al.*, “Rapid sealing and cutting of porcine blood vessels, ex vivo, using a high power, 1470-nm diode laser.” J Biomed Opt, 19(3), (2014).

[40] K. L. Harlod, H. Pollinger, B. D. Mathews *et al.*, “Comparison of Ultrasonic Energy, Bipolar Thermal Energy, and Vascular Clips for the Hemostasis of Small-, Medium-, and Large-Sized Arteries.” Surgical Endoscopy, 17(8), 1228-1230 (2003).

[41] G. M. Hale, and M. R. Querry, “Optical constants of water in the 200 nm to 200 µm wavelength region,” Appl. Opt., 12(3), 555-563 (1973).

[42] R. K. Wang, “Modelling Optical Properties of Soft Tissue by Fractal Distribution of Scatterers.” Journal of Modern Optics, 47(1), 103-120 (2000).

[43] C. Ash, M. Dubec, K. Donne *et al.*, “Effect of Wavelength and Beam Width on Penetration in Light-Tissue Interaction Using Computational Methods.” Lasers in Medical Science, 32(8), 1909-1918 (2017).

[44] M. A. Ansari, M. Erfanzadeh, and E. Mohajerani, “Mechanisms of laser-tissue interaction: II. Tissue thermal properties,” J. Laser Med. Sci. 4, 99–106 (2013).

[45] W. L. Newcomb, W. W. Hope, T. M. Schmelzer *et al.*, “Comparison of blood vessel sealing among new electrosurgical and ultrasonic devices,” Surg. Endosc. 23(1), 90-96 (2009).

[46] M. Rustagi and V. Bharihoke, “Intercranial human vertebral artery: A histomorphology study” International journal of current research and review,” IJCRR 5(12), 89-90 (2013).

[47] Y. Suzuki, S Yoriyasu, A. C. Yeung et al.,, "The representative porcine model for human cardiovascular disease.” Journal of Biomedicine and Biotechnology, (2010).

[48] R. S. Schwartz, J. G. Murphy, W. P. Edwards *et al.*, "Restenosis after balloon angioplasty. A practical proliferative model in porcine coronary arteries,” Circulation 8(6), 2190-2200 (1990).

[49] E. G. Chekan, M. A. Davison, D. W. Singleton *et al.*, "Consistency and sealing of advanced bipolar tissue sealers," Medical Devices 8, 193 (2015).

[50] D. Arrese, B. Mazrahi, M. Kalady, “Technological Advancements in tissue-sealing Devices.” General Surgert News Special Report, (2012).

[51] C. M. Cilip, S. B. Rosenbury, N. C. Giglio *et al.*, “Infrared laser thermal fusion of blood vessels: preliminary ex vivo tissue studies,” J. Biomed. Opt., 18(5) (2013).

[52] W. W. Hope, S. Padma, W. L. Newcomb *et al*, “An evaluation of electrosurgical vessel-sealing devices in biliary tract surgery in a porcine model,” HPB 12(10), 703-708 (2010).

[53] L. Wang, J. Yuan, H. Jiang *et al.*. "Vessel sampling and blood flow velocity distribution with vessel diameter for characterizing the human bulbar conjunctival microvasculature," Eye & contact lens, 42(2), 135 (2016).

[54] R. Müller, S. Lang, M. Dominetto *et al.*, "High-resolution tomographic imaging of microvessels." Developments in X-Ray Tomography, 4(7078), 70780B (2008).

[55] I. W. Sherman and V. G. Sherman., "Biology: A Human Approach," New York: Oxford UP Print, 2, 76 (1979).

[56] D. B. Camasão and M. Diego. "The mechanical characterization of blood vessels and their substitutes in the continuous quest for physiological-relevant performances. A critical review," Materials Today Bio, 100-106 (2021).

[57] J. A. Pearce and S. L. Thomsen, "Blood vessel architectural features and their effects on thermal phenomena," *Proc. SPIE*, 10297(06), 1-47 (2000).

[58] A. G. Sharp, "Design Curves for Oceanographic Pressure-Resistant Housings," Woods Hole Oceanographic Institution Technical Memorandum, 3(81), 5 (1981).

[59] D. Marti, R. N. Aasbjerg, P. E. Andersen *et al.*,, "MCmatlabL an open-source, user-friendly, MATLAB-integrated three-dimensional Monte Carlo light transport solver with heat diffusion and tissue damage," J. Biomed. Opt., 23(12), 1-6 (2018).

[60] S. L. Jacques, "Monte Carlo modeling of light transport in tissues (steady state and time of flight)," Optical-Thermal Response of Laser-Irradiated Tissue, 109-144 (2011).

[61] E. K. Chan, B. Sorg, D. Protsenko *et al.*, "Effects of compression on soft tissue optical properties," IEEE J. Sel. Top. Quantum Electron., 2(4), 943-950 (1996).

[62] I. F. Cilesiz and A. J. Welch, "Light dosimetry: effects of dehydration and thermal damage on the optical properties of the human aorta," Appl. Opt., 32(4), 477-487 (1993).

[63] J. P. Ritz, A. Roggan, C. Isbert *et al.*, "Optical properties of native and coagulated porcine liver tissue between 400 and 2400 nm," Lasers Surg. Med., 29(3), 205-212 (2012).

[64] E. Q. Chen, C. F. Lam, and A. Periasamy "Effect of refraction on optical microscopic measurement of internal blood-vessel diameter and its correction." J. Microsc., 164(3), 239-245 (1991).

[65] G. J. Müller, and A. Roggan, "Laser-Induced Interstitial Thermotherapy," SPIE Optical Engineering Press, (1995).

[66] J. W. Valvano, “Temperature dependence of human arterial tissue,” Optical-Thermal Response of Laser-Irradiated Tissue,” Heidelberg: Springer, 467-468 (2011).

[67] N. Markolf, “Laser-Tissue Interactions,” Springer Nature Switzerland , fourth edition print, 61 (2019).

[68] W. Waesche, H. Albrecht, and G. J. Muller “Determination of temperature dependence of the production of volatile organic compounds (VOCs) during the vaporization of tissue using Nd:YAG laser, CO_2 laser, and electrosurgery devices,” *Proc. SPIE*, 23(23), 1-7 (1995).

[69] F. J. Kim, M. F. Chammas Jr, E. Gewehr *et al.*, “Temperature safety profile of laparoscopic devices: Harmonic ACE (ACE), Ligasure V (LV), and plasma trisector (PT).” Surg. Endosc., 22(6), 1464-1469 (2008).

[70] G. L. LeCarpentier, M. Motamedi, L. P. McMath *et al.*,. “Continuous wave laser ablation of tissue: analysis of thermal and mechanical events,” *IEEE* Trans. Biomed. Eng., 40(2), 188-200 (1993).

[71] A. L. Mckenzie, “A three-zone model of soft-tissue damage by a CO_2 laser,” Phys. Med. Biol., 31(9), 967-983 (1986).

[72] A. J. Welch, M. Motamedi, S. Rastegar *et al.*, “Laser thermal ablation,” Photochem. Photobiol., 53(6), 815-823 (1991).

[73] A. V. Belikov, A. V. Skrypnik, S. N. Smirnov *et al.*, “Temperature dynamics of soft tissues during diode laser cutting by different types of fiber opto-thermal converters.” Proc. SPIE, 10336, 1-7 (2017).

[74] B. J. Wiatrak and J. P. Willging, “Harmonic scalpel for tonsillectomy,” Laryngoscope, 112(8), 14-16 (2002).

[75] T. A. Springer and A. J. Welch, “Temperature control during laser vessel welding,” Appl. Opt., 32(4) 517-525 (1993).

[76] J. Z. Zhang, Y. G. Shen, and X. X. Zhang, “A dynamic photo-thermal model of carbon dioxide laser tissue ablation,” Lasers Med. Sci., 24(3), 329-338 (2008).

[77] F. C. Henriques and A. R. Moritz, “Studies of thermal injury I: The conduction of heat to and through skin and the temperatures attained therein. A theoretical and experimental investigation,” Am. J. Pathol., 23(4), 530-549 (1947).

[78] A. R. Moritz and F. C. Henriques, “Studies of thermal injury II. The relative importance of time and surface temperature in the causation of cutaneous burns,” Am. J. Pathol., 23(5), 695-720 (1947).

[79] A. R. Moritz, “Studies of thermal injury III. The pathology and pathogenesis of cutaneous burns. An experimental study,” Am. J. Pathol., 23(6), 915-934 (1947).

[80] L. H. Peterson, R. E. Jensen, and J. Parnell, “Mechanical properties of arteries in vivo,” Circ. Res., 8(3), 622-639 (1960).

[81] C. Berry, “Design and development of two test fixtures to test the longitudinal and transverse tensile properties of small diameter tubular polymers.” M.S. Thesis, California Polytechnic State University, San Luis Obispo, (2011).

[82] A. C. Voegele, D. L. Korvick, M. Gutierrez *et al.*, “Perpendicular blood vessel seals are stronger than those made at an angle.” J. Laparoendosc. Adv. Surg. Tech. A., 23(8), 669-672 (2013).

[83] C. Cilip, D. Kerr, C. A. Latimer *et al.*, “Infrared laser sealing of porcine vascular tissues using a 1470 nm diode laser: preliminary in vivo studies,” Lasers Surg. Med., 49(4), 366-371, (2017).

[84] L. A. Hardy, T. C. Hutchens, E. R. Larson *et al.*, “Rapid sealing of porcine renal vessels, ex vivo, using a high power, 1470-nm laser and laparoscopic prototype,” J. Biomed. Opt. 22(5), 058002 (2017).

[85] J. J. Davenport, M. Hickey, J. P. Phillips, P. A. *et al.*, “Method for producing angled optical fiber tips in the laboratory.” Opt. Eng. 55(2), 026120 (2016).

[86] R. Pashaie and R. R. Falk, “Single optical fiber probe for fluorescence detection and optogenetic stimulation,” IEEE Trans. Biomed. Eng., 60(2), 268-280 (2013).

[87] N. C. Giglio and N. M. Fried, "Computational simulations for infrared laser sealing and cutting of blood vessels," IEEE J Sel. Top. Quantum Electron. 27(4), 1-8 (2021).

[88] J. A. Pearce and S. L. Thomsen, "Blood vessel architectural features and their effects on thermal phenomena," Proc. SPIE 10297, Matching the Energy Source to the Clinical Need: A Critical Review, 1029706 (2000).

[89] A. J. Marques, R. Reyes, CR Pasarikorski, *et al*., “Doppler optical coherence tomography for energy seal evaluation and comparison to visual evaluation,” J. Biomed. Opt. 25(3), 1-14 (2020).

[90] N. C. Giglio, T. C. Hutchens, C. M. Cilip *et al.*, “Optical coherence tomography for use in infrared sealing of blood vessels,” IEEE Photonics Conference, 1-2 (2020).

[91] J. A. Gutiérrez, E. Real, A. Pardo, José M. López-Higuera, Olga M. Conde, "Fusion of OCT and hyperspectral imaging for tissue diagnosis and assessment," Proc. SPIE 1136207 (2020).

[92] S. A. Prahl, M. Keijzer, S. L. Jacques *et al.*, "A Monte Carlo model of light propagation in tissue," Proc. SPIE 10305, 1-10 (1989).

[93] J. S. Kennedy, P. L. Stranahan, K. D. Taylor, and J. G. Chandler, “High-burst-strength, feedback-controlled bipolar vessel sealing,” Surg. Endosc. 12, 876-878 (1998).

[94] N. Shigemura, A. Akashi, T. Nakagiri *et al.*, “A new tissue-sealing technique using LigaSure system for nonanatomical pulmonary resection: preliminary results of suture less and staple less thoracoscopic surgery,” Ann. Thorac. Surg., 77, 1415-1418 (2004).

[95] R. Patrone, C. Gambardella, R. M. Romano et al., “The impact of the ultrasonic, bipolar and integrated energy devices in the adrenal gland surgery: literature review and our experience,” BMC Surg., 18, 123 (2019).

[96] M. Jasiński, "Numerical analysis of soft tissue damage process caused by laser action." AIP Conf. Proc. 1922, 060002 (2018).

[97] V. K. Nagarajan, V. R. Gogineni, S. B. White *et al.*, "Real time evaluation of tissue optical properties during thermal ablation of ex vivo liver tissues," Int. J. Hyperthermia, 35(1), 176-182 (2019).

APPENDIX A: PEER – REVIEWED PUBLICATIONS

Giglio, N. C. & N.M. Fried (2022). “Nondestructive optical feedback systems for use during infrared laser sealing of blood vessels” *Lasers in Surgery and Medicine* (*Under Review*)

Giglio, N. C., Grose, H. M., & Fried, N. M. (2022). Comparison of fiber-optic linear beam shaping designs for laparoscopic laser sealing of vascular tissues. *Optical Engineering*, 61(2), 026112.

Giglio, N. C., Hutchens, T. C., South, A. A., & Fried, N. M. (2021). Dynamic properties of surfactant-enhanced laser-induced vapor bubbles for lithotripsy applications. *Journal of Biomedical Optics*, *26*(1), 018001.

South, A. A., **Giglio, N. C**., & Fried, N. M. (2021). Simulations and testing of the mechanical properties of small core optical fibers for ureteroscopy. *Optical Engineering*, *60*(3), 036110.

Giglio, N. C., & Fried, N. M. (2021). Computational simulations for infrared laser sealing and cutting of blood vessels. *IEEE Journal of Selected Topics in Quantum Electronics*, *27*(4), 1-8.

Cilip, C. M., Kerr, D., Latimer, C. A., Rosenbury, S. B., **Giglio, N. C**., Hutchens, T. C., ...& Fried, N. M. (2017). Infrared laser sealing of porcine vascular tissues using a 1,470 nm diode laser: Preliminary in vivo studies. *Lasers in Surgery and Medicine*, *49*(4), 366-371.

Giglio, N. C., Hutchens, T. C., Perkins, W. C., Latimer, C., Ward, A. K., Nau Jr, W. H., & Fried, N. M. (2014). Rapid sealing and cutting of porcine blood vessels, ex vivo, using a high-power, 1470-nm diode laser. *Journal of Biomedical Optics*, *19*(3), 038002.

Cilip, C. M., Rosenbury, S. B., **Giglio, N. C**., Hutchens, T. C., Schweinsberger, G. R., Kerr, D. E., ... & Fried, N. M. (2013). Infrared laser thermal fusion of blood vessels: preliminary ex vivo tissue studies. *Journal of Biomedical Optics*, *18*(5), 058001.

Acknowledged:

L. Hardy, T. Hutchens, E. Larson, D. Gonzalez, C. Chang, W. Nau, & N. M. Fried, "Rapid sealing of porcine renal blood vessels, ex vivo, using a high power, 1470-nm laser, and laparoscopic prototype," *J. Biomed. Opt.* 22(5), 058002, 2017.

APPENDIX B: CONFERENCE PROCEEDINGS

Giglio, N. C., Grose, H. M., & Fried, N. M. (2022). Fiber optic beam shaping designs for laparoscopic laser sealing of vascular tissues. In *Diagnostic and Therapeutic Applications of Light in Cardiology 2022 (Pending)*

Giglio, N. C., & Fried, N. M. (2022). Real-time optical feedback system for infrared laser sealing of blood vessels. In *Optical Coherence Tomography and Coherence Domain Optical Methods in Biomedicine 2022 (Pending)*

Giglio, N. C., Grose, H. M., & Fried, N. M. (2022). Optical coherence tomography feedback system for infrared laser sealing of blood vessels. In *Diagnostic and Therapeutic Applications of Light in Cardiology 2022 (Pending)*

Giglio, N. C., & Fried, N. M. (2021). Optical transmission feedback for infrared laser sealing of blood vessels. In *European Conference on Biomedical Optics* (pp. EW4A-47). Optical Society of America.

Giglio, N. C., & Fried, N. M. (2021). Sealing and bisection of blood vessels using a 1470 nm laser: optical, thermal, and tissue damage simulations. In *Diagnostic and Therapeutic Applications of Light in Cardiology 2021* (Vol. 11621, p. 1162108). International Society for Optics and Photonics.

Giglio, N. C., South, A. A., & Fried, N. M. (2021). Characterization of a prototype miniature digital ureteroscope tip for enabling office-based thulium fiber laser lithotripsy. In *Advanced Photonics in Urology* (Vol. 11619, p. 116190F). International Society for Optics and Photonics.

South, A. A., **Giglio, N. C**., & Fried, N. M. (2021). Simulating manual manipulation of small optical fibers within flexible ureteroscopes for potential application in thulium fiber laser lithotripsy. In *Advanced Photonics in Urology* (Vol. 11619, p. 1161908). International Society for Optics and Photonics.

Giglio, N. C., Hutchens, T. C., Cilip, C. M., & Fried, N. M. Optical coherence tomography for use in infrared laser sealing of blood vessels. In *2020 IEEE Photonics Conference (IPC)* (pp. 1-2). IEEE.

Giglio, N. C., Hutchens, T. C., Wilson, C. R., Gonzalez, D. A., & Fried, N. M. (2020). Surfactant enhanced laser-induced vapor bubbles for potential use in thulium fiber laser lithotripsy. In *2020 42nd Annual International Conference of the IEEE Engineering in Medicine & Biology Society (EMBC)* (pp. 5045-5048). IEEE.

Hutchens, T. C., **Giglio, N. C**., Cilip, C. M., Rosenbury, S. G., Hardy, L. A., Kerr, D. E., ... & Fried, N. M. (2020). Novel Optical Linear Beam Shaping Designs for use in Laparoscopic Laser Sealing of Vascular Tissues. In *2020 42nd Annual International Conference of the IEEE Engineering in Medicine & Biology Society (EMBC)* (pp. 5049-5052). IEEE.

Gonzalez, D. A., **Giglio, N. C**., Hall, L. A., Vinnichenko, V., & Fried, N. M. (2019). Comparison of single, dual, and staircase temporal pulse profiles for reducing stone retropulsion during thulium fiber laser lithotripsy in an in vitro stone phantom model. In *Therapeutics and Diagnostics in Urology 2019* (Vol. 10852, p. 108520E). International Society for Optics and Photonics.

Cilip, C. M., Hutchens, T. C., Kerr, D., Latimer, C., Rosenbury, S. B., **Giglio, N. C**., ... & Fried, N. M. (2015). Infrared laser sealing of porcine tissues: preliminary in vivo studies. In *Photonic Therapeutics and Diagnostics XI* (Vol. 9303, p. 930319). International Society for Optics and Photonics.

Giglio, N. C., Hutchens, T. C., Perkins, W. C., Latimer, C., Ward, A., Nau, W. H., & Fried, N. M. (2014). Rapid infrared laser sealing and cutting of porcine renal vessels, ex vivo. In *Photonic Therapeutics and Diagnostics X* (Vol. 8926, p. 892619). International Society for Optics and Photonics.

Cilip, C. M., Rosenbury, S. B., **Giglio, N**., Hutchens, T. C., Schweinsberger, G. R., Kerr, D., ... & Fried, N. M. (2013). Thermal sealing of blood vessels using infrared lasers. In *Photonic Therapeutics and Diagnostics IX* (Vol. 8565, p. 85654B). International Society for Optics and Photonics.

Acknowledged:

L. Hardy, T. Hutchens, E. Larson, D. Gonzalez, C. Chang, W. Nau, & N. M. Fried, "Laparoscopic prototype for optical sealing of renal blood vessels," *Proc. SPIE* 10038, 100380V, 1-7, 2017.

APPENDIX C: PATENTS

Thomas C. Hutchens, Nathaniel M. Fried, **Nicholas C. Giglio**, “Enhanced laser induced vapor bubbles,” U.S Patent Application #63/017,212, Jan. 2020.

APPENDIX D: CUSTOM PARTS

Backplate with 1 mm through hole and SMA insert:

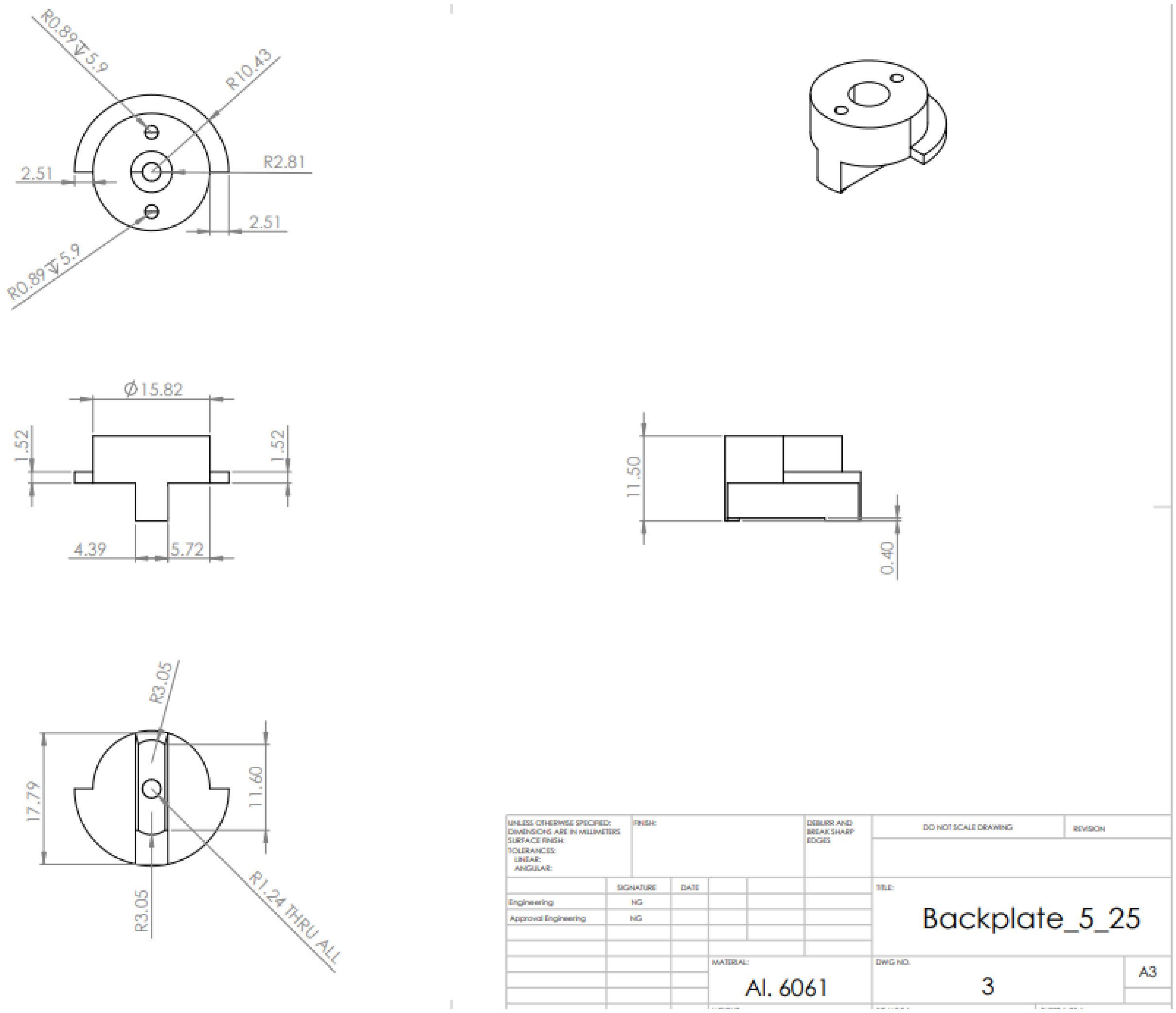

Compression front and backplate:

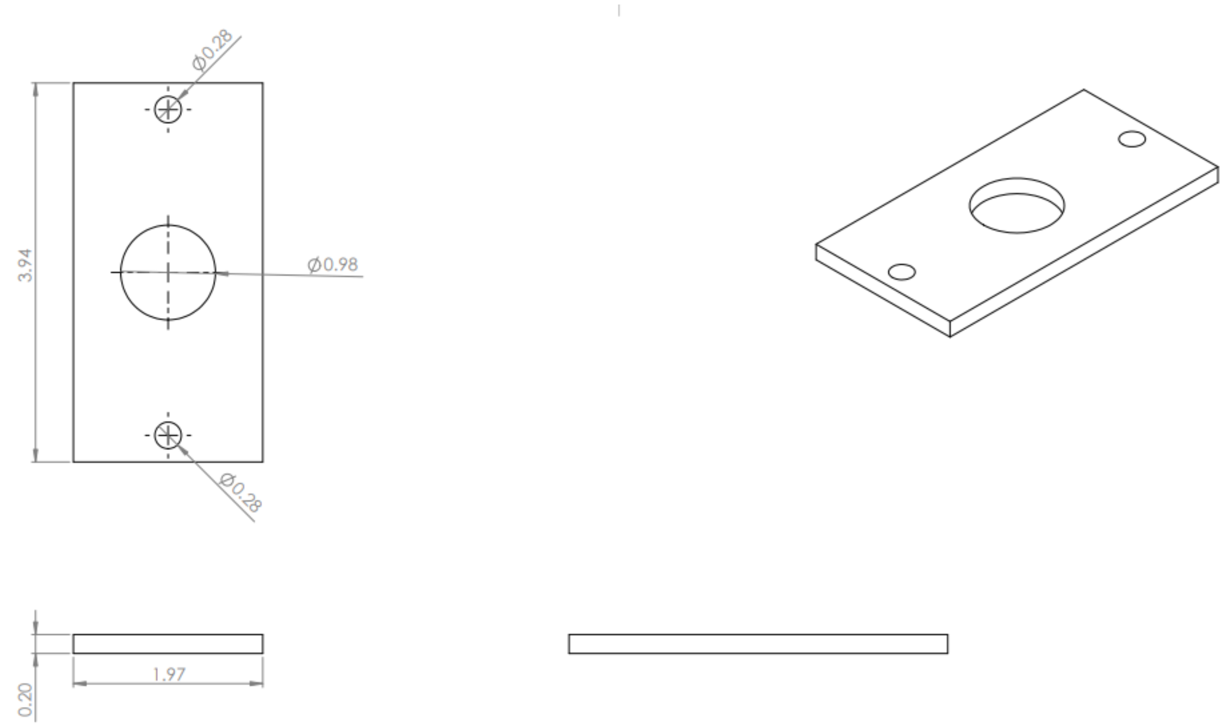

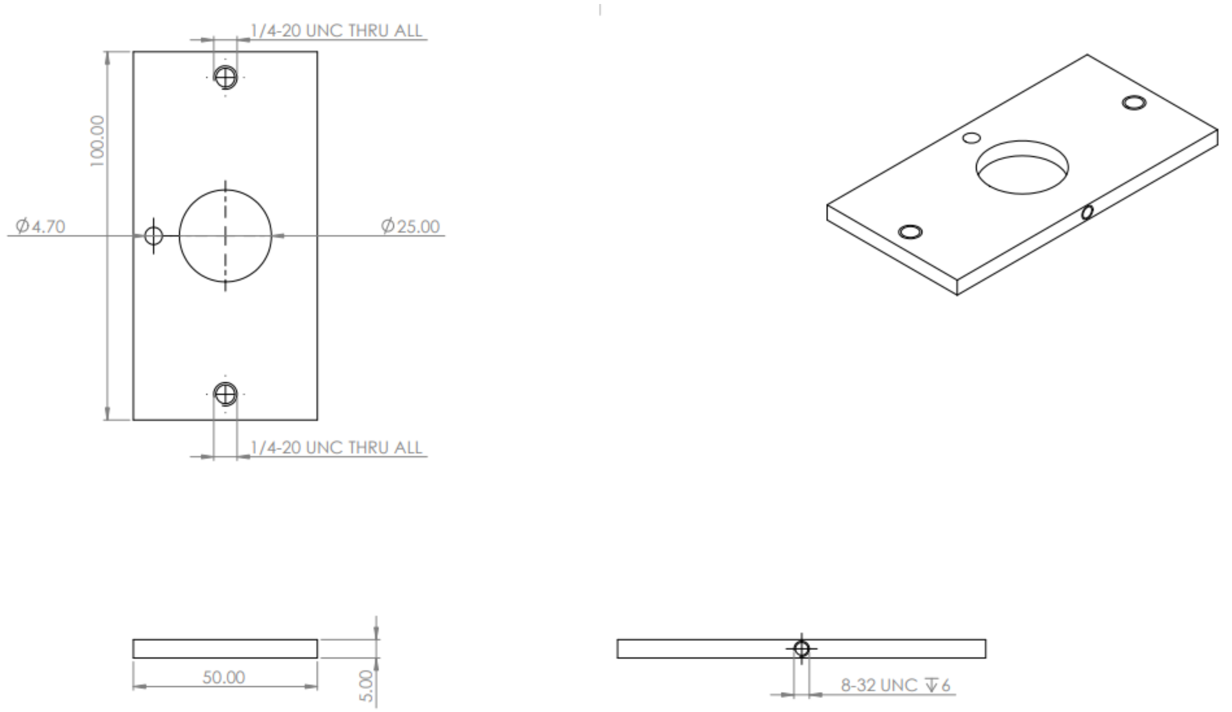

3D printed servo horn attachment:

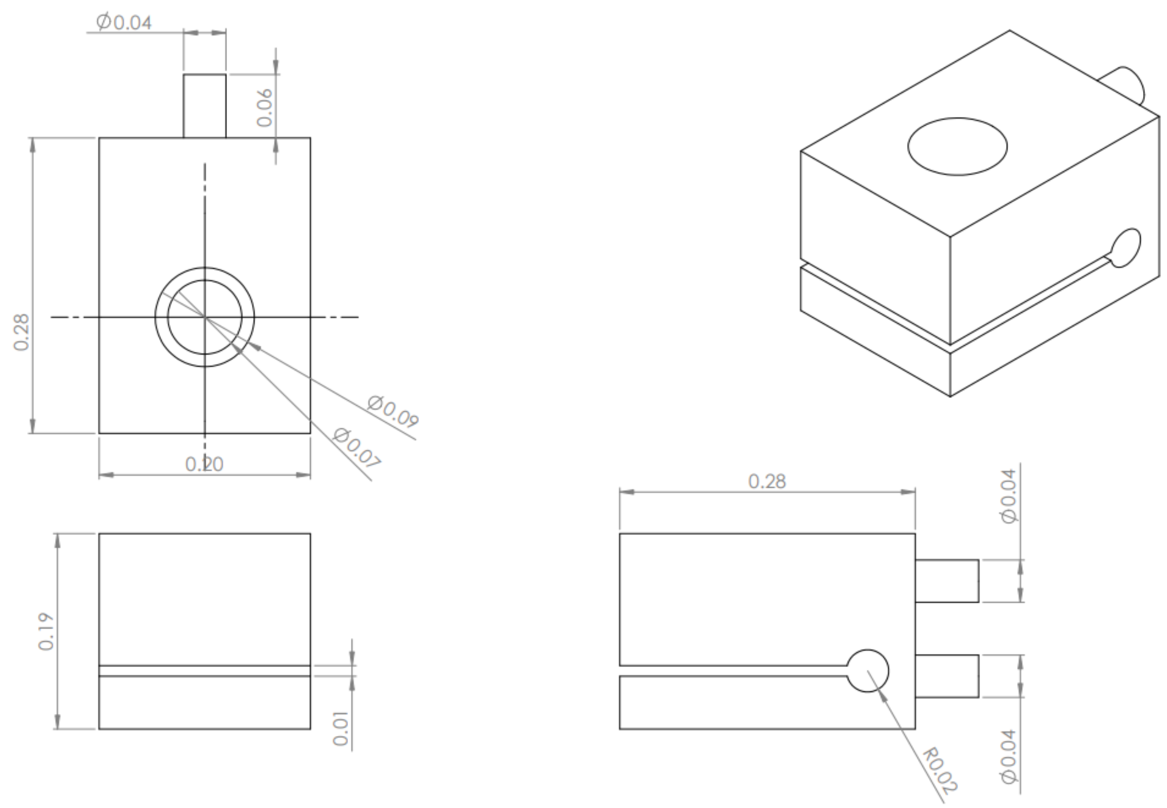

Pillar for stack fiber holder:

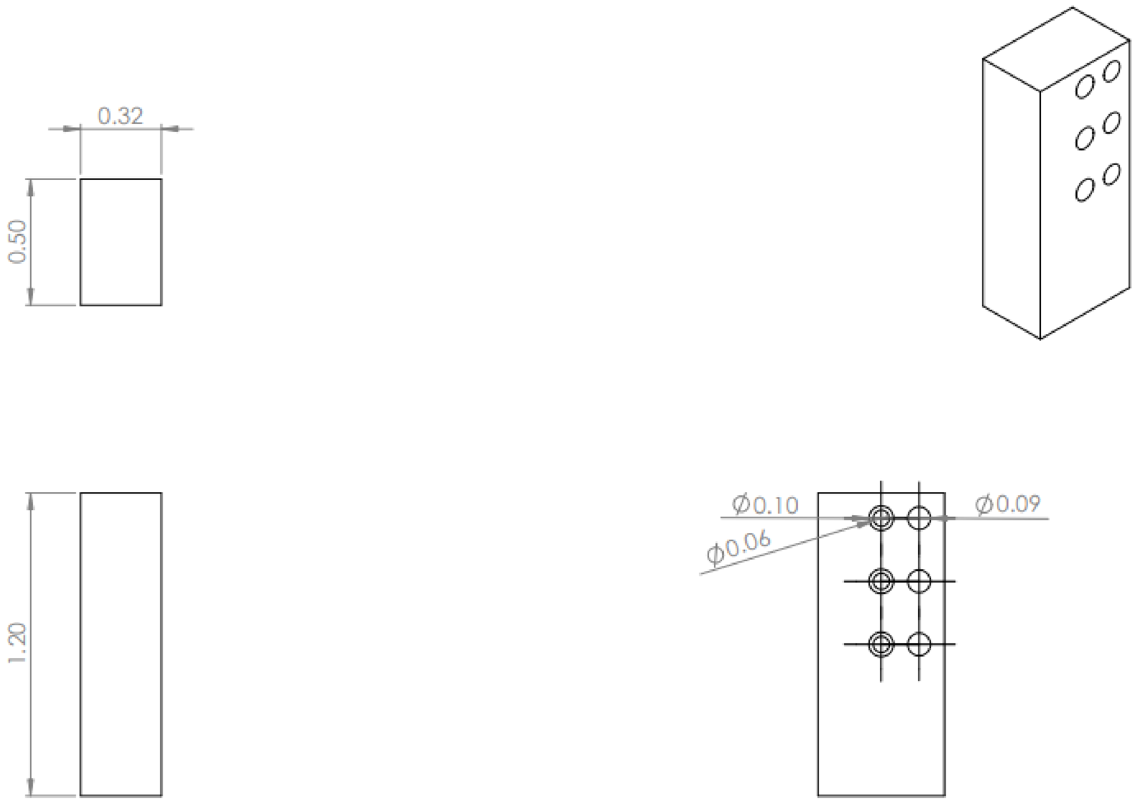

Fiber holder for pillar stacking:

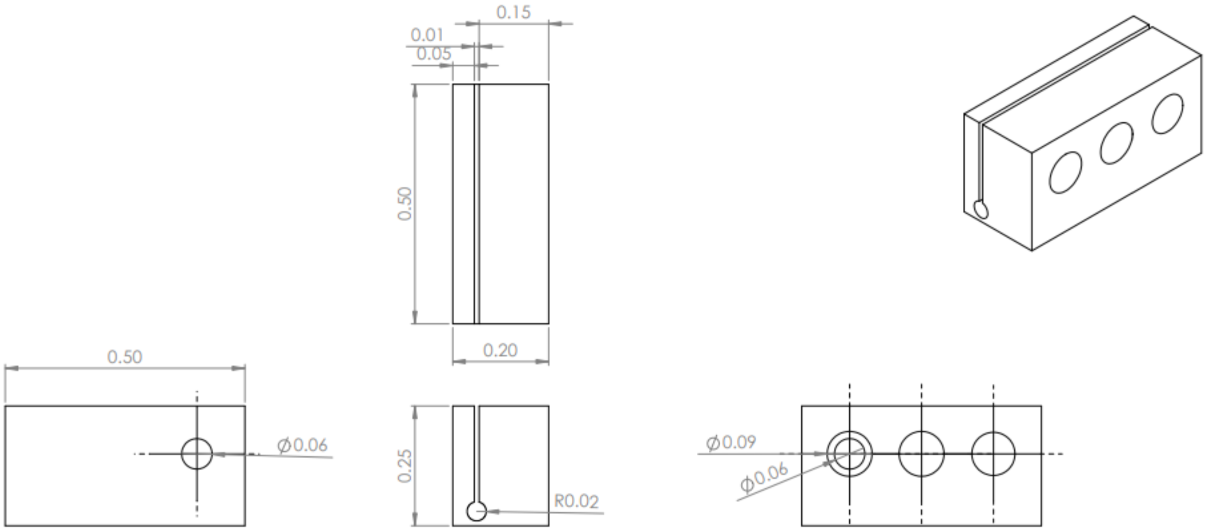

Orientation fiber holder compression lid:

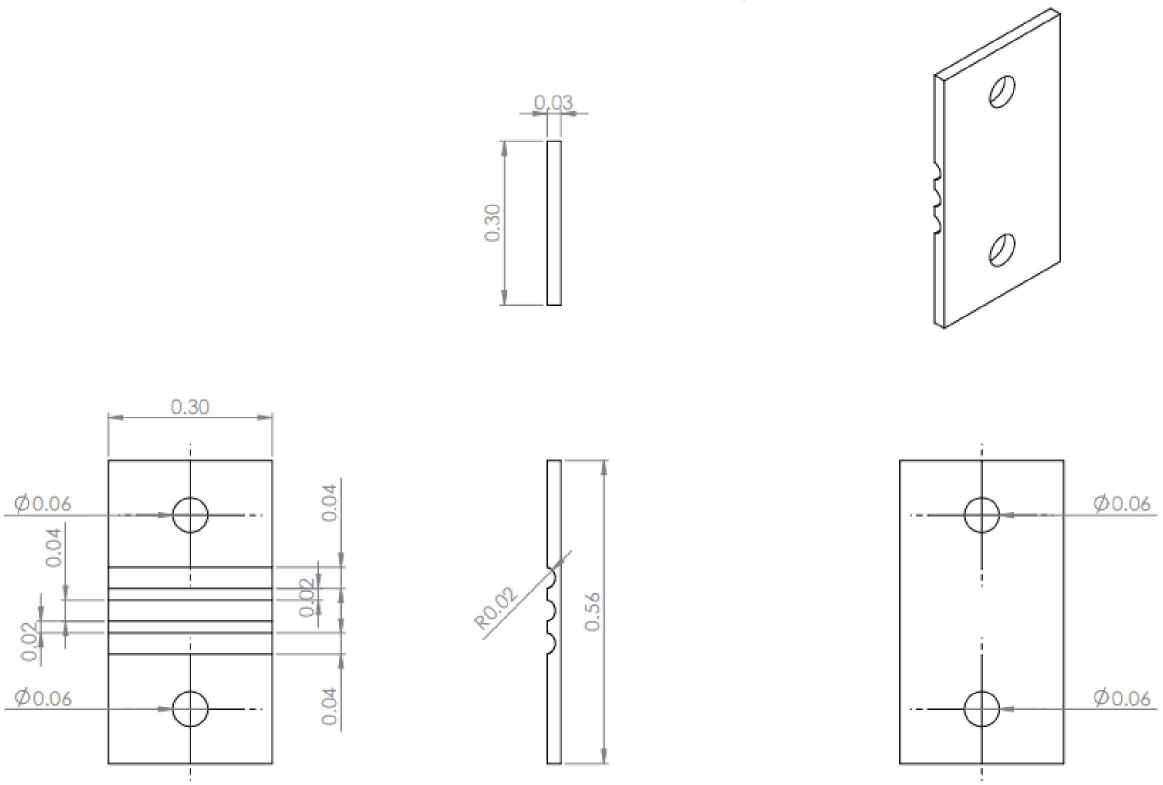

Orientation fiber holder:

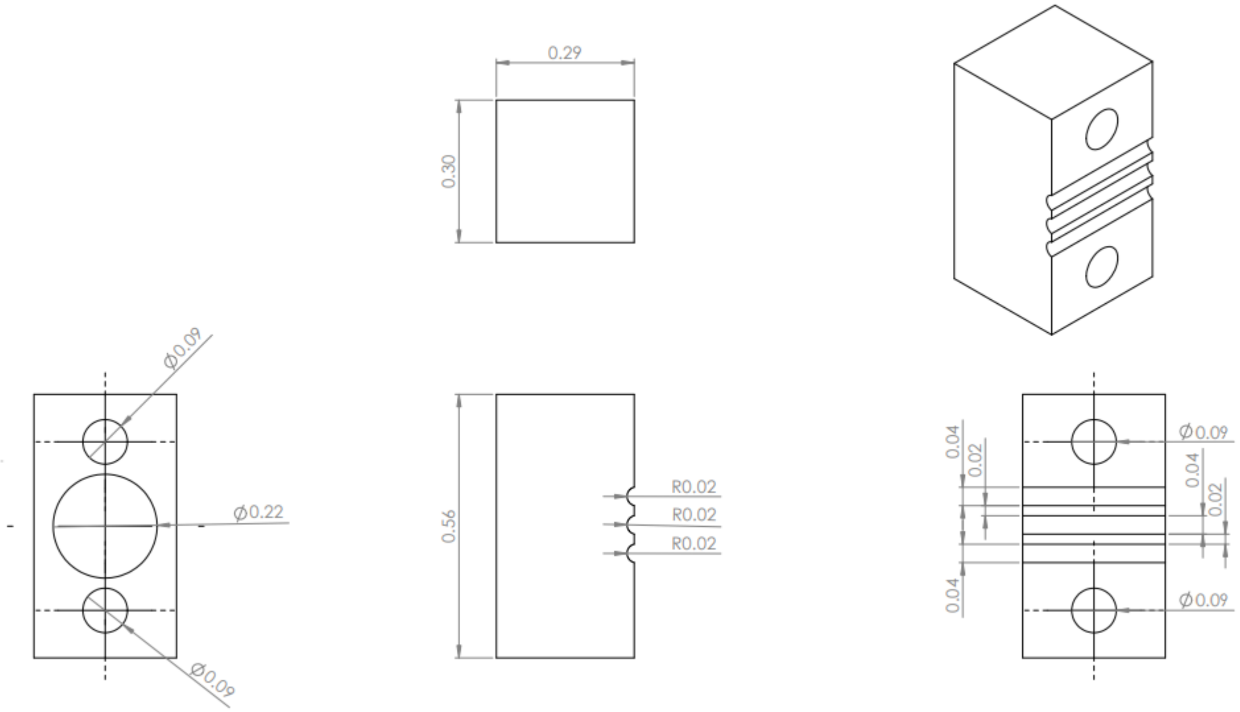

APPENDIX E: MICROCONTROLLER CODE

Servo Motion Code:

```
#include <Servo.h>

Servo myservo; // create servo object to control a servo


int pos = 0;  // variable to store the servo position

void setup() {
myservo.attach(9); // attaches the servo on pin 9 to the servo object
}

void loop() {
for (pos = 0; pos <= 70; pos += 1) { // goes from 0 degrees to 70 degrees
// in steps of 1 degree
myservo.write(pos); // tell servo to go to position in variable 'pos'
delay(3);  // waits 15ms for the servo to reach the position
}
for (pos = 70; pos >= 0; pos -= 1) { // goes from 70 degrees to 0 degrees
myservo.write(pos); // tell servo to go to position in variable 'pos'
delay(3);  // waits 15ms for the servo to reach the position
 }
}
```